Internal Node Microwave Monolithic Integrated Circuit Diagnostics Using Scanning Electrostatic Force Microscopy

BY

MANOJ MITTAL

45

A Thesis
Submitted to the Faculty of Graduate Studies
in Partial Fulfillment of the Requirements
for the Degree of

Master of Science

Department of Electrical and Computer Engineering
University of Manitoba
Winnipeg, Manitoba

December, 1994

ISBN 0-612-13377-X

Canada

Name _____

Dissertation Abstracts International is arranged by broad, general subject categories. Please select the one subject which most nearly describes the content of your dissertation. Enter the corresponding four-digit code in the spaces provided.

ELECTRONICS AND ELECTRICAL ENGINEERING | 0544 | U·M·I

SUBJECT TERM SUBJECT CODE

Subject Categories

THE HUMANITIES AND SOCIAL SCIENCES

COMMUNICATIONS AND THE ARTS
Architecture 0729
Art History 0377
Cinema 0900
Dance 0378
Fine Arts 0357
Information Science 0723
Journalism 0391
Library Science 0399
Mass Communications 0708
Music 0413
Speech Communication 0459
Theater 0465

EDUCATION
General 0515
Administration 0514
Adult and Continuing 0516
Agricultural 0517
Art 0273
Bilingual and Multicultural 0282
Business 0688
Community College 0275
Curriculum and Instruction 0727
Early Childhood 0518
Elementary 0524
Finance 0277
Guidance and Counseling 0519
Health 0680
Higher 0745
History of 0520
Home Economics 0278
Industrial 0521
Language and Literature 0279
Mathematics 0280
Music 0522
Philosophy of 0998
Physical 0523
Psychology 0525
Reading 0535
Religious 0527
Sciences 0714
Secondary 0533
Social Sciences 0534
Sociology of 0340
Special 0529
Teacher Training 0530
Technology 0710
Tests and Measurements 0288
Vocational 0747

LANGUAGE, LITERATURE AND LINGUISTICS
Language
- General 0679
- Ancient 0289
- Linguistics 0290
- Modern 0291

Literature
- General 0401
- Classical 0294
- Comparative 0295
- Medieval 0297
- Modern 0298
- African 0316
- American 0591
- Asian 0305
- Canadian (English) 0352
- Canadian (French) 0355
- English 0593
- Germanic 0311
- Latin American 0312
- Middle Eastern 0315
- Romance 0313
- Slavic and East European 0314

PHILOSOPHY, RELIGION AND THEOLOGY
Philosophy 0422
Religion
- General 0318
- Biblical Studies 0321
- Clergy 0319
- History of 0320
- Philosophy of 0322

Theology 0469

SOCIAL SCIENCES
American Studies 0323
Anthropology
- Archaeology 0324
- Cultural 0326
- Physical 0327

Business Administration
- General 0310
- Accounting 0272
- Banking 0770
- Management 0454
- Marketing 0338

Canadian Studies 0385
Economics
- General 0501
- Agricultural 0503
- Commerce-Business 0505
- Finance 0508
- History 0509
- Labor 0510
- Theory 0511

Folklore 0358
Geography 0366
Gerontology 0351
History
- General 0578
- Ancient 0579
- Medieval 0581
- Modern 0582
- Black 0328
- African 0331
- Asia, Australia and Oceania 0332
- Canadian 0334
- European 0335
- Latin American 0336
- Middle Eastern 0333
- United States 0337

History of Science 0585
Law 0398
Political Science
- General 0615
- International Law and Relations 0616
- Public Administration 0617

Recreation 0814
Social Work 0452
Sociology
- General 0626
- Criminology and Penology ... 0627
- Demography 0938
- Ethnic and Racial Studies 0631
- Individual and Family Studies 0628
- Industrial and Labor Relations 0629
- Public and Social Welfare 0630
- Social Structure and Development 0700
- Theory and Methods 0344

Transportation 0709
Urban and Regional Planning 0999
Women's Studies 0453

THE SCIENCES AND ENGINEERING

BIOLOGICAL SCIENCES
Agriculture
- General 0473
- Agronomy 0285
- Animal Culture and Nutrition 0475
- Animal Pathology 0476
- Food Science and Technology 0359
- Forestry and Wildlife 0478
- Plant Culture 0479
- Plant Pathology 0480
- Plant Physiology 0817
- Range Management 0777
- Wood Technology 0746

Biology
- General 0306
- Anatomy 0287
- Biostatistics 0308
- Botany 0309
- Cell 0379
- Ecology 0329
- Entomology 0353
- Genetics 0369
- Limnology 0793
- Microbiology 0410
- Molecular 0307
- Neuroscience 0317
- Oceanography 0416
- Physiology 0433
- Radiation 0821
- Veterinary Science 0778
- Zoology 0472

Biophysics
- General 0786
- Medical 0760

EARTH SCIENCES
Biogeochemistry 0425
Geochemistry 0996
Geodesy 0370
Geology 0372
Geophysics 0373
Hydrology 0388
Mineralogy 0411
Paleobotany 0345
Paleoecology 0426
Paleontology 0418
Paleozoology 0985
Palynology 0427
Physical Geography 0368
Physical Oceanography 0415

HEALTH AND ENVIRONMENTAL SCIENCES
Environmental Sciences 0768
Health Sciences
- General 0566
- Audiology 0300
- Chemotherapy 0992
- Dentistry 0567
- Education 0350
- Hospital Management 0769
- Human Development 0758
- Immunology 0982
- Medicine and Surgery 0564
- Mental Health 0347
- Nursing 0569
- Nutrition 0570
- Obstetrics and Gynecology .. 0380
- Occupational Health and Therapy 0354
- Ophthalmology 0381
- Pathology 0571
- Pharmacology 0419
- Pharmacy 0572
- Physical Therapy 0382
- Public Health 0573
- Radiology 0574
- Recreation 0575
- Speech Pathology 0460
- Toxicology 0383

Home Economics 0386

PHYSICAL SCIENCES
Pure Sciences
Chemistry
- General 0485
- Agricultural 0749
- Analytical 0486
- Biochemistry 0487
- Inorganic 0488
- Nuclear 0738
- Organic 0490
- Pharmaceutical 0491
- Physical 0494
- Polymer 0495
- Radiation 0754

Mathematics 0405
Physics
- General 0605
- Acoustics 0986
- Astronomy and Astrophysics 0606
- Atmospheric Science 0608
- Atomic 0748
- Electronics and Electricity 0607
- Elementary Particles and High Energy 0798
- Fluid and Plasma 0759
- Molecular 0609
- Nuclear 0610
- Optics 0752
- Radiation 0756
- Solid State 0611

Statistics 0463

Applied Sciences
Applied Mechanics 0346
Computer Science 0984
Engineering
- General 0537
- Aerospace 0538
- Agricultural 0539
- Automotive 0540
- Biomedical 0541
- Chemical 0542
- Civil 0543
- Electronics and Electrical 0544
- Heat and Thermodynamics ... 0348
- Hydraulic 0545
- Industrial 0546
- Marine 0547
- Materials Science 0794
- Mechanical 0548
- Metallurgy 0743
- Mining 0551
- Nuclear 0552
- Packaging 0549
- Petroleum 0765
- Sanitary and Municipal 0554
- System Science 0790

Geotechnology 0428
Operations Research 0796
Plastics Technology 0795
Textile Technology 0994

PSYCHOLOGY
General 0621
Behavioral 0384
Clinical 0622
Developmental 0620
Experimental 0623
Industrial 0624
Personality 0625
Physiological 0989
Psychobiology 0349
Psychometrics 0632
Social 0451

Nom _____

Dissertation Abstracts International est organisé en catégories de sujets. Veuillez s.v.p. choisir le sujet qui décrit le mieux votre thèse et inscrivez le code numérique approprié dans l'espace réservé ci-dessous.

_____ ☐☐☐ U·M·I

SUJET — CODE DE SUJET

Catégories par sujets

HUMANITÉS ET SCIENCES SOCIALES

COMMUNICATIONS ET LES ARTS
Architecture 0729
Beaux-arts 0357
Bibliothéconomie 0399
Cinéma 0900
Communication verbale 0459
Communications 0708
Danse 0378
Histoire de l'art 0377
Journalisme 0391
Musique 0413
Sciences de l'information 0723
Théâtre 0465

ÉDUCATION
Généralités 515
Administration 0514
Art 0273
Collèges communautaires 0275
Commerce 0688
Économie domestique 0278
Éducation permanente 0516
Éducation préscolaire 0518
Éducation sanitaire 0680
Enseignement agricole 0517
Enseignement bilingue et multiculturel 0282
Enseignement industriel 0521
Enseignement primaire. 0524
Enseignement professionnel 0747
Enseignement religieux 0527
Enseignement secondaire 0533
Enseignement spécial 0529
Enseignement supérieur 0745
Évaluation 0288
Finances 0277
Formation des enseignants 0530
Histoire de l'éducation 0520
Langues et littérature 0279
Lecture 0535
Mathématiques 0280
Musique 0522
Orientation et consultation 0519
Philosophie de l'éducation 0998
Physique 0523
Programmes d'études et enseignement 0727
Psychologie 0525
Sciences 0714
Sciences sociales 0534
Sociologie de l'éducation 0340
Technologie 0710

LANGUE, LITTÉRATURE ET LINGUISTIQUE
Langues
- Généralités 0679
- Anciennes 0289
- Linguistique 0290
- Modernes 0291

Littérature
- Généralités 0401
- Anciennes 0294
- Comparée 0295
- Médiévale 0297
- Moderne 0298
- Africaine 0316
- Américaine 0591
- Anglaise 0593
- Asiatique 0305
- Canadienne (Anglaise) 0352
- Canadienne (Française) 0355
- Germanique 0311
- Latino-américaine 0312
- Moyen-orientale 0315
- Romane 0313
- Slave et est-européenne 0314

PHILOSOPHIE, RELIGION ET THÉOLOGIE
Philosophie 0422
Religion
- Généralités 0318
- Clergé 0319
- Études bibliques 0321
- Histoire des religions 0320
- Philosophie de la religion 0322

Théologie 0469

SCIENCES SOCIALES
Anthropologie
- Archéologie 0324
- Culturelle 0326
- Physique 0327

Droit 0398
Économie
- Généralités 0501
- Commerce-Affaires 0505
- Économie agricole 0503
- Économie du travail 0510
- Finances 0508
- Histoire 0509
- Théorie 0511

Études américaines 0323
Études canadiennes 0385
Études féministes 0453
Folklore 0358
Géographie 0366
Gérontologie 0351
Gestion des affaires
- Généralités 0310
- Administration 0454
- Banques 0770
- Comptabilité 0272
- Marketing 0338

Histoire
- Histoire générale 0578
- Ancienne 0579
- Médiévale 0581
- Moderne 0582
- Histoire des noirs 0328
- Africaine 0331
- Canadienne 0334
- États-Unis 0337
- Européenne 0335
- Moyen-orientale 0333
- Latino-américaine 0336
- Asie, Australie et Océanie 0332

Histoire des sciences 0585
Loisirs 0814
Planification urbaine et régionale 0999
Science politique
- Généralités 0615
- Administration publique 0617
- Droit et relations internationales 0616

Sociologie
- Généralités 0626
- Aide et bien-être social 0630
- Criminologie et établissements pénitentiaires 0627
- Démographie 0938
- Études de l' individu et de la famille 0628
- Études des relations interethniques et des relations raciales 0631
- Structure et développement social 0700
- Théorie et méthodes. 0344
- Travail et relations industrielles 0629

Transports 0709
Travail social 0452

SCIENCES ET INGÉNIERIE

SCIENCES BIOLOGIQUES
Agriculture
- Généralités 0473
- Agronomie. 0285
- Alimentation et technologie alimentaire 0359
- Culture 0479
- Élevage et alimentation 0475
- Exploitation des pâturages 0777
- Pathologie animale 0476
- Pathologie végétale 0480
- Physiologie végétale 0817
- Sylviculture et faune 0478
- Technologie du bois 0746

Biologie
- Généralités 0306
- Anatomie 0287
- Biologie (Statistiques) 0308
- Biologie moléculaire 0307
- Botanique 0309
- Cellule 0379
- Écologie 0329
- Entomologie 0353
- Génétique 0369
- Limnologie 0793
- Microbiologie 0410
- Neurologie 0317
- Océanographie 0416
- Physiologie 0433
- Radiation 0821
- Science vétérinaire 0778
- Zoologie 0472

Biophysique
- Généralités 0786
- Medicale 0760

SCIENCES DE LA TERRE
Biogéochimie 0425
Géochimie 0996
Géodésie 0370
Géographie physique 0368
Géologie 0372
Géophysique 0373
Hydrologie 0388
Minéralogie 0411
Océanographie physique 0415
Paléobotanique 0345
Paléoécologie 0426
Paléontologie 0418
Paléozoologie 0985
Palynologie 0427

SCIENCES DE LA SANTÉ ET DE L'ENVIRONNEMENT
Économie domestique 0386
Sciences de l'environnement 0768
Sciences de la santé
- Généralités 0566
- Administration des hôpitaux 0769
- Alimentation et nutrition 0570
- Audiologie 0300
- Chimiothérapie 0992
- Dentisterie 0567
- Développement humain 0758
- Enseignement 0350
- Immunologie 0982
- Loisirs 0575
- Médecine du travail et thérapie 0354
- Médecine et chirurgie 0564
- Obstétrique et gynécologie 0380
- Ophtalmologie 0381
- Orthophonie 0460
- Pathologie 0571
- Pharmacie 0572
- Pharmacologie 0419
- Physiothérapie 0382
- Radiologie 0574
- Santé mentale 0347
- Santé publique 0573
- Soins infirmiers 0569
- Toxicologie 0383

SCIENCES PHYSIQUES
Sciences Pures
Chimie
- Généralités 0485
- Biochimie 487
- Chimie agricole 0749
- Chimie analytique 0486
- Chimie minérale 0488
- Chimie nucléaire 0738
- Chimie organique 0490
- Chimie pharmaceutique 0491
- Physique 0494
- PolymÈres 0495
- Radiation 0754

Mathématiques 0405
Physique
- Généralités 0605
- Acoustique 0986
- Astronomie et astrophysique 0606
- Électronique et électricité 0607
- Fluides et plasma 0759
- Météorologie 0608
- Optique 0752
- Particules (Physique nucléaire) 0798
- Physique atomique 0748
- Physique de l'état solide 0611
- Physique moléculaire 0609
- Physique nucléaire 0610
- Radiation 0756

Statistiques 0463

Sciences Appliqués Et Technologie
Informatique 0984
Ingénierie
- Généralités 0537
- Agricole 0539
- Automobile 0540
- Biomédicale 0541
- Chaleur et thermodynamique 0348
- Conditionnement (Emballage) 0549
- Génie aérospatial 0538
- Génie chimique 0542
- Génie civil 0543
- Génie électronique et électrique 0544
- Génie industriel 0546
- Génie mécanique 0548
- Génie nucléaire 0552
- Ingénierie des systèmes 0790
- Mécanique navale 0547
- Métallurgie 0743
- Science des matériaux 0794
- Technique du pétrole 0765
- Technique minière 0551
- Techniques sanitaires et municipales 0554
- Technologie hydraulique 0545

Mécanique appliquée 0346
Géotechnologie 0428
Matières plastiques (Technologie) 0795
Recherche opérationnelle 0796
Textiles et tissus (Technologie) 0794

PSYCHOLOGIE
Généralités 0621
Personnalité 0625
Psychobiologie 0349
Psychologie clinique 0622
Psychologie du comportement 0384
Psychologie du développement 0620
Psychologie expérimentale 0623
Psychologie industrielle 0624
Psychologie physiologique 0989
Psychologie sociale 0451
Psychométrie 0632

INTERNAL NODE MICROWAVE MONOLITHIC INTEGRATED CIRCUIT DIAGNOSTICS USING SCANNING ELECTROSTATIC FORCE MICROSCOPY

BY

MANOJ MITTAL

A Thesis submitted to the Faculty of Graduate Studies of the University of Manitoba in partial fulfillment of the requirements of the degree of

MASTER OF SCIENCE

Abstract

The ongoing development of high–speed integrated circuits, based on silicon as well as GaAs technologies has led to an increased demand for internal voltage measurement techniques with picosecond time resolution. High frequency circuits are being developed for a wide range of applications, from digital memories to microwave amplifiers. At the same time, the shrinking geometrical dimensions and smaller voltage swings of modern high frequency devices require a voltage resolution in the mV range and probing resolutions well below 1 μm. The currently available measurement techniques do not meet the combined requirement of high temporal and spatial resolution, high voltage sensitivity, internal node access, non–invasiveness and simplicity.

The electrostatic force microscope is one in a family of scanned probe microscopes that is capable of providing accurate non–invasive measurements of potentials at the internal nodes of a circuit. The application of this microscope for measurements of sinusoidal signals at radio frequencies (RF) is investigated in this thesis. A measurement instrument using commonly available microwave components has been designed and constructed. Measurements on a microstrip thru–line and a MMIC low noise amplifier have been performed. Measured circuit characteristics match well with those measured using a network analyzer. Measurements at the internal nodes of an LNA demonstrate the usefulness of the instrument in characterizing individual components in a fully functioning microwave integrated circuit chip.

With some improvements to automate the measurement procedure, this instrument can serve as an important diagnostic tool in the hands of circuit designers as well for test and manufacture on a commercial scale.

Acknowledgements

I would like to express my sincere gratitude to Dr. G. Bridges for his guidance and support. He has been a constant source of motivation for me. I look forward to working with him on future projects.

Special thanks to Dave Roscoe of Communications Research Centre, Ottawa for letting us play with the TI low noise amplifier.

Thanks also to R.A. Said for helping me understand the nuances of the instrument and to Dean McNeill for his help with the scanner.

The support of technical staff in the department – Brad Tabachnick, Al Symmons and Al McKay, in particular, is gratefully acknowledged.

Finally I would like to thank members of my family. Without their support, this work could not have been completed. Special thanks to Abha, my dear wife, for her patience and understanding.

Financial support from the Province of Manitoba, Federal Government's Networks of Centres of Excellence Program/Micronet and the Natural Sciences and Engineering Research Council of Canada (NSERC) is gratefully acknowledged.

TABLE OF CONTENTS

List of Figures

Figure **Page**

List of Tables

Table **Page**

CHAPTER 1

Introduction

In recent years, the growing complexity of integrated circuits and their ever–faster working speeds have led to the need for contactless measurement methods for logic–state analysis and waveform measurements on internal nodes of very–large–scale–integration (VLSI) circuits. An important requirement to be fulfilled in this environment is the capability of measuring ultrafast signals with rise and fall times below 10 ps on metal lines of 0.5–1.0μm width and spacing and with a voltage resolution better than 5 mV. In addition, it is desirable that the diagnostic technique be applicable to all technologies, rather than being limited to Si or GaAs based circuitry only.

It has been argued that when internal waveform measurements become a standard procedure in IC development, both development time and IC quality will benefit [1]. Currently available measurement techniques are limited in their ability to meet the combined requirements of high temporal and spatial resolution, internal node access, absolute voltage measurement, high sensitivity, non–invasiveness and simplicity.

The main objective of this thesis is to investigate the application of the electrostatic force microscope for measurement of sinusoidal signals at radio frequencies (RF) at the internal nodes of monolithic (MMIC) microwave integrated circuits. For this purpose, a measurement instrument using commonly available microwave components has been designed and constructed. Measurements on a microstrip thru–line and a MMIC low noise amplifier have been performed.

The thesis is organized as follows. Chapter 2 contains a brief review of some of the measurement techniques that are currently employed for waveform measurements. Both direct contact and non–contact techniques are summarized. Relative advantages and disadvantages of each technique are discussed.

Chapter 3 introduces the force microscope. A number of novel scanned probe microscopes that have been developed in the last decade are described briefly. Electrostatic force microscope, the instrument used in present research is modelled next. Components of the instrument – the cantilever probe and the displacement sensor are then described. Spatial resolution and sensitivity, the two important parameters which characterize the force microscope, are discussed. DC and the AC signal measurement schemes are described.

Measurements were first performed at 10 MHz. The measurement system and the results of these measurements are provided in Chapter 4.

Chapter 5 first discusses some of the high frequency issues that are important when the frequencies approach the GHz range. Probe matching is important and is discussed next. The details of the measurement instrument are then given. Measurements at 1 GHz were performed on a microstrip thru–line and on a Texas Instruments (TI) low noise amplifier. Results of these measurements are presented.

Chapter 6 briefly describes the extensions of the heterodyne measurement technique for the spectral analysis of waveforms. Sampled waveform measurements can also be performed using this technique and is discussed briefly. Finally, some conclusions are given and recommendations for possible future work that are suggested by this research are made.

CHAPTER 2

Review of Waveform Measurement Techniques

A review of various measurement techniques for high frequency IC and MMIC diagnostics currently being researched is presented. The operating principle, advantages and disadvantages of each technique are discussed and some sample measurements are provided.

2.1 Electron Beam Testing

Electron Beam Testing refers to the measurement of waveforms with the aid of an electron beam probe. The technique has been under development for last several decades and originates from standard SEM. The operating principle of electron beam testing is outlined in Fig. 2.1. A pulsed electron beam is focussed on the point of interest within the device under test (DUT). Bombardment by primary electrons causes the probed area to emit secondary electrons (SE). A retarding grid spectrometer in front of the detector allows the secondary electrons to be analyzed with respect to their energy. This enables determination of relative potentials of the probed IC internal node. Synchronization between the electron pulses, as generated by the blanking control signal, and the repeated signal stimulating the DUT ensures that a constant voltage is sampled with a fixed phase relation. Slowly shifting the phase relation between the probe pulse and the DUT stimulus allows an entire waveform to be recorded.

A feedback loop is usually used to keep the detector signal constant by readjusting the retarding grid voltage of the spectrometer during the phase scan. The retarding grid voltage thus tracks the voltage of the sampled waveform and is recorded with respect to the phase shift between signal and e–beam pulses [2].

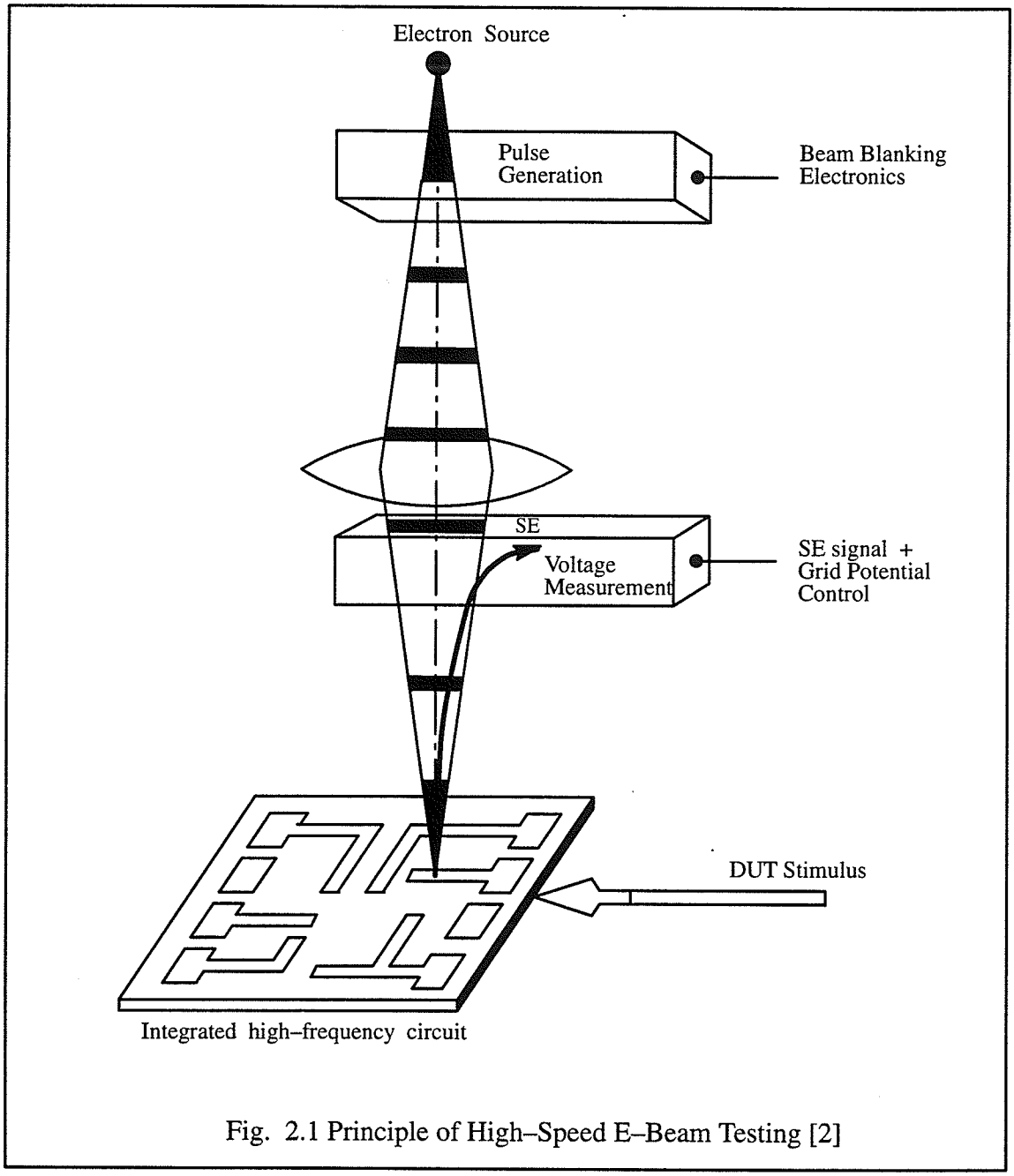

Fig. 2.1 Principle of High–Speed E–Beam Testing [2]

Voltage contrast results from the local potentials at the surface of the IC when it is operating. For example, when the interconnection is in a 'high' logic state (positive voltage), it attracts back a large portion of the resulting secondary electrons. The second-

ary electron collector then 'sees' fewer electrons, so that these points appear dark in the image. On the other hand, a large percentage of secondary electrons will reach the collector when the interconnection is in a 'low' logic state. These points then appear bright [3].

E–Beam testing is a widely accepted tool for direct voltage measurements on the interconnection of integrated circuits. Its main application has been the testing of complex VLSI and ULSI circuits, with emphasis on connection to CAD workstations and on automation to allow for high throughput measurements of a great number of signals within a single circuit. This technique has been an integral part of design verification flow that new products undergo at Intel [4]. With a 7–ps effective sampling pulse width, this technique has demonstrated evaluation of high–frequency devices with a 0.5 μm probe diameter and 2–mV/$(Hz)^{1/2}$ noise voltage at a 1 GHz repetition frequency [2].

A specific number of secondary electrons are required for signal processing. If the pulse width is greatly reduced (< 1 ns) to achieve high temporal resolution, then only a few or even single electrons are generated per pulse. This results in low signal levels and repetitive sampling over long durations is necessary to achieve an acceptable signal to noise ratio.

Another drawback of this technique is that at the beam energies suitable for probing integrated circuits, there is a considerable spot size degradation and submicron spatial resolution is difficult to achieve simultaneously with high temporal resolution. As well, to avoid irradiation damage of circuit elements and current loading of internal nodes, low acceleration voltages of primary electron beam is required. This leads to a reduction in the rise and fall time of the pulse edges.

The accuracy of the e–beam testing technique is also reduced by the transit–time effect. The transit–time effect is caused by the change in the potential field above the device surface associated with the alternating signal at the test point. After emission, the secondary electrons accelerate towards the spectrometer with a potential energy. This energy is converted into kinetic energy before the retarding field spectrometer. The total energy remains constant if a constant field is maintained. The energy of the secondary electrons reveals the test–point voltage without any error in this case. This description is no longer valid if the potential changes while the electron is still close to the point of emission, which is the typical situation at very high frequencies. In this case, the secondary electron energy reveals the average of the potential during the time the electron spends in the electrical field of the test point. This time is deter-

mined by the speed of the secondary electron and the spatial extent of the electrical field, the latter depending on the test point dimensions. Different geometries of the probe points lead to different transit times which may cause errors in propagation delay measurements.

As the voltage is derived by analyzing the energy of secondary electrons, e–beam probing is not a direct measurement technique. Calibration is required which becomes more complex in the presence of a passivation layer on the device. Besides the above listed limitations, the measurement system is fairly complex and expensive and since it must operate in vacuum, it requires specialized test circuit setup.

2.2 Photoemission Probing

The photoemission probing technique extends the temporal capabilities of electron beam probing. In photoemission probing, a continuous (real–time mode) or pulsed (stroboscopic sampling mode) laser beam is focused onto a metal line to induce photoemission of electrons from the metal. The voltage level at the point from which electron emission occurs is determined by accelerating the electrons toward a reference or retarding field electrode. The photoemitted electrons that pass the reference electrode are guided towards an electron detector. The detected electron current is a function of the potential difference between the point of the sample being tested and the reference or retarding electrode. The voltage change is extracted by calibrating the change in the intensity of measured electrons against the change in voltage, or it is extracted directly by using a feedback loop to keep the measured intensity constant by shifting the retarding voltage. Typical setup of the probing instrument is shown in Fig. 2.2.

In the real–time mode, the voltage change is detected directly, with the possible time resolution of the measurement determined by the reaction time of the electron detector, which counts the number of electrons passing the retarding field barrier and the possible time–spread of the electrons during transport toward the detector due to various start energies [5].

The sampling mode is applied to detect voltage changes on the picosecond time scale for very fast signals. Here, picosecond laser pulses are used to induce photoemission similar to the e–beam technique. The temporal resolution is achieved by measuring the photoemission signal as a function of the delay between the signal on the device and the laser pulse which excites the electrons into vacuum. This method works only

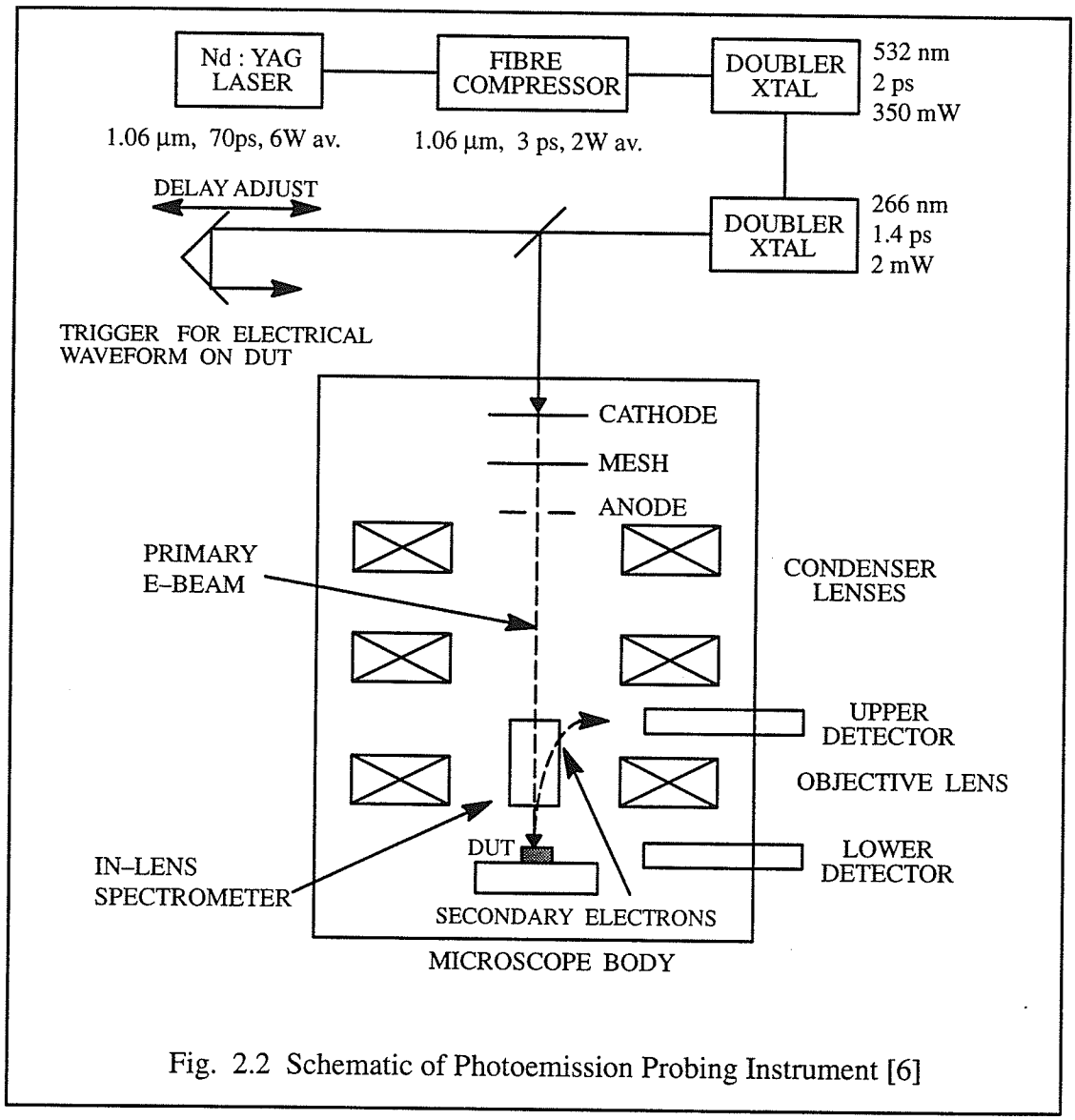

Fig. 2.2 Schematic of Photoemission Probing Instrument [6]

for periodic signals and requires a synchronization of the signal at the device with the probing laser pulse. For each delay selected, the voltage level is measured just as if there were a constant signal voltage at the device. The entire signal waveform is then determined by combining all the snapshot pictures for different delay times. The time resolution of the sampling mode is determined by the time the induced pulse of emitted electrons interacts with the electric potential of the sample, hence the duration of the laser pulse.

The total yield of emitted electrons and the width of the energy distribution are both important parameters which determine the voltage sensitivity of photoemission probing. Theoretically, the best voltage sensitivity should be achieved with the largest

possible number of emitted electrons per pulse without causing damage from the correspondingly large incident primary beam. However a high electron density in a pulse leads to a broadening of the energy distribution of the emitted electrons and therefore degradation in temporal resolution.

The photoemission probing technique has demonstrated stroboscopic noncontact waveform measurements on metal interconnect lines with a temporal resolution better than 5 ps, a voltage resolution of 3 mV/ $(Hz)^{1/2}$ and a spatial resolution of 0.1 μm [6]. This technique has been used for measurements on internal nodes of a sub–100 ps emitter coupled logic (ECL) bipolar ring oscillator [6].

Photoemission probing is a very surface–sensitive method and this sensitivity can cause severe problems with respect to the stability and reliability of the measurements. The surface sensitivity of the method must be taken into account for air–exposed samples if the measurement time on a single spot of the sample exceeds a few seconds [5].

2.3 Photoconductive Sampling

Photoconductive sampling or optoelectronic techniques use photoconductive switches for both signal generation and sampling. A photoconductive switch is usually fabricated from a doped semiconductor material. It acts as a high impedance under ambient conditions and as a good short circuit when illuminated by high intensity light. Photoconductive switches are capable of generating ultra–short duration short–circuits when illuminated by fast laser pulses and are thus capable of probing short pulse signals along a transmission line. Sufficiently fast switching photoconductive switches, along with a picosecond laser source, creates pulses with high mm–wave frequency content, thus enabling extremely broadband characterization of MMICs. By launching the pulses along a terminated quasi–TEM transmission line, an inherently excellent broadband source match is provided to the MMIC. The laser excitation of a photoconductive switch can also perform signal sampling with a response function limited only by the photoconductive switch dynamics.

A schematic diagram of the optical measurement system for pulse generation and sampling is shown in Fig. 2.3. The incident pulse train is generated at a photoconductive switch at port 'a' and subsequently sampled at photoconductive switches at ports 'b' or 'c'. The transmitted waveform is sampled at port 'c'. The input and reflected waveforms are sampled at port 'b'. The reflected waveform is time–windowed by selecting the length of sampling time to isolate it from the incident waveform [7].

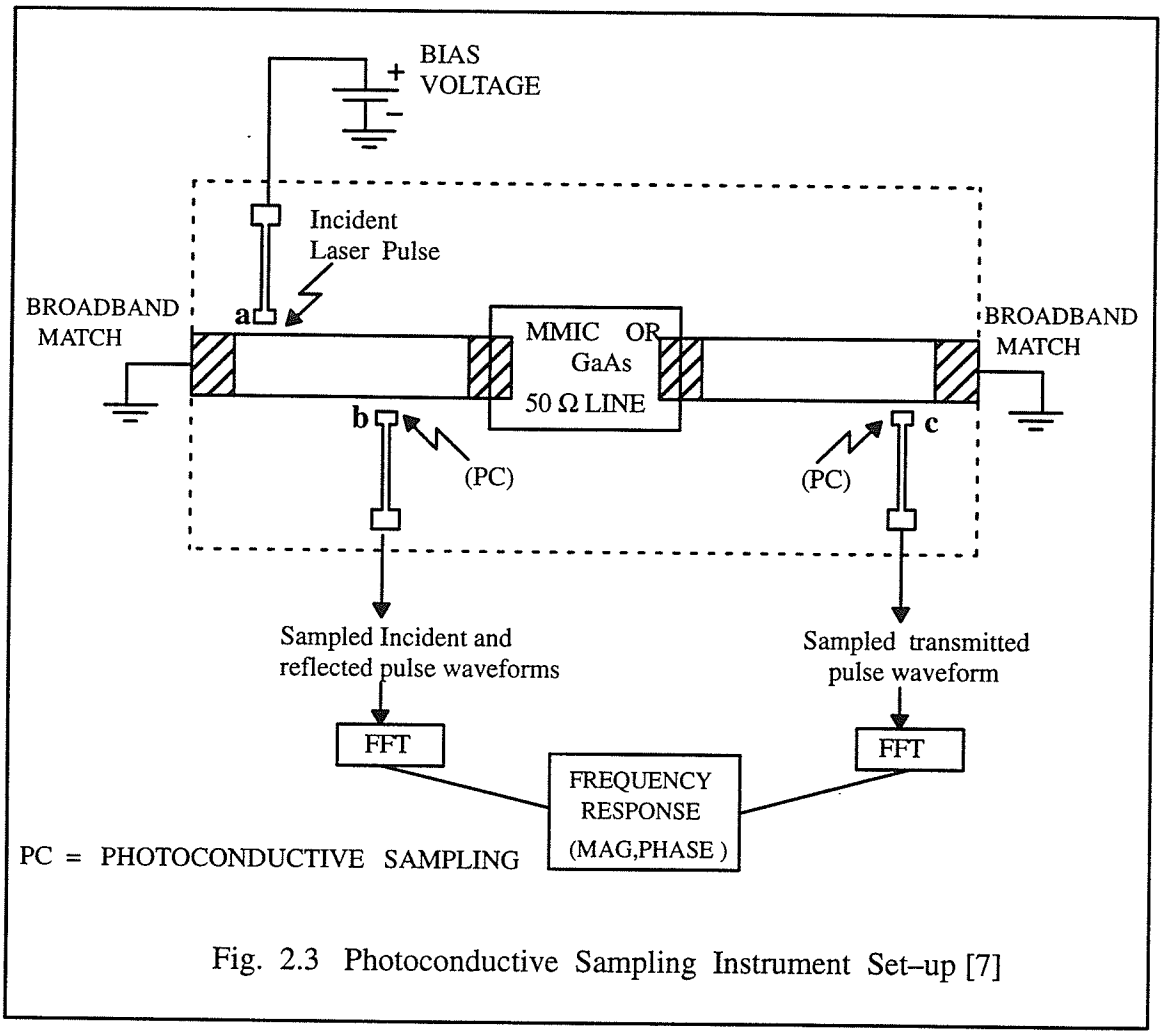

Fig. 2.3 Photoconductive Sampling Instrument Set–up [7]

The sampled signal is dependent on the characteristics of the incident electrical pulse and the photoconductive response of the sampling gap. To obtain de–embedded parameters, the loss and phase shift of the switch circuit, as determined by measuring the incident pulse, can be removed from the measured data.

The photoconductive switches are usually fabricated using MMIC compatible technology on semi–insulating GaAs substrate. The gaps are proton–implanted with hydrogen ions on the surface of the substrate to reduce the carrier lifetime, which results in faster switching time. Photoconductive switches have demonstrated response time on the order of 10 ps, limiting the incident waveform upper frequency range to 100 GHz [7]. Recently, a compact optoelectronic test structure that has the potential to be integrated with active devices on wafer has been fabricated and characterized over a 500–GHz bandwidth [8].

The main disadvantage of this technique is that the photoconductive switches must be formed as an integral part of the circuit under test.

In a recent development, a photoconductive sampling probe has demonstrated a 2.3 ps temporal resolution and 8–μm spatial resolution with a 4 μV/ $(Hz)^{1/2}$ sensitivity [9]. The probe is extremely small and offers the advantage of probing the circuit externally by locating it on the test point. It uses a metal–semiconductor–metal (MSM) interdigitated electrode structure as its photoconductive switch. The probe itself was fabricated from low–temperature grown GaAs of molecular beam epitaxy.

2.4 Plasma–Optical Probing

In plasma–optical probing technique, a high power laser beam is used to create plasma in the region between an electrode which serves as the probe and the DUT [10]. The plasma so generated serves as an electrical pathway through which signals appearing on the DUT can be probed. A configuration of the probing system is shown in Fig. 2.4.

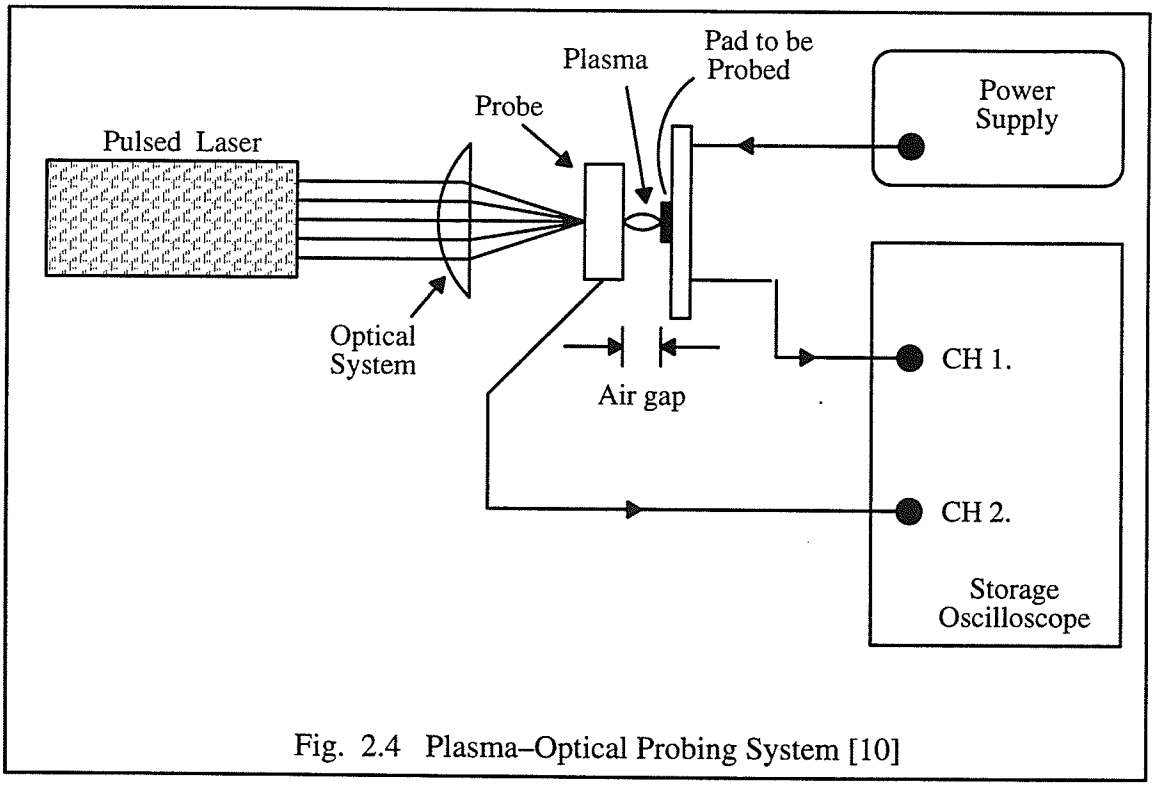

Fig. 2.4 Plasma–Optical Probing System [10]

In a related technique, the change in phase of a laser beam, as it passes through a material, is monitored. This change in phase is proportional to the volume and potential

of the material [11]. This technique yields the space–charge density in the material and therefore does not provide a direct measure of the test point voltage.

2.5 Electro–Optic Probing

The physical basis of this optical probing technique is the electro–optic effect, in which the presence of an electric field across an appropriate substrate induces a field–dependent birefringence in the substrate. The birefringence effects an optical beam by altering its state of polarization. If the field is caused by a voltage on a device or interconnect, the change of polarization of the probe beam can be related directly to the voltage. When the optical probe beam is a train of ultrashort (picosecond duration) pulses, very high–speed voltage waveforms can be resolved, because the pulses act as sampling gates [12,13].

Electro–optic sampling requires a substrate that exhibits a linear electro–optic effect. Semiconductor materials, such as GaAs and InP, are electro–optic in nature whereas silicon is not. Several different electro–optic (EO) probing configurations are possible. One configuration uses an external EO crystal, typically lithium tantalate, $LiTaO_3$, either in direct contact with the GaAs substrate, or in close proximity, to sample the fringing electric field lines above the substrate. This external electro–optic sampling scheme is shown in Fig. 2.5(a). A second approach, which eliminates the need for an external EO probe crystal, is used when the DUT is fabricated on a substrate that is itself electro–optic in nature. When a laser beam passes through the substrate that has electric fields set up by transmission line voltages, the optical E–field induced birefringence causes a polarization change proportional to the sampled voltage. This approach is shown schematically in Fig. 2.5(b). A generalized schematic for measurement of waveforms on an IC (by direct electro–optic sampling) using electrical excitation is shown in Fig. 2.6.

Electro–optic sampling has been applied to to the evaluation of discrete devices, packaged ICs, and ICs in wafer form. This technique is capable of measuring electrical signals with a temporal resolution below 1 ps and sensitivity below 1 $mV/(Hz)^{1/2}$. Electro–optic sampling has also been used for two–dimensional substrate internal field mapping of monolithic microwave integrated structures [14]. This kind of measurement allows the analysis of complex MMICs.

Although most of the electro–optic sampling systems use pulsed laser source for making sampling measurements, recently a CW optical probing method has been pro-

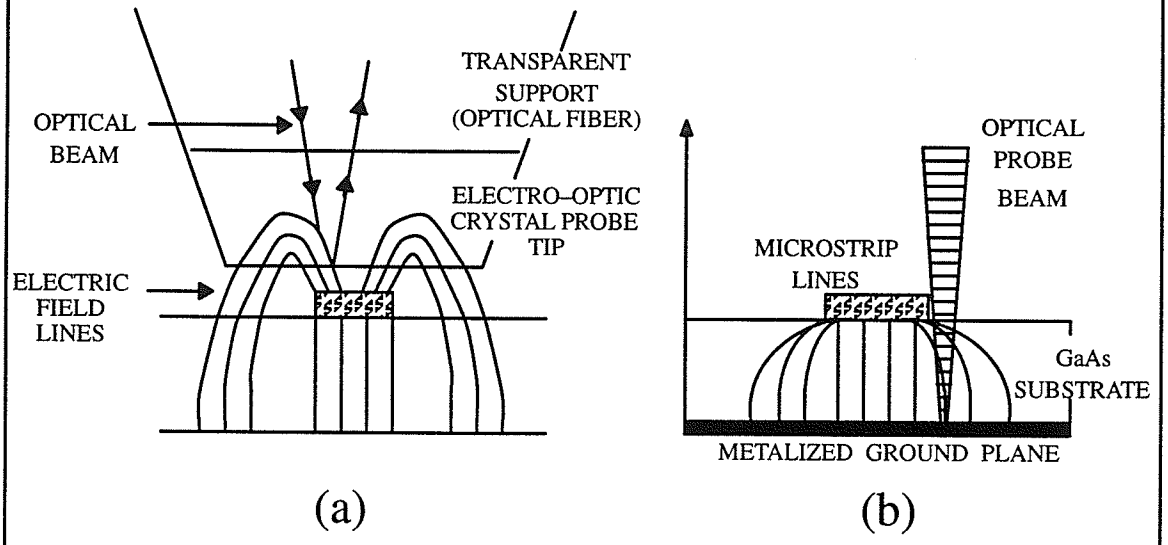

Fig. 2.5 Electro–Optic Probing Configurations (a) External electro–optic probe (b) Direct probing [7]

posed [15]. A CW optical probing signal associated with a fast photodetector gives the results directly in the frequency domain which may have applications in the testing of microwave integrated circuits. It also offers enhancement in sensitivity over the sampling system by the presence of a Fabry–Perot effect due to the continuity of the probing beam.

For direct–probing experiments, the creation of free carriers by absorption of the probe beam is a potential cause of invasiveness. On the other hand, capacitive loading is a potential problem for the external probing scheme. Because the external crystal of $LiTaO_3$ has a large dielectric constant (ε~45), it will disturb the electric field in the half plane above the IC being tested and may affect the operation of the DUT. Experimental results indicate that for optimum measurement accuracy and minimum invasiveness of the probe, the electro–optic crystal should be no thicker than the extent of the microwave coplanar transmission line guided mode [16].

The electro–optic modulation of the probe beam is proportional to the difference in potential between the front and back surfaces of the electro–optic substrate. The potentials are due to electric fields emanating from all contacts on the DUT, not just from the contact being probed. Thus, if the field from a nearby line is sufficiently

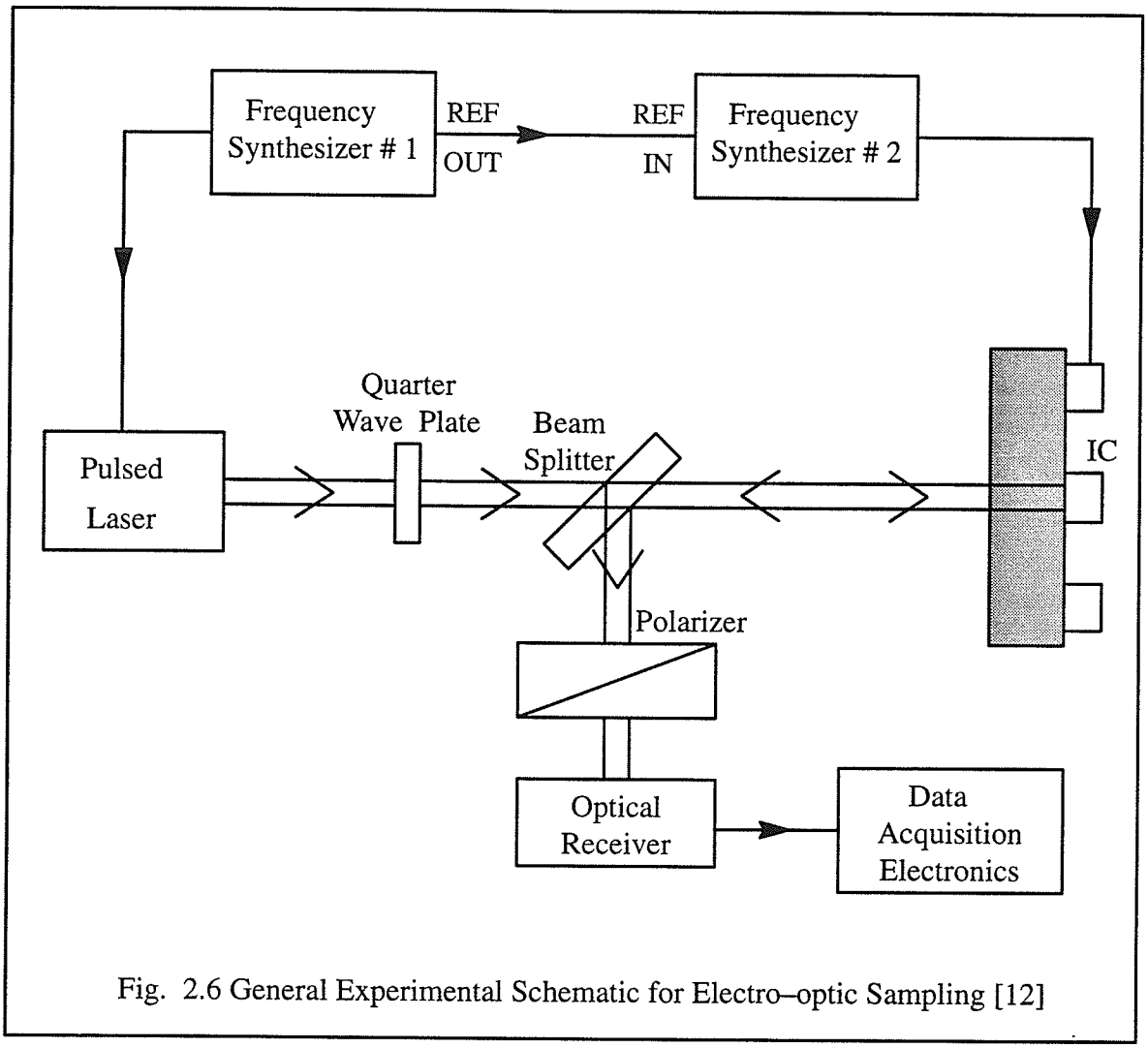

Fig. 2.6 General Experimental Schematic for Electro–optic Sampling [12]

strong at the spatial position of the probe beam, the signal from the nearby line will also be sampled by the probe beam. This leads to electro–optic cross–talk, which may exist even when there is negligible electrical crosstalk on the device [12].

2.6 Near Field Probing

Various types of electromagnetic probes can be used to directly couple to the electric and magnetic fields associated with the circuit under test. These probes offer a simple measurement technique when used in conjunction with a network analyzer.

The centre conductor of a coaxial cable has been used to measure the local charge and potential by capacitively coupling to a microstrip under test [17]. The coaxial

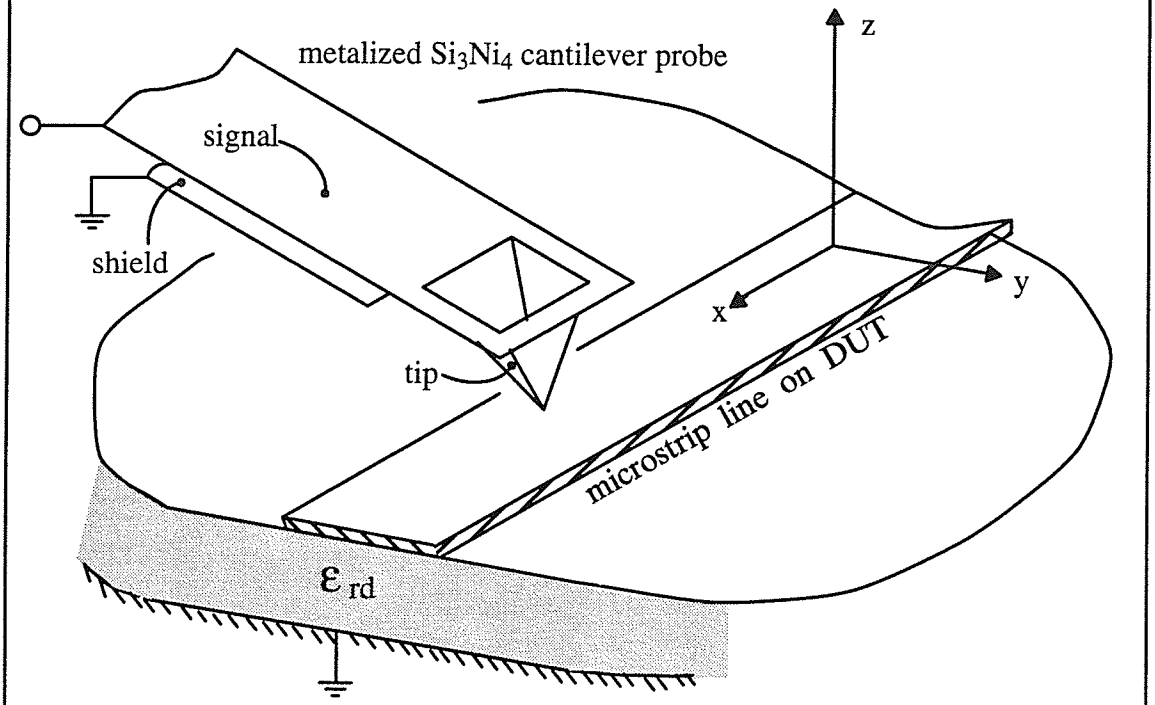

Fig. 2.7 Capacitively Coupled Probe Structure [19]

probe essentially measures the vertical component of the electrical field close to the surface of the DUT which is related directly to the charge/potentials. The best results were obtained when the circuit was shielded to eliminate spurious coupling to the probe circuit. This is a serious limitation of the technique.

Fig. 2.7 shows a micromachined probe used for reactive near–field probing. The capacitive coupling between the probe and the circuit induces a signal in the probe. The relative induced signal amplitude and phase is measured which is then related to the signal on the circuit under test. To obtain accurate magnitude and phase results, the technique requires that the coupling capacitance between the printed line and the probe is known accurately [18,19].

Alternately, a non–contacting magnetic field probe could be used for measurement of amplitude and phase at internal points of a circuit [20]. Fig. 2.8 shows how the double–loop magnetic field probe couples to magnetic fields of a microstrip and a

coplanar waveguide. To reduce pickup from adjacent lines, the probe dimension has to be reduced which reduces the sensitivity of the probe.

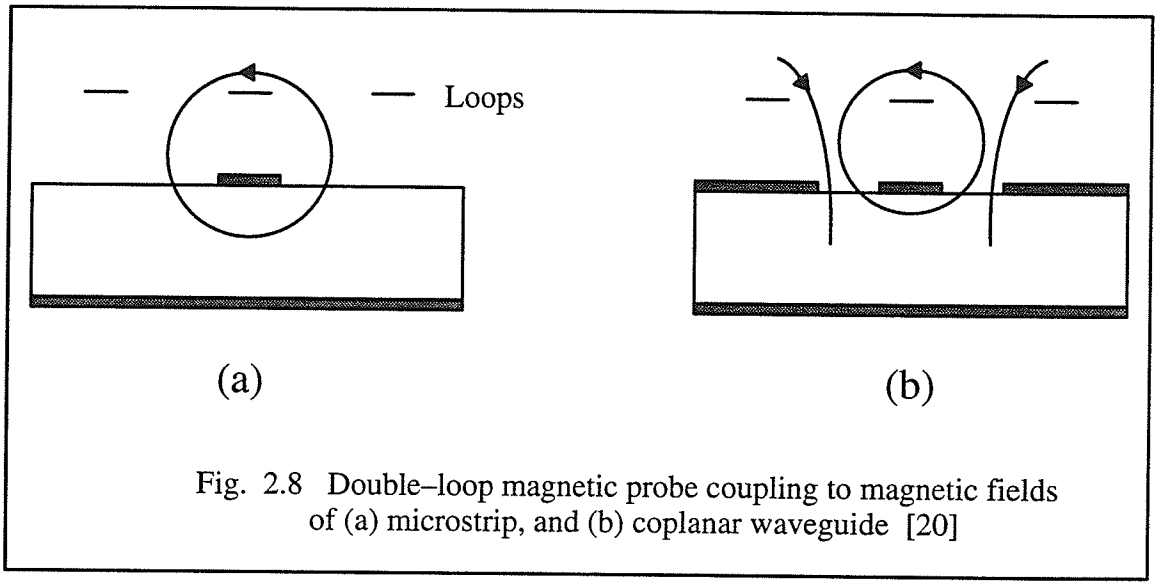

Fig. 2.8 Double–loop magnetic probe coupling to magnetic fields of (a) microstrip, and (b) coplanar waveguide [20]

This technique requires complex calibration as well to accurately determine amplitudes. The probes tend to disturb the circuit under test. The probe's sensitivity is limited by radiation picked up from other elements in the circuit. Unwanted capacitive coupling is another problem in the magnetic field probe. Often two measurements are required by rotating the probe and then averaging the measured data. Certain portions of the circuit, where high VSWR are encountered, are more prone to measurement errors.

The advantage of the reactively coupled techniques is that the probes are simple devices that are capable of useful measurements on planar circuits. These probes can be used on prototype circuits to verify circuit operation and find defects.

2.7 Direct Contact On–Wafer Probing

On–wafer probing is a contact measurement technique usually used at microwave frequencies. The need for wafer probing at microwave frequencies has arisen from the push for cheaper, high volume microwave components for military, consumer and commercial applications. Microwave probing of active and passive devices aids the data gathering process for both engineering database accumulation and process monitoring [21]. Measurements up to 50 GHz have been made on GaAs FETs [22].

To substitute for the I/O connections normally provided by the packaged devices, high frequency probes are used to test the terminal characteristics of the DUT directly on the wafer. Testing at GHz frequencies requires controlled–impedance signal lines, low inductance ground contacts and state of the art 50 ohm probes [23]. The basic reason for using a 50 ohm probe is to control the characteristic impedance down to the wafer connection. Some approaches which have been used include (a) sharpening the center conductor of a micro–coax line (b) attaching very short probe needles to microstrip lines and (c) defining coplanar contacts with microstrip or coplanar waveguides feeds on flexible or springy substrates.

Usually a coplanar waveguide probe is used as shown in Fig. 2.9. In a coplanar waveguide, the signal line and the two grounds are located adjacent to each other on the same side of the substrate. The center signal line is tapered in width to match the device–pad size. Direct contact to the wafer is then made at the tip of the coplanar waveguide [24]. This avoids the problems associated with inductive needles. Contact to the device is made at bumps (2 mils $\times$ 0.5 mils). The low common–lead inductance of this configuration also leads to low radiation and crosstalk. The main disadvantage of these probes is that owing to their large size, only a limited number of them can be used on a circuit.

These wafer probes are commercially available and have been used for FET, passive elements and MMIC characterization.

The circuits being tested have to be specially designed with wafer probing in mind. Problems arise when microstrip inputs and outputs are used where there are no contacts to the ground plane near the ends of the microstrip lines. Such a circuit cannot be accurately tested in wafer form since the electromagnetic fields cannot be launched properly down the microstrip lines. For accuracy in measurements in microstrip–style circuits, ground vias have to be fabricated next to desired test points. Again this also limits the testability to a small number of predetermined test points. Also, connecting the probe to an interior point of a circuit can greatly disturb the way the circuit operates. Fig. 2.10 shows the desirable device layout for on–wafer testability. The DUT connection pads that are expected to be probed at high frequency should be arranged for clean coplanar transitions to the probe. The DUT may be a discrete FET, an MMIC, a thin–film hybrid circuit, or any planar substrate with microstrip transmission lines. The ground and signal pads must be colinear for proper probe contacts.

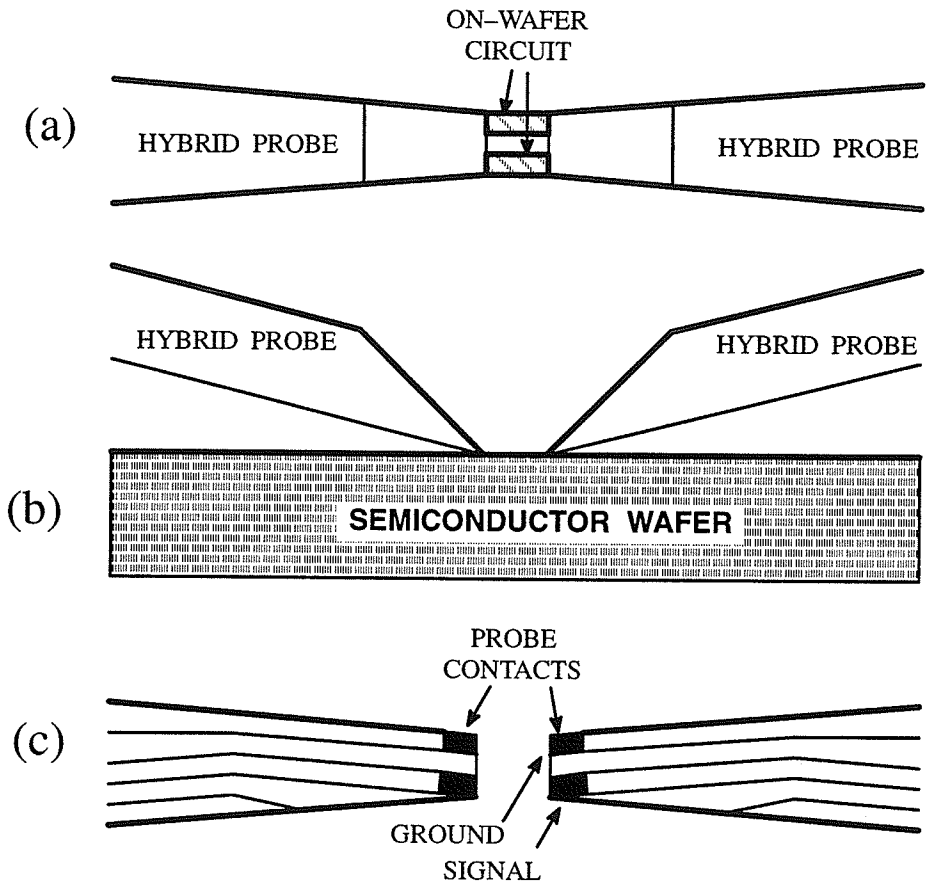

Fig. 2.9 Coplanar Microwave Probe Heads (a) top view
(b) side view and (c) bottom view [21]

This measurement technique requires extreme care by the operator in positioning the probes on the pads of the calibration standards and on the device under test. The way a bond pad is contacted directly affects measurement accuracy.

The probes described above are best suited for the planar structures encountered on ICs and achieve their highest bandwidth for the case when ground and signal pads are adjacent to each other at a predetermined separation. A "bird–beak" coaxial probe has been designed [25] that can be used for testing planar or non–planar structures with a range of pad separations. The probe was used to characterize the electrical properties of a lossy transmission line system up to 24 GHz. These probes have also been used to study low level coupled noise signals, and switching induced noise on power supply leads.

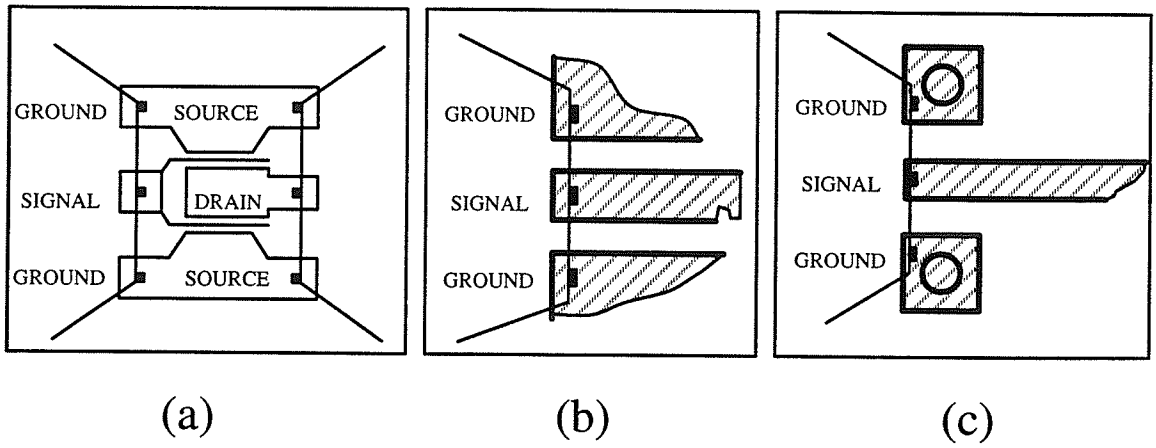

Fig. 2.10 Preferred Device Layout for mm–Wave On–Wafer Testability
(a) simple GSG FET pattern (b) Coplanar Launch and (c) Microstrip Launch [22]

In another implementation, two port on–wafer vector network analysis has been performed using active probes [26]. The active probes consists of monolithic GaAs directional TDR ICs mounted directly on low–loss microwave wafer probes. Nonlinear transmission lines (NLTLs) and NLTL–gated sampling circuits are used for the generation and detection of transient signals with a wide (> 100 GHz) bandwidth.

Recently on–wafer measurements have been demonstrated in the subpicosecond regime, where a nonlinear impedance transformer has been used to demonstrate a 500 GHz wafer probe [27].

CHAPTER 3

The Force Microscope

A brief history of the development of scanned probe microscopes is first presented. The electrostatic force microscope, the instrument used in present research, is then introduced. The components of the microscope are described next. Spatial resolution and sensitivity, which characterize the instrument, are described in the following section. Finally a description of the measurement schemes for the extraction of waveforms on the circuit under test is provided.

3.1 Scanned Probe Microscopes

In the last decade or so, a family of new microscopes have been developed that can map atomic and molecular shapes, electrical, magnetic and mechanical properties and even temperature variations on the surface of semiconductor materials at a much higher resolution than was possible earlier. These microscopes overcome the so called Abbe barrier which describes the fundamental limitation of any microscope that relies on lenses to focus light or other radiation: diffraction obscures details smaller than about one half the wavelength of the radiation. The resolution in the new microscopes is determined by the finest tip diameter and tip–sample gap spacing that can be achieved [28].

The first of these microscopes was the scanning tunneling microscope (STM). In the STM (Fig. 3.1), piezoelectric controls maneuver a fine tungsten tip, to within

a few nanometers of a conducting specimen – so close that the electron clouds of the atom at the probe tip and of the nearest atom of the specimen overlap. A small voltage applied to the tip causes the electrons to tunnel across the gap, generating a small tunneling current. The probe scans the surface in a raster pattern. As the probe is scanned, a feedback mechanism controls the piezoelectric so that the probe moves vertically to stabilize the current and maintain a constant gap between the microscopic tip and the surface. In this manner, the tip moves up and down in concert with the topography. Thus, the variation in the voltage applied to the piezoelectric are electronically translated into an image of surface relief. STM is capable of resolving individual atoms [29].

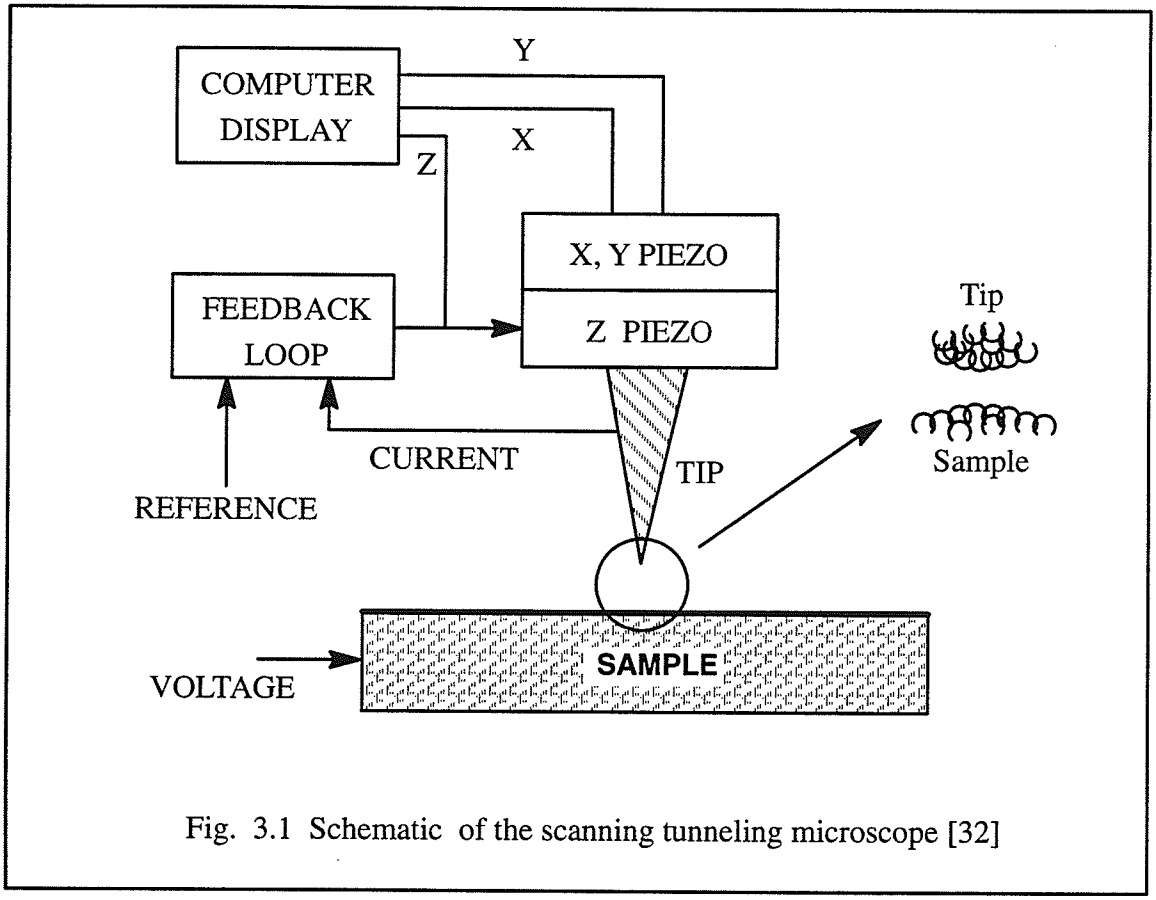

Fig. 3.1 Schematic of the scanning tunneling microscope [32]

The STM triggered the development of a whole family of scanned probe microscopes – based on similar technology. In the atomic force microscope (AFM), a conducting sample is not required. The tip is placed in direct contact with the surface with a specified force, similar to a record needle but very much sharper. Instead of using the tunneling current to measure how close the tip is to the surface, the deflection of a probe beam as determined with a fiber interferometer or laser beam deflection

sensor, is used. In this manner, the AFM records contours of constant interatomic forces as the tip is scanned on the surface. The AFM can image semiconductors and insulators as well as conductors. In the AFM, the repulsive forces involved in the imaging are sometimes large enough to disturb the sample.

In an extension of AFM, lateral deflection of the tip and frictional forces have been measured on an atomic scale [30].

In magnetic force microscope (MFM) [31], a magnetized nickel or iron probe is used to sense the magnetic force between the tip and a magnetic sample. The MFM can trace the magnetic field pattern emanating from data–recording heads at a resolution of better than 25 nm.

Scanning thermal microscope can measure surface–temperature variations of a ten–thousandth of a degree on a scale of tens of nanometers [32].

Another modification of the STM is the scanning tunneling potentiometer. In this technique, a bridge method is used to measure the spatial variation in potential across the sample as the tip is controlled and scanned so as to obtain surface potential simultaneously with the surface topography. An AC voltage (typically a few kHz frequency) is applied between tip and sample which generates an AC tunnel current. The amplitude of this current is then used to control the tip–sample spacing. An independent control loop, whose band (DC to 1 kHz) is outside the band of the gap control loop, is used to maintain zero DC tunnel current by continuously causing the voltage on the tip to track the voltage on the sample as the tip is rastered across its surface. The tip voltage is then equal to the sample voltage at every point on the surface. This technique is useful for measuring nanometer scale potential variations on devices such as Schottky barriers, pn–junctions and heterostructures. The voltage resolution is typically on the order of a few millivolts [33].

Scanning tunneling potentiometry has been used to provide information about the electrical properties at semiconductor junctions and inversion layers, microscopic potential distribution across a double heterojunction (DH) AlGaAs laser structure. Potential distribution under operating conditions and related properties, such as the extent of space charge regions next to p–n and material junctions, can be measured. The potential distribution across the cleaved end face of a forward–biased GaAs double heterojunction laser diode was mapped using STP [34].

3.2 Electrostatic Force Microscopes

In the electrostatic force microscope, an AC voltage is applied between tip and sample and the induced force is measured. The force is proportional to the square of the applied voltage V^2 times the rate of change of tip–sample capacitance with spacing, $\partial C/\partial z$.

The force microscope has been used to deposit and image localized surface charge on insulators as shown in Fig. 3.2 [35]. If local charge is present on a surface, the tip feels, in addition to the van der Waals force, an additional attractive force due to the Coulomb attraction of the charge to its image charge in the tip. The resulting force gradient contour has a peak at the location of the charge. In one study, the charge was deposited on a PMMA substrate by applying a negative voltage pulse onto the tip, and its decay with time was imaged with the EFM . The deposited charge was estimated to be around 1200 electrons. With further refinements, it has been possible to observe discrete steps in the force versus time curve corresponding to the discharge of single charge carriers during the decay process. In an improved mode of charge sensing, the charge and topography are distinguished and the sign of the charge is determined in a single scan [36].

Contact electrification has also been studied using the force microscope with a view to study its mechanism. The microscope has 0.2 μm lateral resolution and the sensitivity to detect 3 electron charges [37].

Ferroelectric domain walls in the ferroelectric–ferroelastic material have been imaged using force microscopy. Ferroelectric materials are of interest because of a switchable polarization state. In ferroelectrics, the microscope is sensitive to the stray electric field emanating from the surface and is thus non–destructive. The force gradient due to the polarization change at the sample surface has been imaged. The signal changes sign at the domain wall because of the reversal in sign of the polarization across a wall [38].

The EFM has also demonstrated the capability to image the migrating surface ions on Si_3Ni_4 in fringing lateral fields. This study is important since such migration of surface ions can modify the electrical characteristics of underlying semiconductor structures causing device instabilities [39].

The capacitance measurement technique can be used to map dopant profiles in semiconductors. A voltage is applied across the gap between the probe of an EFM

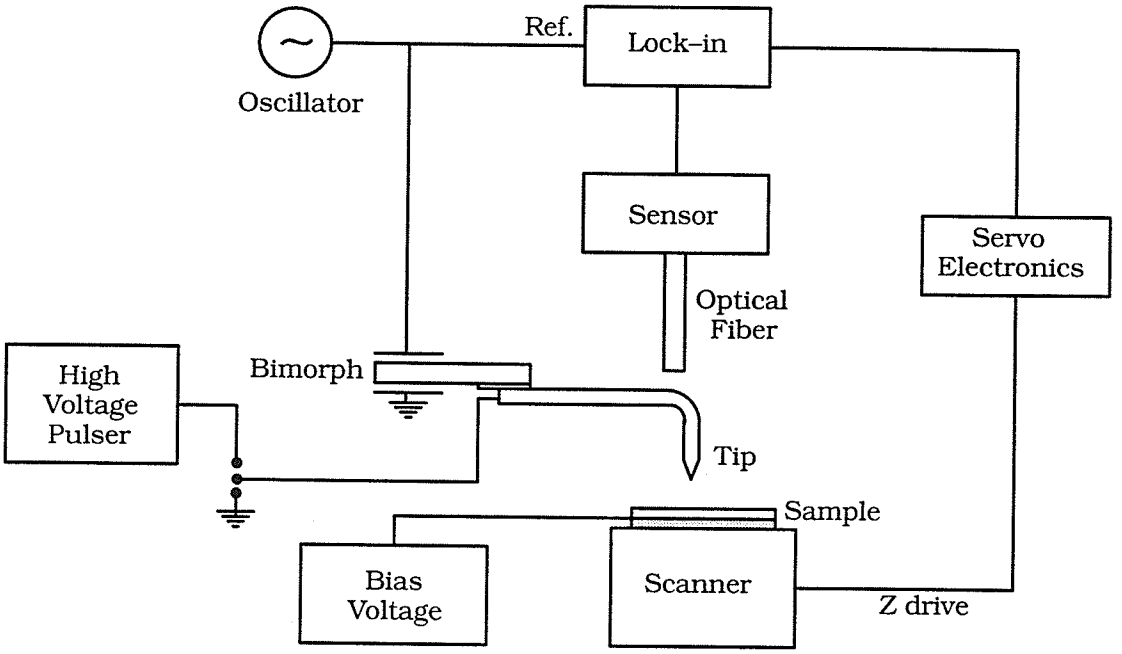

Fig. 3.2 Surface charge measurement with the electrostatic force microscope [35]

and the surface. The voltage mobilizes the conduction electrons or holes beneath the probe, leaving a charged region that exerts an electrostatic force on the tip. The consequent movements of the tip provide a measure of the charge and hence of the number of mobilized electrons or holes and the concentration of dopant atoms. The dopant profile of the active regions of a cleaved MOSFET structure has been mapped in this way by scanning at a fixed bias voltage. A schematic of the instrument is shown in Fig. 3.3. The typical dopant densities varied from 10^{16}/cc in the gate region to 10^{20}/cc in the n^+ source and drain regions [40].

The scanning force microscope has also been used for the measurement of contact potential difference with high spatial resolution. The contact potential difference (CPD) between two materials depends on a variety of parameters such as the work function, adsorption layers, oxide layers, dopant concentration in semiconductors, or temperature changes on the sample. For many decades, the common method of measuring the

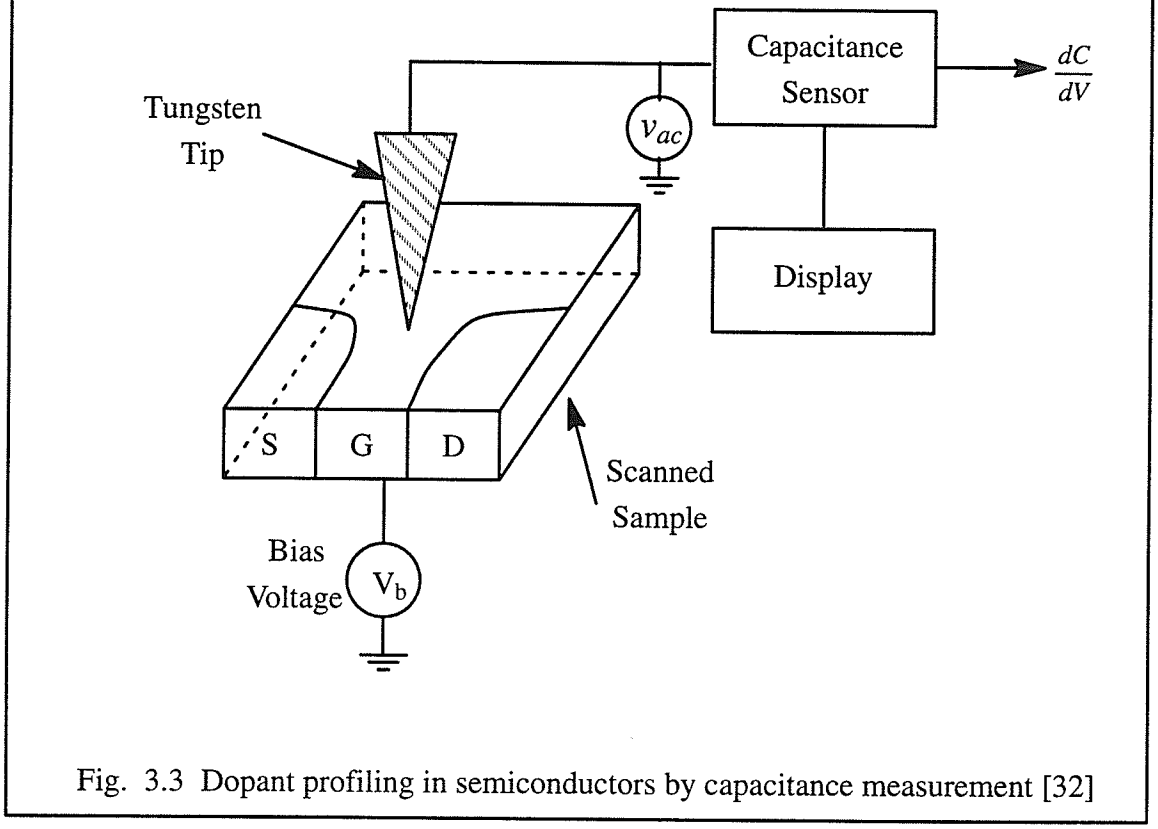

Fig. 3.3 Dopant profiling in semiconductors by capacitance measurement [32]

CPD has been the vibrating capacitor method or the Kelvin method [41]. In the Kelvin method two conductors are arranged as a parallel plate capacitor with a small spacing. The Kelvin method has a high sensitivity for potential measurement but integrates over the whole plate area and does not provide a high resolution lateral image of the variation of the CPD on the surface. The vibrating capacitor technique relies on the measurement of an AC signal. Spurious AC signals, unrelated to the contact potential, mixed in with genuine signals will result in measurement error. Microphonic signals generated by vibration in the system is one source of such spurious signals [42].

Recently, scanning force microscope has been used to measure CPD. Images of gold, platinum and palladium surfaces, taken in air, indicate CPD on the order of 90 mV for Pt on gold and 65 mV for Pd on gold [43,44].

The imaging of lateral distribution of CPD has industrial application in minimizing residual contamination for cleaning processes in semiconductor technology.

3.3 Electrostatic Force Microscope – The Instrument

In the electrostatic force microscope, a probe is positioned over a sample and it vibrates under the influence of an electrostatic force acting between the probe tip and the sample.

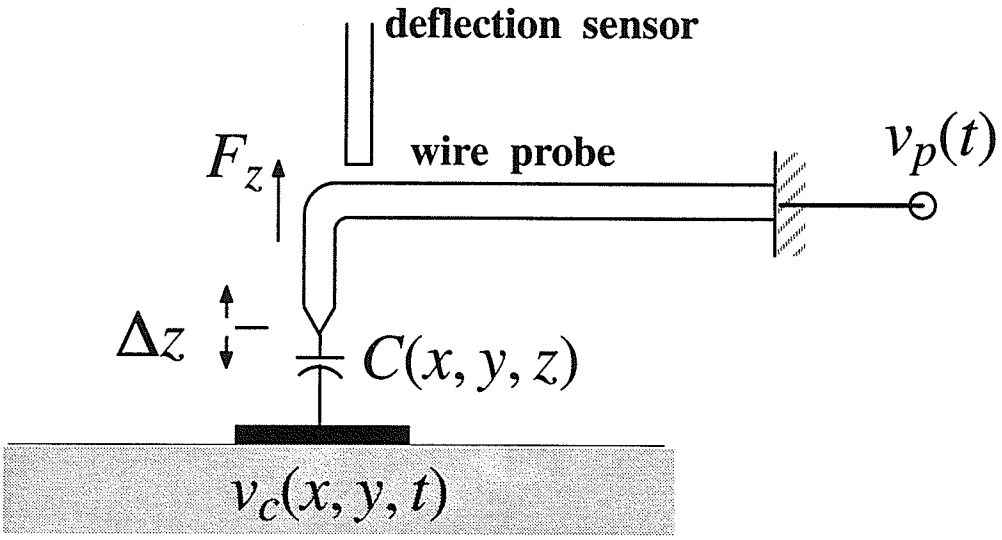

Fig. 3.4 Principle of the Electrostatic Force Microscope

The operating principle of this microscope is illustrated in Fig. 3.4 where the localized signal $v_c(x,y,t)$ on an integrated circuit is to be measured. The circuit signal is extracted by sensing the deflection of a small probe due to the electrostatic force between the tip of the probe and the point on the circuit being monitored. In our instrument a conducting wire, which has sharp tip at its end, is used as the probe and is externally driven by a controllable voltage $v_p(t)$. The probe tip is held in close proximity to the location on the circuit surface at which the signal $v_c(x,y,t)$ is to be extracted. The probe tip and circuit test point form a small localized capacitor $C(x,y,z)$ which charges up when there is a potential difference between them, thus producing an attractive force. The force acting on the wire probe can be deduced from the stored energy on the capacitor as

$$F_z = \frac{1}{2}\frac{\partial}{\partial z} C(x,y,z)\left[v_p(t) - v_c(x,y,t)\right]^2 \qquad (3.1)$$

Here the capacitance between the probe and the circuit $C(x,y,z)$ is a non–linear function dependent on the probe tip–circuit geometry and position z above the circuit surface.

The force on the cantilever probe (3.1) produces a mechanical deflection Δz which is monitored using a deflection sensor described later in this chapter. The deflection will be a function of the cantilever's mechanical properties and the driving frequency of the applied force.

The main components of the electrostatic force microscope are the following :

- The cantilever probe
- Deflection sensor
- The electronics for generating appropriate signals

While the first two remain the same, the signal electronics depends on the individual measurements that are performed. The mechanical properties of the cantilever probe that are relevant to the measurements are described next, followed by the description of the deflection sensor. The signal electronics is described later in the next two chapters along with the measurement results.

3.3.1 Cantilever Probe

In scanned probe microscopes, a probe is used to sense the force. The deflection amplitude of the probe depends on its mechanical properties such as the spring constant, resonant frequency etc. and associated Q factors. The probe can be either a simple wire or a more complicated micromachined cantilever typically used in AFM studies. Since a wire probe has been used in the present research, mechanical properties of only the wire probe are detailed.

The spring constant for a cantilever with uniform cross–section along its length is given as [45]

$$k = \frac{3EI}{l^3} \qquad (N/m) \tag{3.2}$$

where E is the Young's modulus of elasticity (N/m^2), I is the area moment of inertia and l is the length of the cantilever. For a cantilever of circular cross section and radius r, such as the wire probe used in our experiments, the area moment of inertia is given by

$$I = \frac{\pi r^4}{4} \qquad (m^4) \tag{3.3}$$

Substituting for I in (3.2), the spring constant of a cantilever becomes

$$k = \frac{3\pi E r^4}{4l^3} \tag{3.4}$$

The cantilever is capable of vibrating under the influence of an externally applied force. For a cantilever fixed at one end and free at the other, the resonance frequency is given by

$$\omega = \sqrt{\frac{k}{m_{eff}}} \tag{3.5}$$

$$\text{where} \quad m_{eff} = 0.24m_d + m_c$$

m_d is the distributed mass of the cantilever and m_c is the concentrated mass at the end of the cantilever.

When the cantilever vibrates under the influence of an externally driven force of unit amplitude, at a frequency ω, the amplitude of vibration is given by

$$A(\omega) = \frac{(\omega_0/\omega)\ Q/k}{\sqrt{1 + Q^2\left(\frac{\omega_0}{\omega} - \frac{\omega}{\omega_0}\right)^2}} = \frac{A_0(\omega_0/\omega)}{\sqrt{1 + Q^2\left(\frac{\omega_0}{\omega} - \frac{\omega}{\omega_0}\right)^2}} \tag{3.6}$$

where ω_0 is the resonant frequency of the probe and A_0 is the vibration amplitude when $\omega=\omega_0$ and is given by $A_0=Q/k$.

The expression for resonant frequencies and the amplitude of vibration at a frequency ω are sufficient to characterize the wire probe. In our instrument, a Molybdenum wire of diameter 127 μm is used. Typical length of the probe is 10 mm with the last 2 mm bent at a 90^0 angle to form a tip. Using (3.4) and (3.5), we can determine k = 22.5 N/m and $f_r \approx 1100$ Hz. To determine the resonant frequency and Q experimentally, the probe is externally driven at various frequencies by applying a sinusoidal voltage $v_p(t)$ to the structure shown in Fig. 3.4. The deflection is then measured at each of these frequencies. A normalized plot of one such measurement is shown in Fig. 3.5. The resonant frequency for this particular probe is determined to be 1422 Hz. The quality factor Q can be determined using (3.6). With the experimentally determined value of ω_r, the Q in (3.6) is adjusted to fit the curve. Thus Q is determined for this probe to be 282.

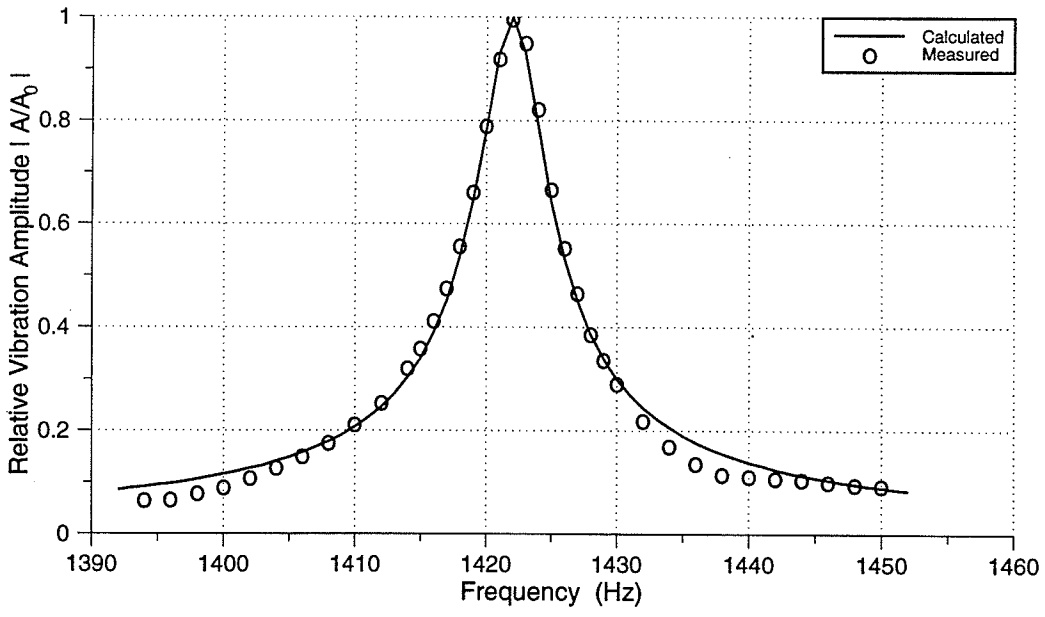

Fig. 3.5 Mechanical response of the cantilever probe as a function of frequency. The theoretical result is calculated using (3.6) with f_r = 1422 Hz, Q = 282.

3.3.2 Deflection Sensor

In the original AFM design, the probe's deflection was measured by the tunneling current flowing between the probe and an STM tip mounted just above it.

Another scheme to measure tip deflection is using a laser beam that is reflected off the probe. Movement of the probe shifts the path of the reflected beam, so that a position sensitive split detector placed in the beam path some distance away can detect tiny movements of the probe. An optical sensor provides a more reliable measure of tip deflection than the tunneling sensor. The optical beam deflection method is widely used in laboratory and commercially available AFMs.

In an interferometer based position sensing, a laser beam is split into a reference beam, and a probe beam partially reflected by the back of the cantilever. The reflected beam is recombined with the reference beam, and they interfere with each other to yield a beam whose phase is sensitively dependent on the path length of the probe beam. The phase shifts back and forth with each excursion of the tip : the extent of the shift reveals the amplitude of vibration. In this way the interferometer can detect amplitude changes as small as 10^{-5} nanometer.

Analysis has shown that the optical beam deflection method and the interferometer have essentially the same sensitivity [46]. This result has been explained by the physical equivalence of both methods.

The deflection sensor used in the present research is a super luminescent diode (SLD) based optical fiber interferometer. This is similar to a standard interferometer based system except that a SLD is used instead of a laser for the coherent source. The technique used in fiber–optic interferometers to measure the deflection of the cantilevers is outlined in Fig. 3.6. Light from a laser is launched into a fiber and then through a 2×2 directional coupler to a cleaved fiber end. When the light reaches the air–fiber interface, part of the light is reflected back into the fiber. The remainder of the light is transmitted into the cavity between the fiber and the cantilever. Here it repeatedly reflects between the cantilever and the fiber. A portion of the light reflecting off the cantilever and back into the fiber will interfere with the light reflected from the fiber–air interface. The total power reflected back into the fiber will depend on the phase difference between these two waves and thus on the dimensions of the cavity. The total reflected light travels back to the directional coupler where half the power goes to a photodiode detector and half back to the laser source. The output

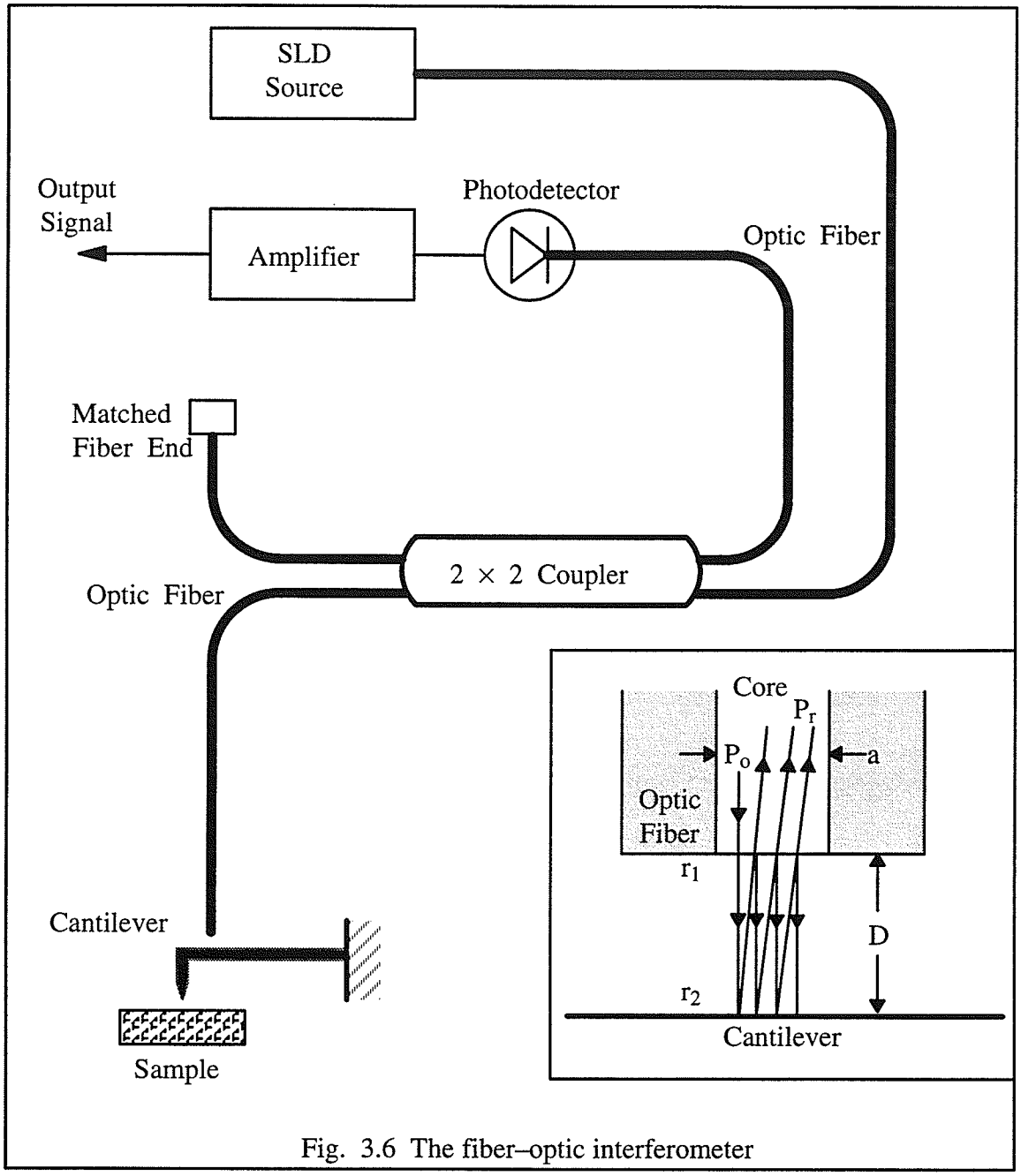

Fig. 3.6 The fiber–optic interferometer

signal, now a function of the fiber–cantilever spacing, is the photocurrent measured at the photodiode.

For small separation between the fiber and the cantilever, the reflected power can be estimated using the equation [47]

$$P_r = P_o \frac{(r_1^2 + r_2^2) - 2r_1 r_2 \cos(4\pi D/\lambda)}{(1 + r_1^2 r_2^2) - 2r_1 r_2 \cos(4\pi D/\lambda)} \tag{3.7}$$

where r_1 is the reflection coefficient of the fiber–air interface, r_2 is the reflection coefficient of the air–cantilever interface, D is the separation between the fiber and the cantilever and λ is the wavelength of the optical source. Equation (3.7) suggests that as the separation between the fiber end and the cantilever is changed, the argument of the cosine term will change, going through a minima (P_{min}) and a maxima (P_{max}) in reflected power. These minima and maxima correspond to points of destructive and constructive interference of the incident and reflected beams. This is shown in Fig. 3.7 where the ratio of reflected to incident power versus phase angle $4\pi D/\lambda$ is plotted for several values of r_2. r_1 is set to 0.2 which is typical for an air–glass interface. Visibility can be defined as

$$V = \frac{P_{max} - P_{min}}{P_{max} + P_{min}} \tag{3.8}$$

The visibility can be used as a measure of usefulness of the interferometer. If r_1 = 1 then V=0 and a useful signal, indicating variations in cavity spacing D, will not be derived. If r_1=0, then again V=0 and again no useful signal is derived. For a useful signal to be derived, r_1 has to be between these limits.

Equation (3.7) can be corrected to account for the losses due to the refraction of the optical signals at the end of the fiber. When the optical signal exits the fiber, it becomes divergent with an half angle of the order of 5^0–10^0. To correct for this effect, r_2 can be made a decreasing function of D. This highlights one of the limitations of the fiber optic interferometers. Since a reasonable amount of optical signal must couple back into the fiber to form a signal, the separation between the fiber and the cantilever cannot be too high. Typically the separation between the fiber and the cantilever is less than 100 μm (~100λ). This can cause some practical problems in the alignment of fibers with cantilevers.

The use of a diode laser source and the all–fiber construction results in smaller size, improved mechanical robustness and reduced heat dissipation. Since there is no air–path between optical components (except for the micron–sized path to the cantilever), the instrument is much less susceptible to instabilities caused by air currents

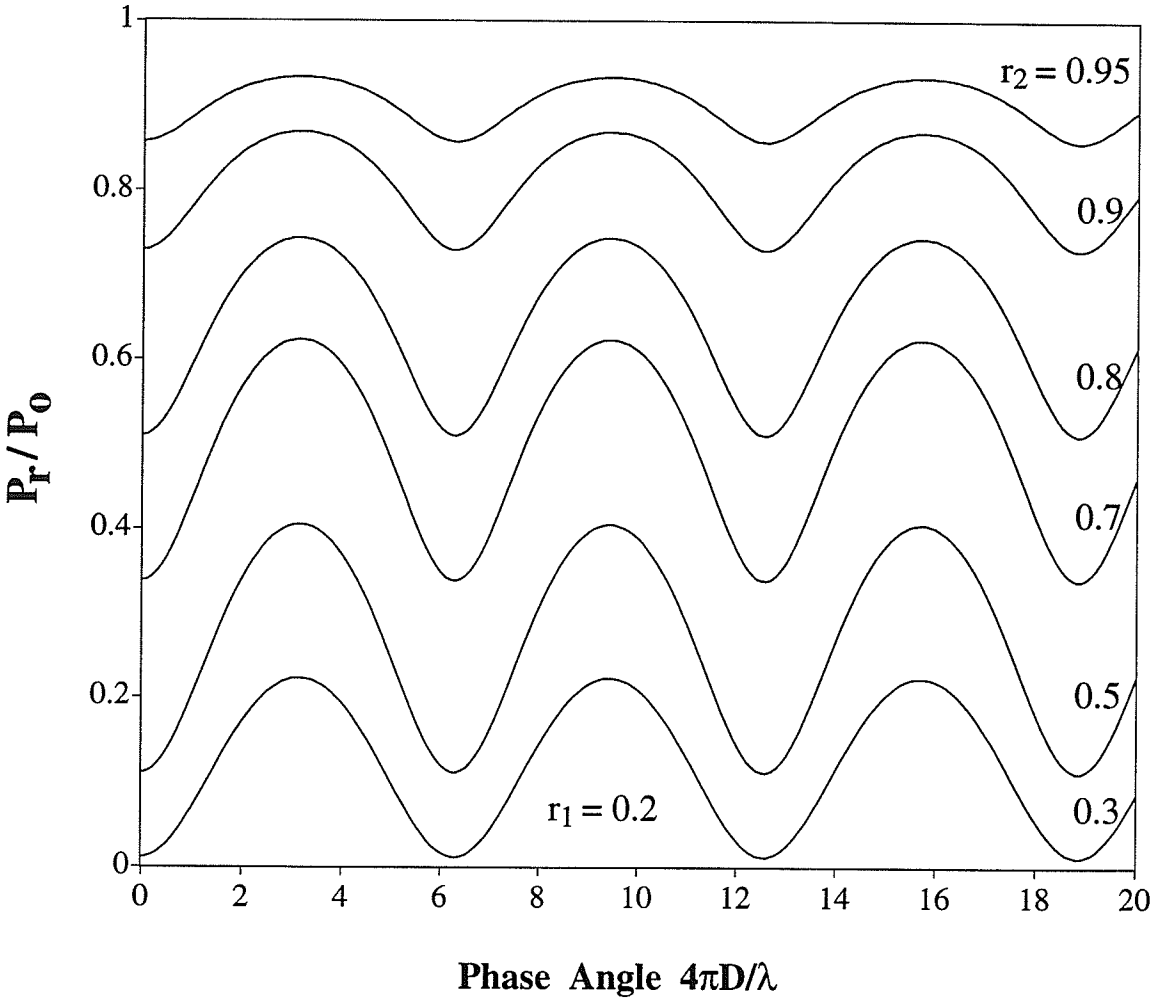

Fig. 3.7 Ratio of the interferometer's output power to the incident power as a function of phase angle for air–glass interface (r_1=0.2) and different values of r_2.

and acoustic noise. Also since the response of the directional coupler depends only weakly on polarization, birefringence introduced by fiber bends will not disturb the operation of the sensor.

A feedback–controlled fiber interferometer has previously been used for the measurement of the deflection of the cantilever. With the feedback control, the influence of thermal and mechanical drifts or fluctuations is minimized [48]. Systems of this type described above have been built using laser diodes and He–Ne laser sources. These systems have displayed noise levels below 0.1 Å over a 0.1–1000 Hz bandwidth with a noise level of 5×10^{-4} Å/(Hz)$^{1/2}$ @ 1000 Hz [49]. These laser based interferometers have been used for a variety of measurements including atomic resolution imaging

of graphite and magnetic force imaging. However, some difficulties have been experienced with the operation of these systems. Lasers contain regions with optical gain, thus making them sensitive to the optical feedback the interferometer generates as part of its normal operation. The main effect of the feedback is to produce noise that is eventually translated into errors in deflection measurements.

The super luminescent diode based interferometer used in the present research overcomes the problem of optical feedback [50]. The SLD is a light emitting diode (LED) which does not contain regions with optical gain and is therefore insensitive to optical feedback. The major disadvantage of using SLD as a source is that it has a much wider spectral content than a laser source. The noise for this interferometer was measured to be 0.03 nm in a 0.1–5000 Hz bandwidth and 10^{-4} nm/(Hz)$^{1/2}$ at frequencies above 400 Hz [50].

3.4 EFM Characterization

Spatial resolution and sensitivity are the two main criteria by which the electrostatic force microscope can be evaluated. A brief description of the two measures are described next.

3.4.1 Spatial Resolution

Resolution implies that something is being resolved. It may be atoms on a surface or cracks in a mineral surface. Different tasks have different definitions tailored to them.

Resolution of the EFM has been estimated analytically by modelling the electrical tip–DUT interactions. It is assumed that the effective force is caused solely by the tip–DUT voltage and depends on the tip–position [51]. In Fig. 3.8, the electrical force per effective area is shown for several working distances h versus the distance of DUT–tip. It is obvious that the spatial resolution decreases dramatically with the increase of the working distance h for a fixed SFM tip–DUT voltage. Assuming a fixed working distance, the spatial resolution can be defined as the diameter of the circle where the force per effective area decreases to 1/e–th part of its maximum. For the tip geometries shown in Fig. 3.8, it is estimated that the spatial resolution is three times the working distance.

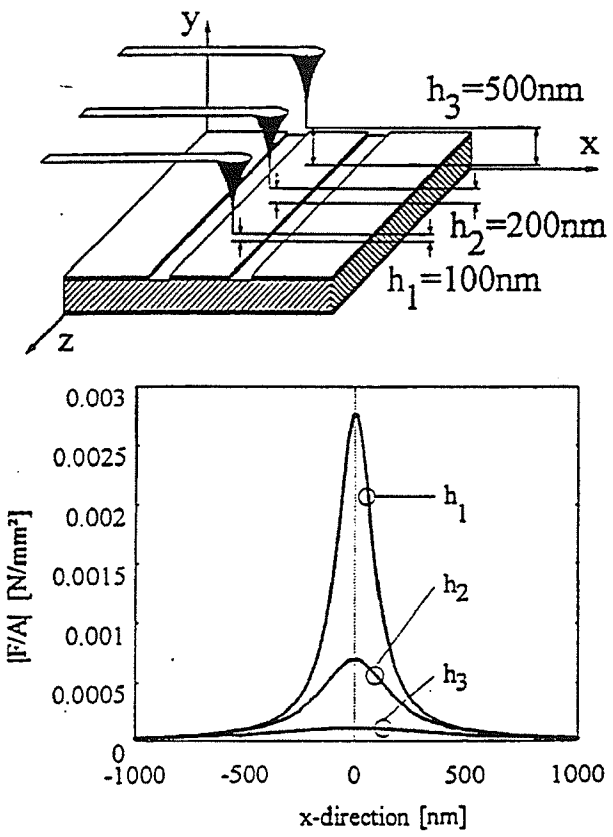

Fig. 3.8 The simulated force per effective area as a function of the working-distance h-(100 nm, 200nm,-500 nm) - versus position beyond the tip in nm (x–direction) [51]

In the EFM, the mutual interaction between the probe tip and a test point on the circuit surface is measured. This interaction is due to the coupling capacitance between the tip and the test point. The localization of the coupling capacitance determines the spatial resolution of the system. The coupling capacitance has been estimated using a static analysis of the tip–interconnect line structure over a ground plane. The numerically calculated capacitance derivative is shown in Fig. 3.9(a) [52]. This curve is plotted for a tip–line separation of 1 μm. The probe in this case is a wire structure similar in geometry to the ones used in our experiments. Using a half bandwidth at half maximum of the capacitance derivative criteria, the figure suggests a spatial resolution better than 4 μm should be possible.

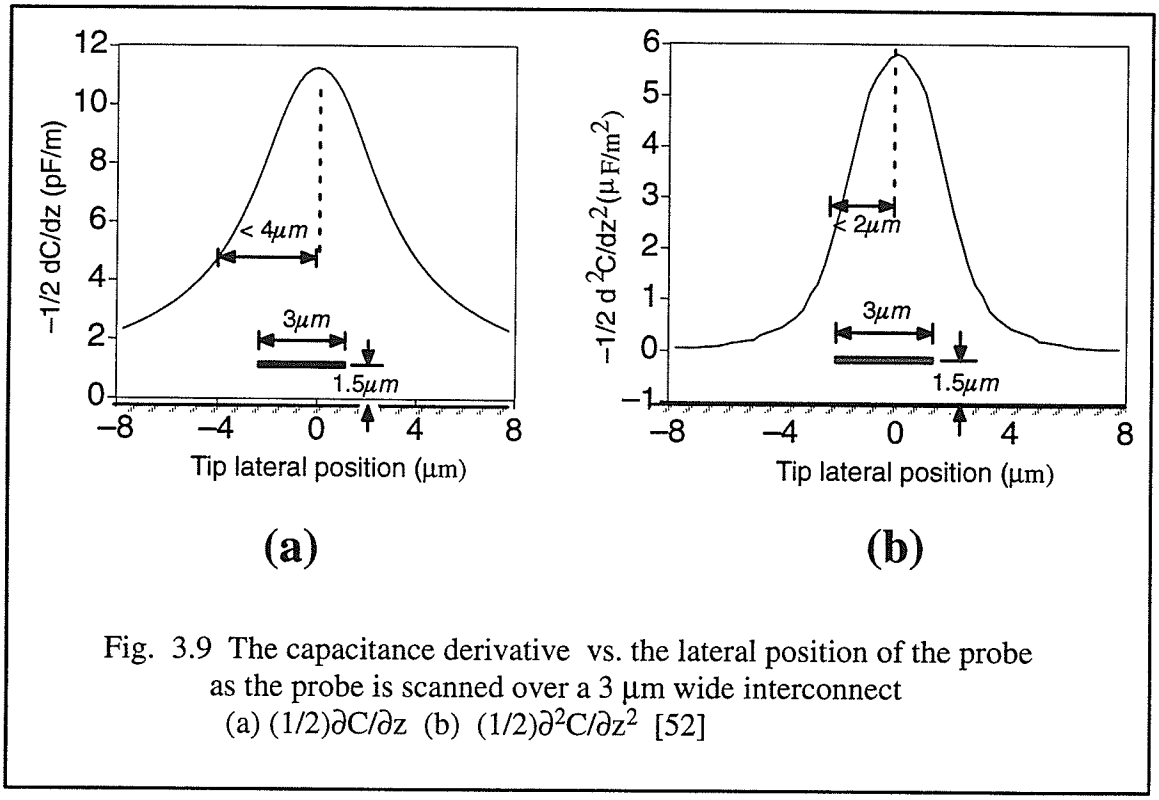

Fig. 3.9 The capacitance derivative vs. the lateral position of the probe as the probe is scanned over a 3 μm wide interconnect
(a) $(1/2)\partial C/\partial z$ (b) $(1/2)\partial^2 C/\partial z^2$ [52]

It is also predicted that the spatial resolution of EFM can be improved by using the force gradient deflection method [53]. The probe deflection in an EFM is proportional to the induced electrostatic force acting on the probe which in turn is proportional to the derivative of the coupling capacitance between the probe and the circuit under test. If instead, force gradient is monitored, a signal proportional to the second derivative of the capacitance $[(1/2)\partial^2 C/\partial z^2]$ is produced. Fig. 3.9(b) shows a plot of $[(1/2)\partial^2 C/\partial z^2]$ versus tip lateral position as the tip is scanned over the interconnect [52]. This figure suggests that force gradient method offers better spatial resolution.

3.4.2 Sensitivity

Sensitivity of the electrostatic force microscope is determined by the noise in the system. Two main sources of noise in the measurement system are

- Noise in the deflection sensor
- Noise due to thermal vibration of the cantilever probe

The deflection sensor utilized in the present research is a fiber optic interferometer. Hence, the noise in only this type of sensor is considered. The performance of properly

designed interferometer is limited by two types of noise. One is the shot noise arising from the random arrival of the photons at the detector surface and 1/f noise resulting from the low frequency change in the output power of the laser source. Other types of noise that may be significant in an actual instrument, like the 60/50 Hz electromagnetic interference can be eliminated by good design.

If the average optical power arriving at the detector is P_o, the associated shot noise is given by [45]

$$\Delta i_{SN} = \left(\frac{2q^2 P_o}{h\nu} \Delta f \right)^{1/2} \tag{3.9}$$

where hν is the photon energy and Δf is the bandwidth of the system.

Assuming the fiber interferometer is operated at the most sensitive operating point, this noise current can be translated into an equivalent noise amplitude given by

$$\Delta d_{SN} = \frac{\Delta i_{SN}}{S} \tag{3.10}$$

where S is the sensitivity of the detector i.e. the change in detected current per unit deflection of the cantilever, often expressed in terms of nA/nm.

Low frequency fluctuations in the optical output is a problem for many sources including semiconductor lasers and light emitting diodes (LEDs). This type of noise is commonly referred to as 1/f noise. It is typically a small percentage of the total optical signal.

The noise due to the interferometer sensor is on the order of 10^{-4} Å/(Hz)$^{1/2}$ [50] when the AC detector mode is used. This noise is very small when compared to the thermal noise of a typical wire cantilever which is considered next (in the range of 10^{-3}–10^{-1} Å/(Hz)$^{1/2}$ at resonance) [49].

The cantilevers used in electrostatic force microscopes have so little mass and are so highly resonant that thermal vibration of the cantilever is a major source of noise in these instruments. The thermally excited noise amplitude N of the cantilever at resonance has been shown to be [54]

$$N = \sqrt{\frac{4k_B TQB}{k\omega}} \tag{3.11}$$

where k_B is the Boltzman constant, B is the bandwidth of measurement system, ω is the resonant frequency of the probe, k is the spring constant of the cantilever, Q is the quality factor and T is the temperature of the cantilever.

This thermal noise puts limit on the measurement of the force or in turn the deflection of the cantilever. This expression can be used to derive the minimum detectable signal or the sensitivity that is theoretically possible.

In practice, many other sources contribute to the overall noise level. In scanned force microscopes, mechanical and acoustic vibrations are dominant factors. Mechanical vibrations can be greatly reduced by using an air–damped optical bench. In our instrument, we use a slab of granite on the inner tubes of car tires in conjunction with other damping mechanisms. Mechanical vibrations have a low frequency nature (< 100 Hz). Electronic noise is created by line pick–up and the power supplies from the electronics. The 60 Hz disturbance is the dominant factor, but also its harmonics contribute to the electronic noise [46].

3.5 Waveform Measurement Schemes

The signal on the circuit can be a DC potential, a slowly varying low frequency signal or a high frequency signal. This section on waveform measurement schemes refers to the way appropriate probe voltages are generated to measure these circuit signals. In what follows, it is shown how the circuit signals can be extracted by applying appropriate probe voltages. A heterodyne technique is employed to measure high frequency AC signals.

3.5.1 DC Measurement

In DC measurements, the circuit voltage that is to be measured is $V_c(x,y)$. Then (3.1), which gives the electrostatic force between the probe and the test point, can be re–written as

$$F_z = \frac{1}{2}\frac{\partial}{\partial z} C(x,y,z)\left[\, v_p(t) - V_c(x,y) + \Delta\Phi\right]^2 \qquad (3.12)$$

where the term $\Delta\Phi$ has been added to represent DC offset effects such as those due

to surface charge and contact potential difference between the probe and the circuit under test [41,43].

It is clear from (3.12) that the extraction of circuit potential $V_c(x,y)$ by directly measuring the force requires accurate knowledge of the capacitance derivative $\partial C/\partial z$ and thus very accurate positioning mechanism is required [55]. To overcome this problem, a nulling technique is utilized to extract the DC potential on the circuit [56,57]. To implement this nulling technique, the probe is driven with a voltage of the form

$$v_p(t) = A + K\cos(\omega_r t) \tag{3.13}$$

where A is a DC bias voltage and ω_r is the resonant frequency of the probe. Using (3.12) the force on the probe can then be written as

$$\begin{aligned} F_z &= \frac{1}{2}\frac{\partial}{\partial z}C(x,y,z)\left[\left(A + K\cos(\omega_r t)\right) - V_c(x,y) + \Delta\Phi\right]^2 \\ &= \frac{1}{2}\frac{\partial}{\partial z}C(x,y,z)\left\{\left[\left(A - V_c(x,y) + \Delta\Phi\right)^2 + \frac{K^2}{2}\right]\right. \\ &\quad \left. + 2\left[A - \left(V_c(x,y) - \Delta\Phi\right)\right]K\cos(\omega_r t) + \frac{K^2}{2}\cos(2\omega_r t)\right\} \end{aligned} \tag{3.14}$$

which results in a DC force term that will cause a static deflection of the probe beam, as well as force at frequencies ω_r and $2\omega_r$. By adjusting the DC probe voltage A so that the beam deflection at ω_r is nulled, the circuit voltage $(V_c(x,y)-\Delta\phi)$ can be extracted regardless of the unknown factor $\partial C/\partial z$. For small values of contact potential difference, this will yield the localized potential at the test point directly.

To monitor the force as specified by (3.14), the mechanical deflection of the cantilever is measured using a fiber interferometer. The deflection will be a function of the probe mechanical properties, the electrostatic force and its driving frequency. Deflections which are small compared to the length of the cantilever can be assumed to be a linear function of the applied force. In the static case, the deflection will simply be proportional to the applied force $\Delta z = F_z/k$, where k is the spring constant of the cantilever. For the dynamic case, the probe can be modelled as a damped harmonic

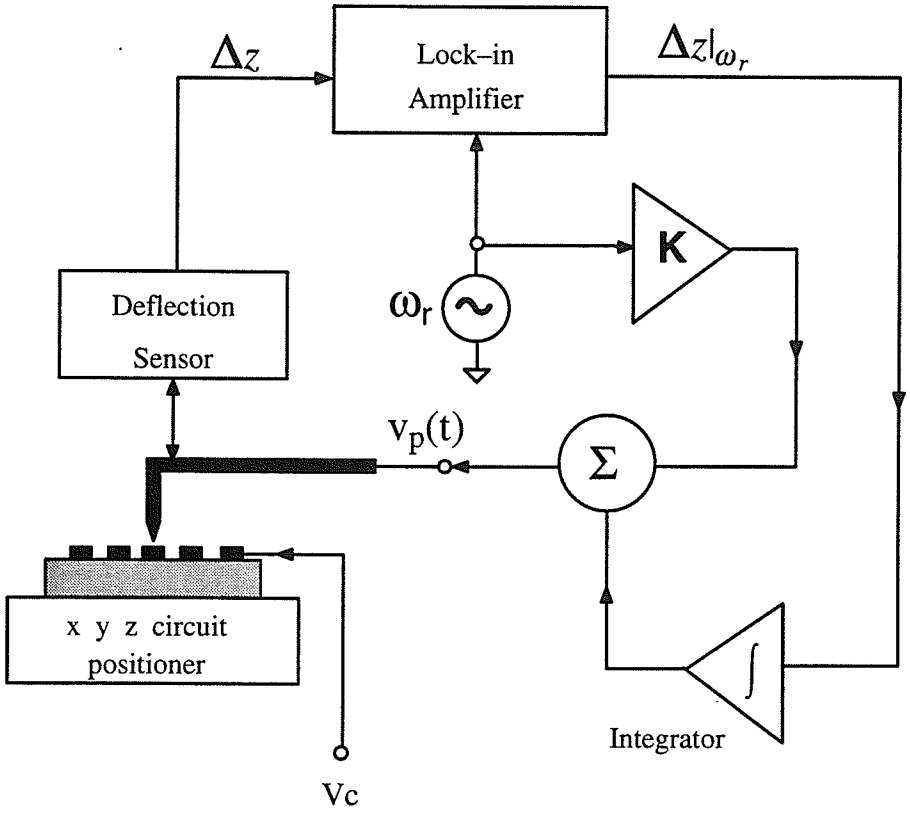

Fig. 3.10 Block diagram of the electrostatic force microscope instrument to extract DC potentials

oscillator and for driving frequencies near resonance, the deflection will be enhanced by the factor Q. To determine the magnitude of probe deflection at the probe resonant frequency ω_r, the electrostatic force component at ω_r in (3.14) then yields a deflection

$$\Delta z|_{\omega_r} = \frac{\partial C}{\partial z}\frac{Q}{k}\Big[A - \big(V_c(x,y) - \Delta\Phi\big)\Big]K\cos(\omega_r t) \qquad (3.15)$$

where the deflection magnitude at the resonance ω_r only has been considered. The driving frequency ω_r being the resonant frequency of the probe, the signal–to–noise ratio of the instrument is greatly enhanced because of the large Q of the cantilever.

In the nulling technique, the DC potential at a point on the circuit is determined by varying the DC bias A applied to the probe tip until the AC vibration amplitude of the tip at ω_r, as measured by the deflection sensor is minimized. The nulling technique allows potential measurements without explicitly determining the constant $\partial C/\partial z$ and thus avoids complex calibrations.

Fig. 3.10 shows a block diagram of the set–up used to perform DC potential measurements. The wire probe is positioned on the point on the circuit where the local DC potential is to be measured. The test circuit can be raster scanned in the x–y dimension using a computer controlled 2–axis positioner. The potential difference between the circuit and the probe causes a capacitively induced force resulting in a deflection Δz. The probe deflection is measured by a fiber interferometer and the deflection at ω_r is detected using a lock–in amplifier. The output from the lock–in amplifier will be proportional to the potential difference between the probe and the circuit. This signal is integrated, summed with the AC driving source and then applied to the probe. In a stable system, the DC component of the probe potential A will be adjusted by this feedback loop so that the output of the lock–in amplifier is minimized, hence reducing the probe vibration at ω_r to zero. Under this condition, the potential on the probe is equal to the local potential on the circuit ($A \approx V_c(x,y)$).

3.5.2 HF AC Measurement

To measure high frequency AC signals, heterodyne techniques based on frequency modulation [58] and an amplitude modulation [59] have been used. These methods enable the measurement of sinusoidal signals with frequencies much greater than the resonant frequency of the probe. They are based on using the square–law force interaction present between the EFM and the sample for mixing and sampling, where high speed signal under test is down converted to a much lower intermediate frequency. In our instrument, we are concerned with measuring sinusoidal signals on the circuit. An amplitude modulation scheme is used [60,61] which enables a nulling method to be used in conjunction with the heterodyne approach. This approach eliminates DC offset effects and the requirement for calibration. The signal $v_c(x,y,t)$ is assumed to be of the form

$$v_c(x, y, t) = V_c \sin(\omega_0 t + \phi_c) \tag{3.16}$$

where V_c is the unknown signal amplitude and ϕ_c is the unknown phase at the test point. The circuit under test is externally driven at the reference frequency ω_0 which is assumed to be much greater than ω_r. To implement the heterodyne technique, a signal at the reference frequency ω_0 is modulated and applied to the probe. Sinusoidal modulation and square wave modulation yield useful results for the extraction of AC signals and are described next.

3.5.2.1 Sinusoidal Modulation

In sinusoidal modulation, the signal applied to the probe is

$$v_p(t) = \left[A + K\cos(\omega_r t)\right]\sin(\omega_0 t + \phi_p) \tag{3.17}$$

Here A, K and ϕ_p are user controllable parameters in the instrument. Using (3.1), the force on the probe will be

$$F_z = \frac{1}{2}\frac{\partial C}{\partial z}\Big[\big(A + K\cos(\omega_r t)\big)\sin(\omega_0 t + \phi_p) - V_c \sin\big(\omega_0 t + \phi_c\big) + \Delta\Phi\Big]^2 \tag{3.18}$$

This square law mixing results in a static force component as well as components at frequencies ω_r, $2\omega_r$, ω_0, $2\omega_0$, $\omega_0 \pm \omega_r$, $2\omega_0 \pm \omega_r$ and $2\omega_0 \pm 2\omega_r$. The force component at ω_r is

$$F_z(\Delta v, z)|_{\omega_r} = \frac{1}{2}\frac{\partial C}{\partial z} K\Big[A - V_c\cos(\phi_p - \phi_c)\Big]\cos(\omega_r t) \tag{3.19}$$

By adjusting the probe voltage A and probe phase ϕ_p so that the beam deflection at ω_r is nulled, the circuit signal amplitude and phase (V_c, ϕ_c) can be extracted. As in the case of DC measurement, the probe deflection at the resonant frequency $\Delta z \approx QF_z/k$ is monitored with a lock–in amplifier. Again using a nulling method, the ill–conditioned factors C(x,y,z), Q and k are not required. Thus accurate probe positioning is not required and complex calibrations are avoided for accurate and repeatable measurements. The force term (3.19) does not contain the term $\Delta\Phi$ and thus the measurement is not sensitive to DC offset effects. For simplicity, this offset term

will not be included in the expression for the force. The modulation signal at the resonant frequency improves the signal–to–noise performance of the measurement as in the dc case.

3.5.2.2 Square Wave Modulation

The sinusoidal modulation may not be easy to implement using simple electronic circuitry, particularly at RF frequencies. Alternately, square wave modulation applied to the reference signal allows the heterodyne technique to be implemented in much the same way as in case of sinusoidal modulation described above [62]. This method has been used successfully to measure signals at 1 GHz as will be discussed in chapter 5.

In this case, a reference signal $\cos(\omega_0 t + \phi_p)$ is modulated by a square wave $G_T(t)$, at a frequency ω_r, and applied to the probe as

$$v_p\ (t)\ =\ \left[\ A + K\ G_T(t)\ \right]\ \cos\ \left(\omega_0 t + \phi_p\ \right) \tag{3.20}$$

Here A, K and ϕ_p are user controllable parameters in the instrument. Using (3.1) and representing $G_T(t)$ by its Fourier series, the force on the probe will be

$$F_z\ (z)\ =\ \frac{1}{2}\frac{\partial C}{\partial z}\ \left[\left(A + K\frac{4}{\pi}\sum_{\substack{n=1\\ n\ odd}}^{n=\infty}\frac{1}{n}\sin n\omega_r t\right)\cos(\omega_0 t + \phi_p) - V_c\cos(\omega_0 t + \phi_c)\right]^2 \tag{3.21}$$

which results in a static force component as well as components at frequencies ω_r, $n\omega_r$, ω_0, $2\omega_0$, $2\omega_0 \pm n\omega_r$. The probe deflection at ω_r is

$$\Delta z\ \Big|_{\omega_r}\ =\ \frac{1}{2}\frac{Q}{k}\frac{\partial C}{\partial z}\ K\frac{4}{\pi}\ \left[A - V_c\ \cos\left(\phi_p\ -\ \phi_c\ \right)\right]\ \sin\ \left(\omega_r t\right) \tag{3.22}$$

This yields a result similar to the one in case of sinusoidal modulation (3.19) except for an additional $4/\pi$ factor. Again the probe voltage A and probe phase ϕ_p is adjusted so that the beam deflection at ω_r is nulled. Thus the circuit signal amplitude and phase (V_c, ϕ_c) can be extracted.

CHAPTER 4

High Frequency Measurements

In this chapter, results demonstrating non–contact heterodyne electrostatic force measurements performed using square–wave modulation at 10 MHz are presented. Measurements using sinusoidal modulation and at lower frequencies have been performed earlier and are reported [60,61]. The measurements presented here demonstrate that the heterodyne technique works with the square–wave modulation. The establishment of these results is important since the RF measurements presented in the next chapter rely on the square–wave modulation method. Further, the need and methodology for probe calibration is discussed and is crucial at higher frequencies. The experimental set–up is described briefly followed by some measurement results.

4.1 Measurement System

In the experiment, a sinusoidal signal with an adjustable amplitude and phase is applied to a CMOS test circuit. This situation would typically be encountered in linear circuit applications where the circuit signal $v_c(t)$ is at the stimulus frequency ω_0 but undergoes changes in amplitude and phase as it propagates through various devices and interconnects on the circuit. Different nodes would then have varying amplitude and phase, but all at the same frequency ω_0.

The test set–up is shown in Fig. 4.1. The test structure used to demonstrate the system was a bond pad of a 68–pin PGA CMOS IC. This enabled a known voltage

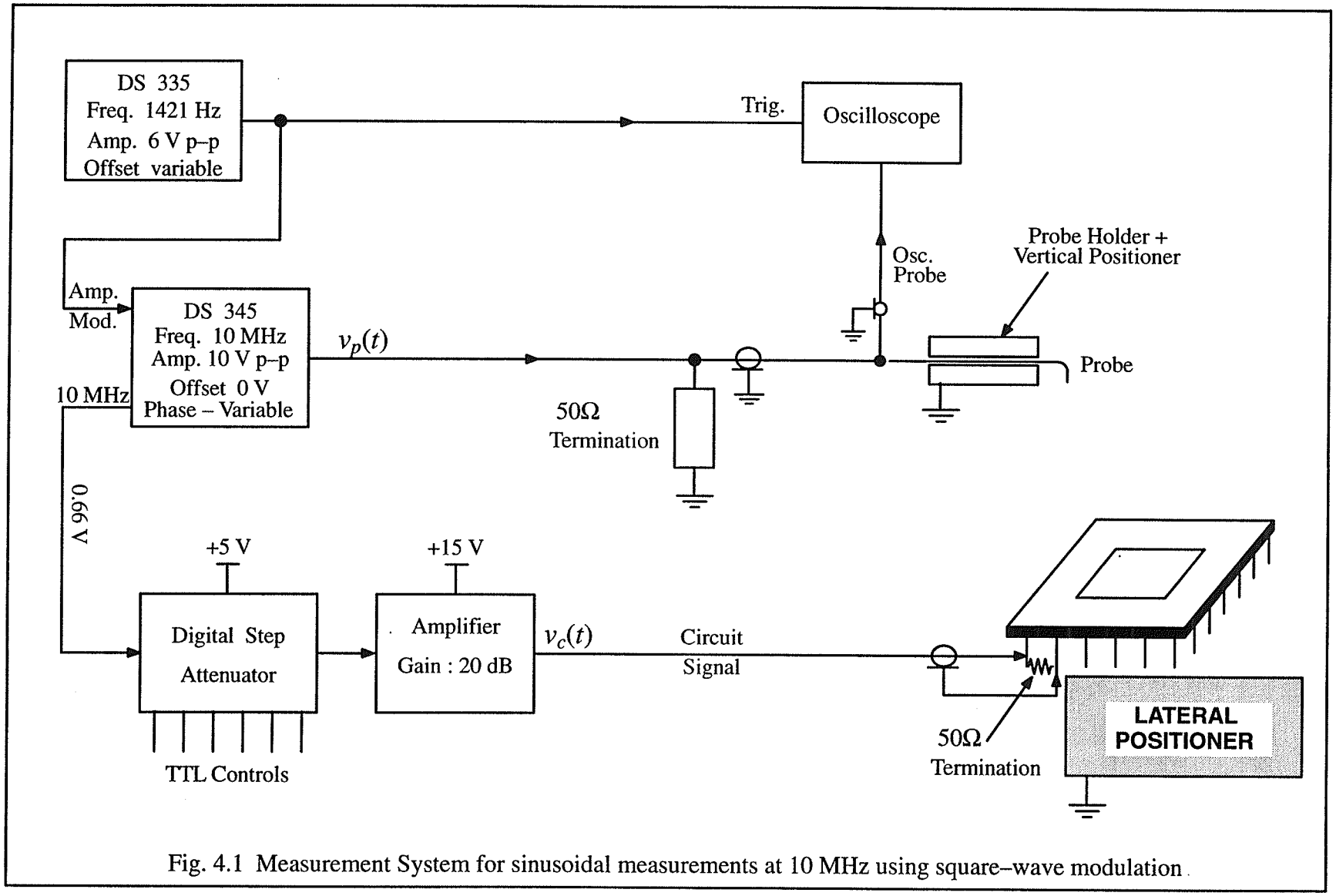

Fig. 4.1 Measurement System for sinusoidal measurements at 10 MHz using square–wave modulation.

to be applied to the test point. A molybdenum wire probe with dimensions similar to those discussed in chapter 3 was used. The end of the wire probe was electrochemically etched [63] to form a sharp tip. The tip was positioned approx. 1 μm above the bond pad. The resonant frequency of the probe was determined to be $f_r \sim 1421$ Hz and the quality factor $Q \sim 282$.

The test circuit is mounted on a 2–axis positioner. The structure holding the positioner, the wire probe and the fiber–optic interferometer is constructed from 3/4 inch aluminium plates to eliminate low frequency vibrations. All the major components of the measurement system are normally placed on a vibration isolation table. The fiber is positioned on the wire probe using a system of fine pitched screws and micrometers. The movement in the z–direction is controlled manually with an arrangement of screws and micrometer in a tripod arrangement allowing movements with an accuracy of 0.2 μm. To position the circuit within 1 μm of the wire probe, the table with the test circuit mounted on it is first moved up with the fine micrometer till the probe tip just starts touching the circuit. This is detected by a disturbance in the fiber signal. Then the table is lowered by turning the micrometer in the reverse direction. By calibrating the micrometer movement, the z–position of the probe above the circuit can be set to approximately 1 μm.

As shown in Fig. 4.1, the function generator has a 10 MHz reference on its back panel. This signal has a fixed amplitude (0.66 volts). To measure various levels of circuit signal V_c, a step attenuator and an amplifier are added before the circuit signal is applied to the pin of the CMOS IC. The circuit signal amplitude can be varied by changing the attenuation level of the step attenuator. A 50Ω chip resistor is mounted between the signal pin of the IC and ground to terminate the circuit signal in its characteristic impedance.

A second square wave signal generator (DS335) with variable offset is used to modulate the 10 MHz signal from the first function generator. A 50Ω termination is used to provide a match for the 50Ω source impedance of the function generator. The phase of the probe signal can be varied (with respect to the circuit signal) on the first function generator (DS 345).

4.2 Measurement Results

When a sinusoidal signal $v_c(x,y) = V_c cos(\omega_0 t + \phi_c)$ is applied to the circuit and a square–wave modulated signal is applied to the probe as $v_p = [A + KG_T(t)]\ cos(\omega_0 t + \phi_p)$,

the probe deflection magnitude at frequency ω_r has been shown in (3.21) to be

$$|\Delta z|_{\omega_r} = \frac{1}{2}\frac{Q}{k}\frac{\partial C}{\partial z}\,K\frac{4}{\pi}\left[A - V_c\cos\left(\phi_p - \phi_c\right)\right] \quad . \tag{4.1}$$

When $\phi_p=\phi_c$, the unknown amplitude can be determined as $V_c \approx A$ by nulling the deflection at ω_r. However, to set the phase accurately, the deflection has to be nulled with $A = V_c$. This is a dual optimization problem where one of the unknown parameters is required to be set accurately, before the other can be measured properly. An algorithm has been devised to initially determine the phase very accurately. Once this is done, the amplitude can be determined. The scheme is illustrated in Fig. 4.2 , where the

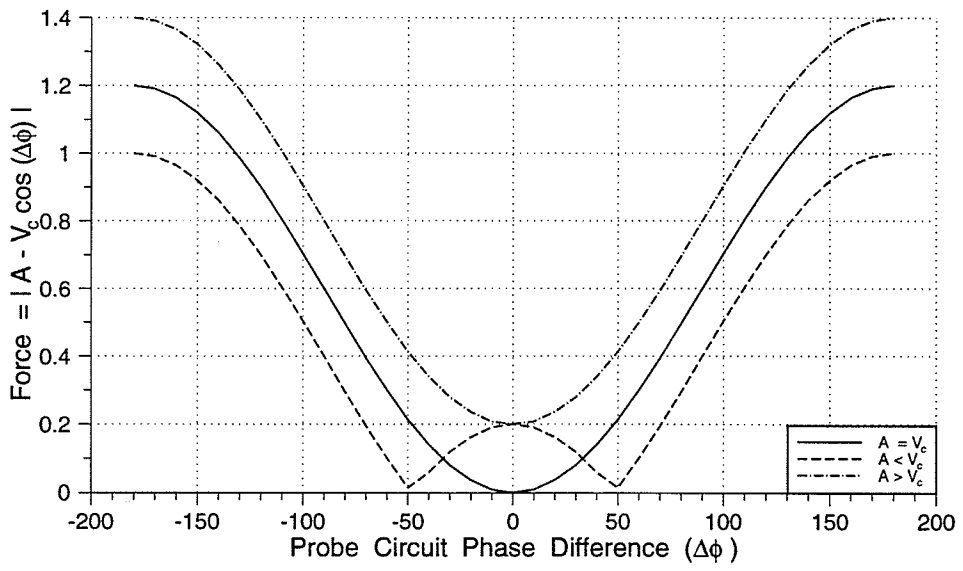

Fig. 4.2 Force/Deflection as a function of probe–circuit phase difference for (i) $A < V_c$ (ii) $A = V_c$ and (iii) $A > V_c$.

Force ($\propto \Delta z$) is shown as a function of the probe–circuit phase difference $\Delta\phi$ ($=\phi_p-\phi_c$) over 360^0. With $A > V_c$, the deflection is never nulled. With $A=V_c$, the deflection is nulled exactly at one point ($\Delta\phi = 0^0$). This null point is difficult to establish, specifically because the unknown amplitude V_c is not known apriori and also because the cosine

curve is flat near the null point. With $A < V_c$, the deflection is nulled at two distinct points.

In the experiment, to set the phase accurately, A is chosen to be lower than V_c. This is relatively easier than setting $A=V_c$. The phase ϕ_p is then varied to null the deflection at ω_r as detected by the deflection sensor. Two phase positions ϕ_{p1} and ϕ_{p2} are determined where the deflection is nulled, taking care that the two are less than 180^0 apart. The phase ϕ_p is set at the mean point $[(\phi_{p1} + \phi_{p2})/2]$ of these phases.

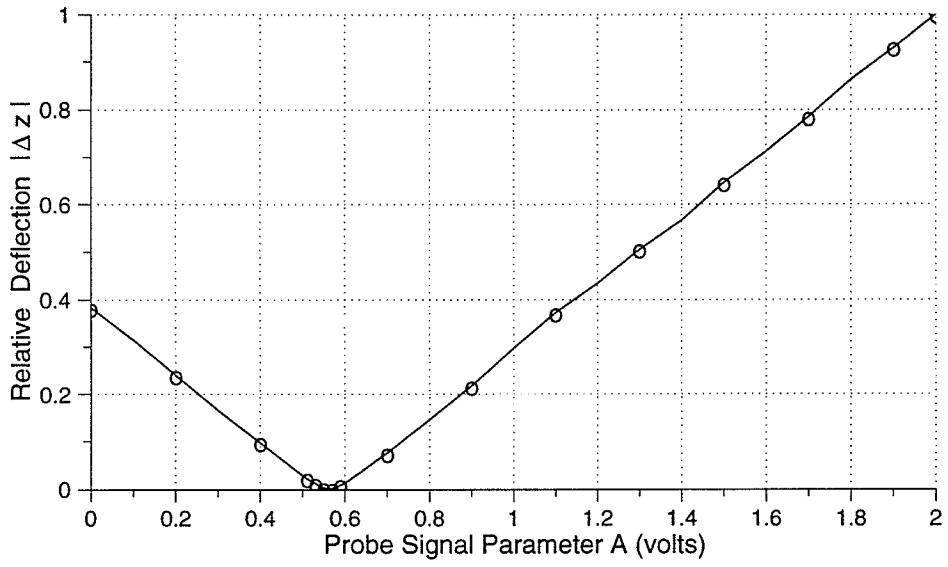

Fig. 4.3 Relative deflection signal as a function of the probe signal parameter A for test circuit amplitude V_c=0.63 V.

Once the phase is set accurately, the probe parameter A is varied until the deflection is nulled again. For test voltage magnitude V_c= 0.63 volts, Fig. 4.3 shows the measured probe deflection magnitude $|\Delta z|$ as a function of the probe parameter A. Here the probe phase has been adjusted to be equal to the circuit phase at the test point ($\phi_p=\phi_c$) using the procedure described above. The deflection is minimized when $A \approx V_c$. Similar plots for V_c=1.05 and 1.44 V are shown in Fig. 4.4 and Fig. 4.5 respectively.

To demonstrate the capability of measuring the phase at the test point, a voltage V_c=1.05 V was applied to the test point and the probe parameter A was set to minimize the deflection as shown in Fig. 4.4. The relative deflection as a function of probe

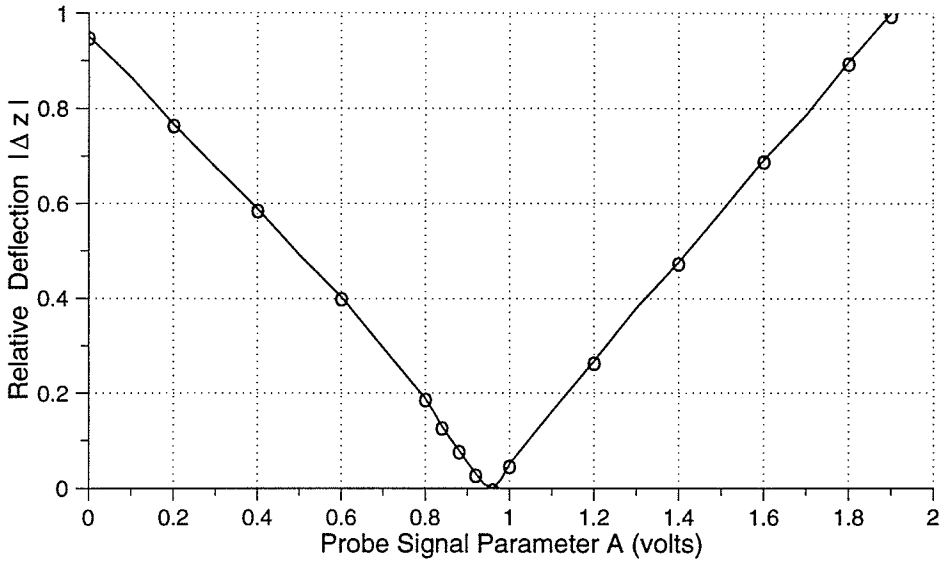

Fig. 4.4 Relative deflection signal as a function of the probe signal parameter A for test circuit amplitude V_c=1.05 V.

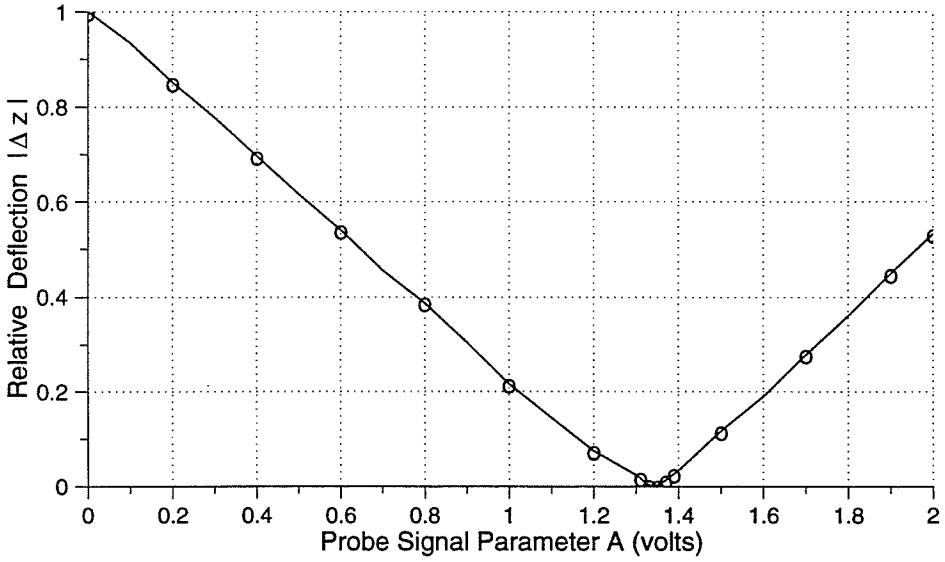

Fig. 4.5 Relative deflection signal as a function of the probe signal parameter A for test circuit amplitude V_c=1.44 V.

phase is shown in Fig. 4.6. The measured result matches well with the theoretical (1–cos $\Delta\phi$) response. This also indicates that the initial phase was set accurately employing the procedure described earlier.

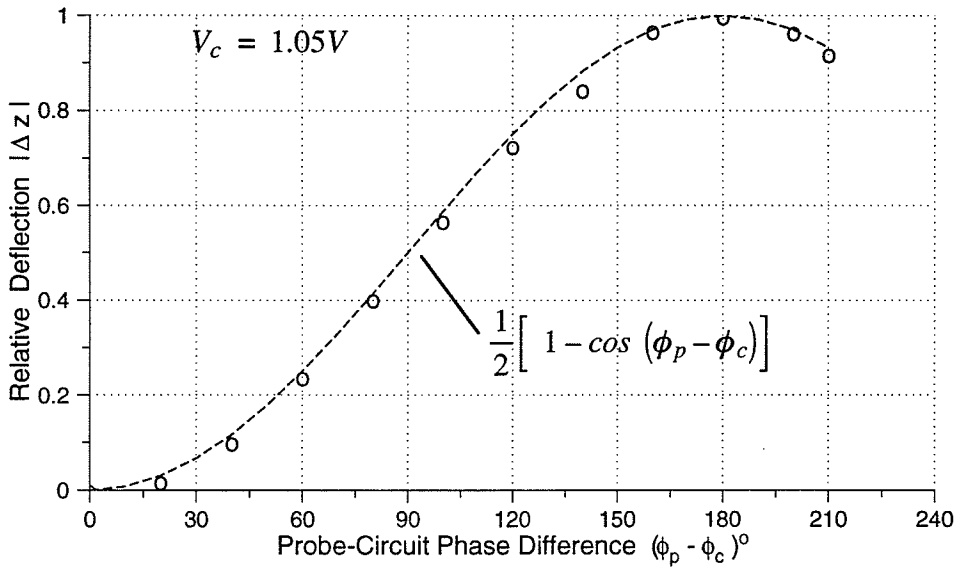

Fig. 4.6 Relative deflection signal as a function of phase difference ($\phi_p - \phi_c$) with fixed voltage levels V_c=1.05 V.

Next, measurements were performed for a number of circuit signal amplitudes V_c, and in each case the probe parameter A which nulls the deflection was determined. A plot of probe parameter A as a function of the circuit signal amplitude V_c is shown in Fig. 4.7. Linear variation of probe signal parameter A with circuit signal amplitude V_c suggests that a scaling factor is involved. This is a consequence of probe mismatch as these issues become significant at higher frequencies. This is discussed in more details in the next chapter where we perform GHz measurements.

The measurements presented in this chapter indicate that the square–wave modulation works as well as the sinusoidal modulation. Results indicate that the probe can be calibrated to account for the probe mismatch and thus provides the ability to measure signals accurately at high frequencies.

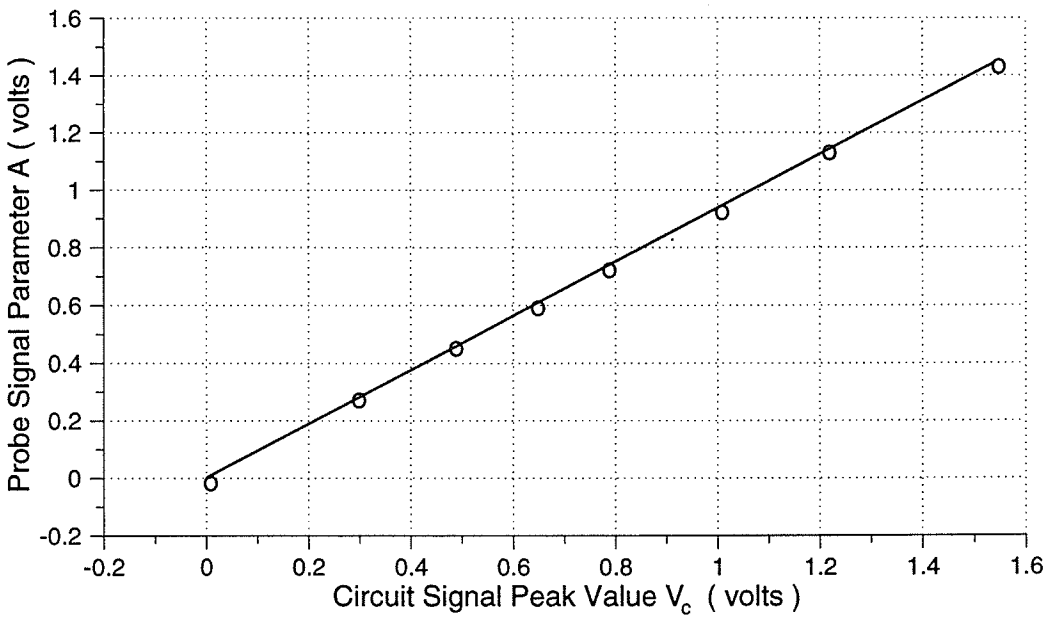

Fig. 4.7 Parameter A as a function of circuit signal amplitude V_c when Δz is nulled. $\phi_p = \phi_c$ and $f_0 = 10$ MHz.

CHAPTER 5

RF Measurements

The measurements presented in the previous chapter demonstrated the applicability of the developed square wave modulation approach for sinusoidal measurements using the heterodyne EFM technique. This chapter extends the measurements to RF frequencies. At higher frequencies, probe matching becomes critical as the path lengths approach the wavelength of the transmitted signal. The issues specifically relevant to high frequency measurements are discussed in this chapter. The signal electronics developed for applying the appropriate square–wave modulated probe signal is described next. Results of measurements performed on a microstrip thru–line and a commercial Texas Instruments MMIC amplifier are presented.

5.1 Introduction

As mentioned earlier, the main objective of this thesis is to demonstrate measurements of high frequency signals with the scanning electrostatic force microscope. The push towards high frequencies in microelectronics/VLSI has already resulted in devices operating beyond 1 GHz. The potential benefit of extending the measurement capabilities of our instrument to GHz frequencies is that not only can the signals be measured on these integrated circuits, but also the waveforms on internal nodes of MICs and MMICs operating in the lower L bands can be measured as well. Personal communication systems, cellular phones and other RF technologies are being commercialized

and require the fabrication of miniature MMIC and hybrid MMIC components. The technique we present could be an important diagnostic tool in the testing and manufacturing of these devices.

5.2 Probe HF issues

In the electrostatic force microscope, the voltage on the circuit is measured by applying a controllable voltage to the probe which is typically positioned less than 1 μm over the circuit test point. At DC and low frequencies (few kHz), the signal that is applied to the probe can be assumed to be the signal at the probe tip. This assumption is not valid at higher frequencies, and at 1 GHz (λ = 30cm), a small length of wire can result in a large phase change and mismatch. Some of the high frequency issues which are critical in the proper functioning of the instrument are discussed in this section.

5.2.1 Electrical Equivalent Circuit

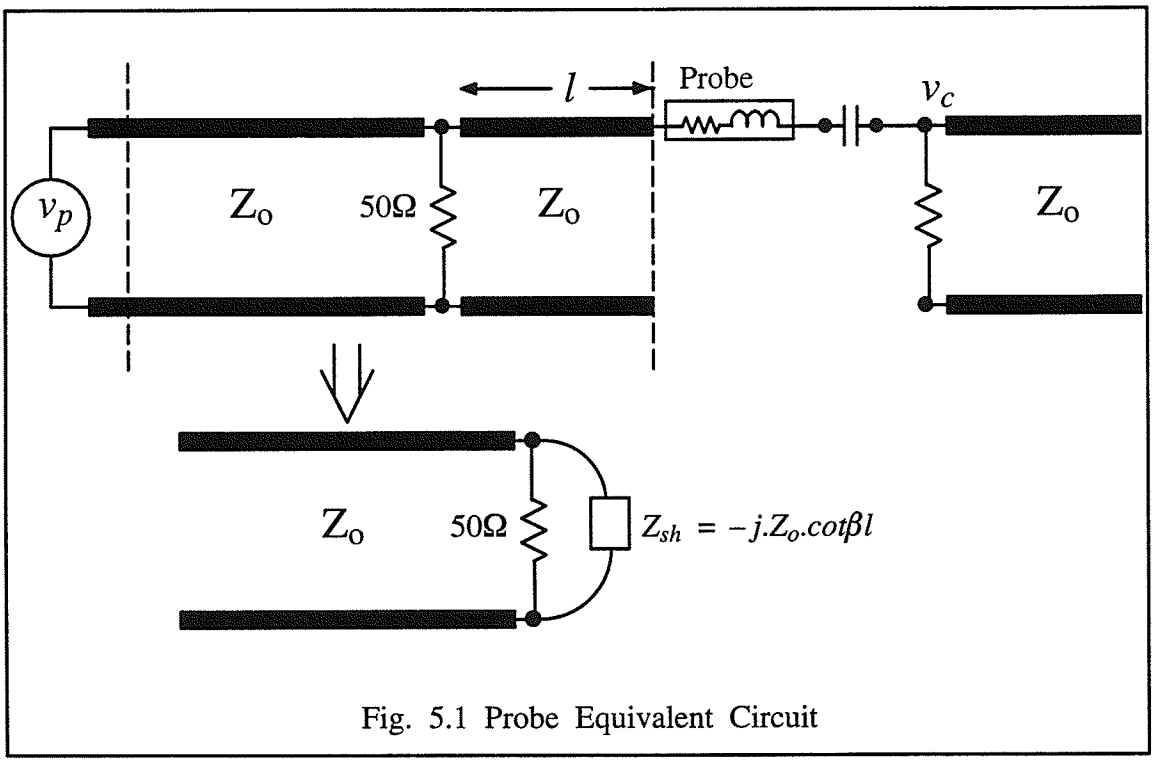

Fig. 5.1 Probe Equivalent Circuit

A semi–rigid cable (0.185 inch diameter) with a SMA connector at one end and the molybdenum wire attached to the centre conductor at the other end was used

for the probe in the measurement instrument. An electrical equivalent circuit of the probe–circuit interaction is shown in Fig. 5.1 where the semi–rigid cable is modelled as a transmission line. A lumped RLC model is used for the wire probe.

The capacitance between the probe and the circuit has been calculated numerically and is on the order of 0.2 fF [18]. The impedance, even at 1 GHz, is on the order of a few hundred KΩ and thus can be considered as an open circuit. The probe equivalent circuit is then essentially an open–circuited line of length 'l' at the end of a terminated 50Ω transmission line. To get a good match, characterized by a low return loss, the length of the open–circuit length is critical. The open–circuit length is equivalent to a shunt impedance which can be calculated using transmission line theory [64]. The equivalent shunt impedance is given by

$$Z_{sh} = -jZ_0 \cot \beta l \tag{5.1}$$

$$\text{where} \quad \beta = \frac{2\pi}{\lambda}$$

If we approximate the 50Ω termination to be the same as the characteristic impedance of the transmission line, and ignoring any parasitics, the return loss can be calculated as

$$s_{11}(Return\ Loss) = 20 \log |\Gamma| \tag{5.2}$$

$$\Gamma = \frac{-1}{1 + 2\ z_{sh}}$$

where z_{sh} = Normalized shunt impedance $= -j\ \cot \beta l$ and

$$\Gamma = \frac{-1}{1 - 2\ j \cot \beta l}$$

$$|\Gamma| = \frac{1}{\sqrt{1 + 4\ \cot^2 \beta l}} = \frac{1}{\sqrt{1 + 4\ \cot^2 \frac{2\pi l}{\lambda}}} \quad . \tag{5.3}$$

Using (5.3), the return loss has been simulated for various open–circuit lengths '*l*' over the frequency range from 50 MHz to 1.2 GHz. This is shown in Fig. 5.2. Fig. 5.3 shows a similar result achieved by simulation using PUFF, a PC based CAD software for microwave integrated circuit design [65].

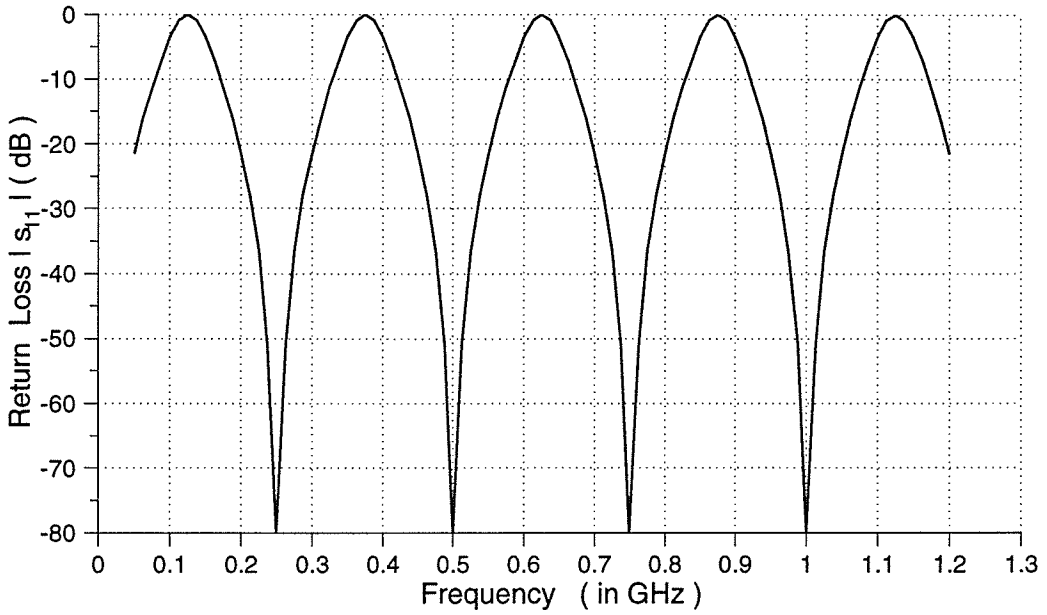

Fig. 5.2 Probe s_{11} simulated using equivalent circuit

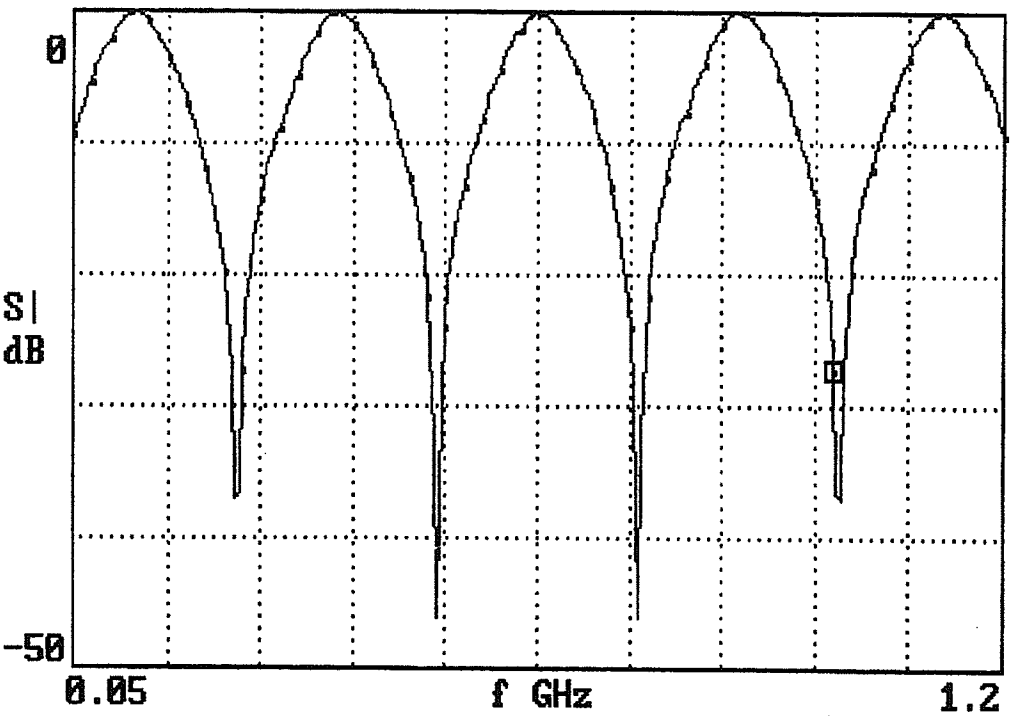

Fig. 5.3 Probe s_{11} plot using PUFF [65]

It can be seen from Fig. 5.2 that stub lengths in multiples of 15 cm give a good match (low return loss) at 1 GHz. This is because a half wavelength at 1 GHz = 15 cm.

5.2.2 Probe Matching

While it is desirable to have a good match for the probe over a wide frequency range, we found that it was one of the most difficult problems that was encountered in the development of our instrument.

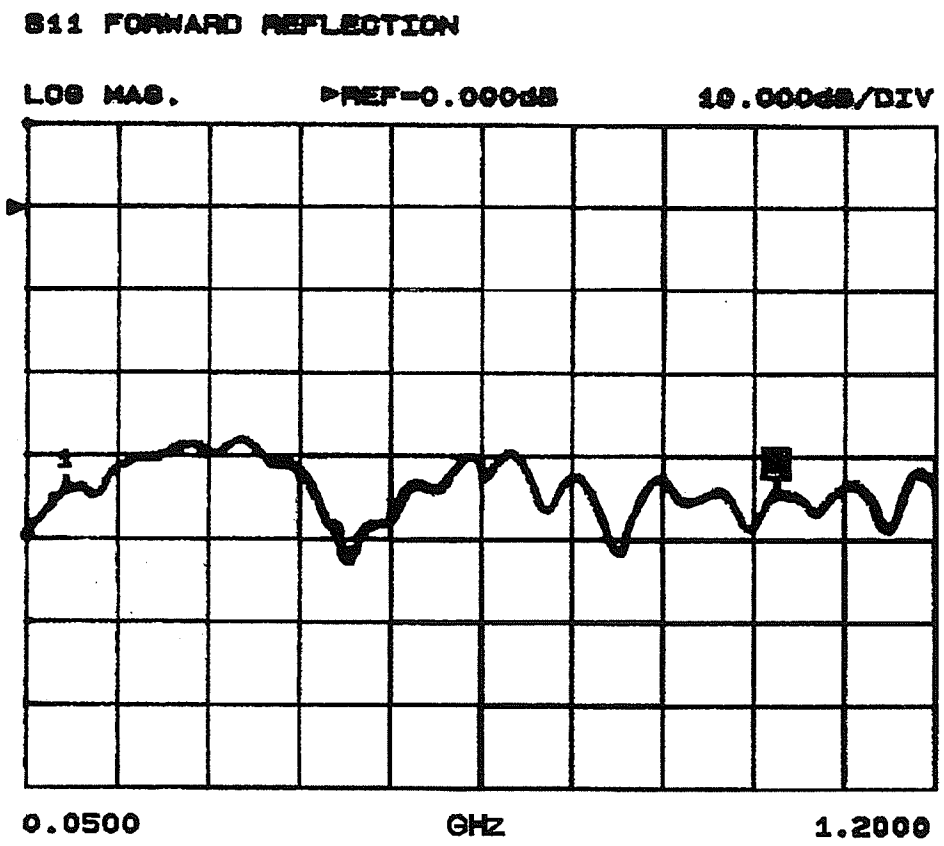

Fig. 5.4 Wideband probe match as measured on the network analyzer

At a first glance, it seems that terminating the probe with its characteristic impedance (50Ω) near the end (close to the Mo wire) should give a good wideband match. This arrangement was tested by soldering a 50Ω chip resistor between the centre conductor of the semi–rigid cable and its outer conductor near the small wire probe. A small

cavity was carved out of the cable by cutting through the dielectric to the centre conductor. This arrangement indeed gave a very good match as measurement on a network analyzer (Fig. 5.4) indicates. However, the voltage applied to the probe produced a sufficient heating of the centre conductor and the Mo wire close to the end, that the force induced vibration could not be nulled. Even the use of four 200Ω chip resistors, all soldered between the inner conductor and the outer copper shield of the cable resulted in enough heating to prevent nulling due to residual thermal drift of the probe.

Since terminating the probe near its end is difficult to realize, a 50Ω feedthrough termination, far from the probe, was used. The available termination with BNC connectors had to be connected to the semi–rigid cable by a series of coaxial adaptors. To eliminate mechanical vibration of the system, the bulky adaptors and the feedthrough

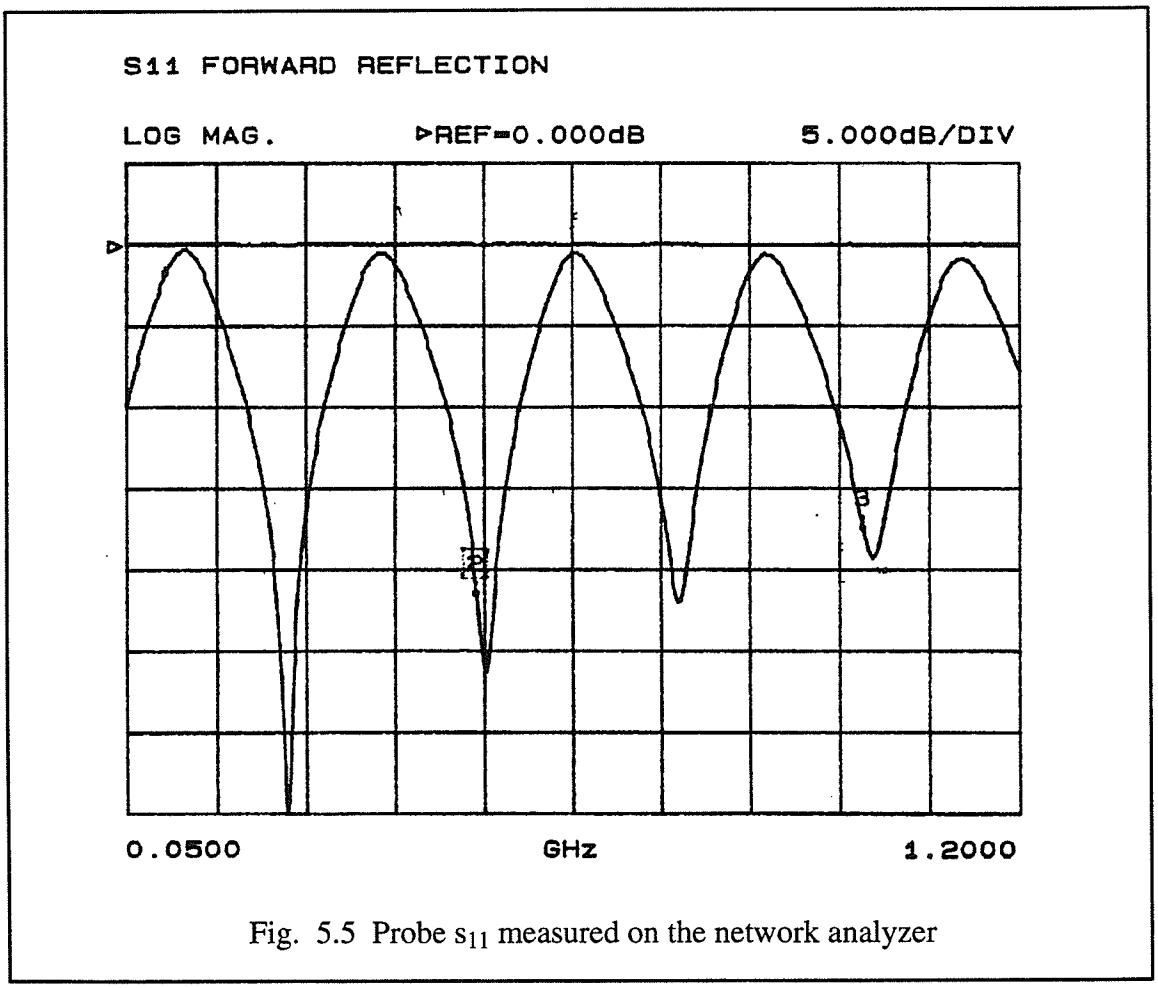

Fig. 5.5 Probe s_{11} measured on the network analyzer

termination were placed some distance away from the probe holder and the platform on which the circuit was mounted. This arrangement necessitated a long length of open–circuit line. The result was a fairly narrowband match around the frequency of measurement. It may be noted that a return loss of –18 dB (VSWR = 1.3) is considered a good match and also desirable for the safety of microwave components used to feed the probe signal. The return loss of the actual probe arrangement used in the measurement system was measured on the network analyzer and is shown in Fig. 5.5. Low return loss (–18 dB) at a desired frequency was achieved by adjusting the length of the open circuit line.

Since the modulating frequency is typically quite low (few kHz), the signal applied to the probe is a narrowband signal at GHz frequencies (< 1 MHz bandwidth). Thus if the probe is matched at 1 GHz, it can be considered a good match over the band of frequencies that are being fed to the probe.

5.3 Measurement System

While the square–wave modulation scheme used in the measurements may be simpler to realize with some of the commercially available instruments, the cost of these microwave instruments can be prohibitively expensive. Our measurement instrument was realized using some simple, inexpensive microwave components and devices.

A block diagram of the measurement system is shown in Fig. 5.6. The high frequency signal source is a HP 8350 sweep oscillator operated at the CW frequency at which measurement are to be performed. To apply the signal to the DUT, and simultaneously derive a reference signal to be applied to the probe, a power divider was used. A set of three phase shifters connected in series were used to provide controllable phase change in the probe signal and to set the phase for nulling the force/deflection. The digital step attenuator (DSA) is the next component in the chain. In this component, each attenuation step is switched on or off by a TTL signal, with the difference in insertion loss between the on and off states being the step attenuation. The biphase modulator is used to provide a 0^0 or 180^0 fixed phase shift. The step attenuator, the biphase modulator, and the associated control logic are used to implement square wave modulation of the reference frequency signal from the power divider. Finally, an amplifier is used to increase the level of the signal since the signal goes through

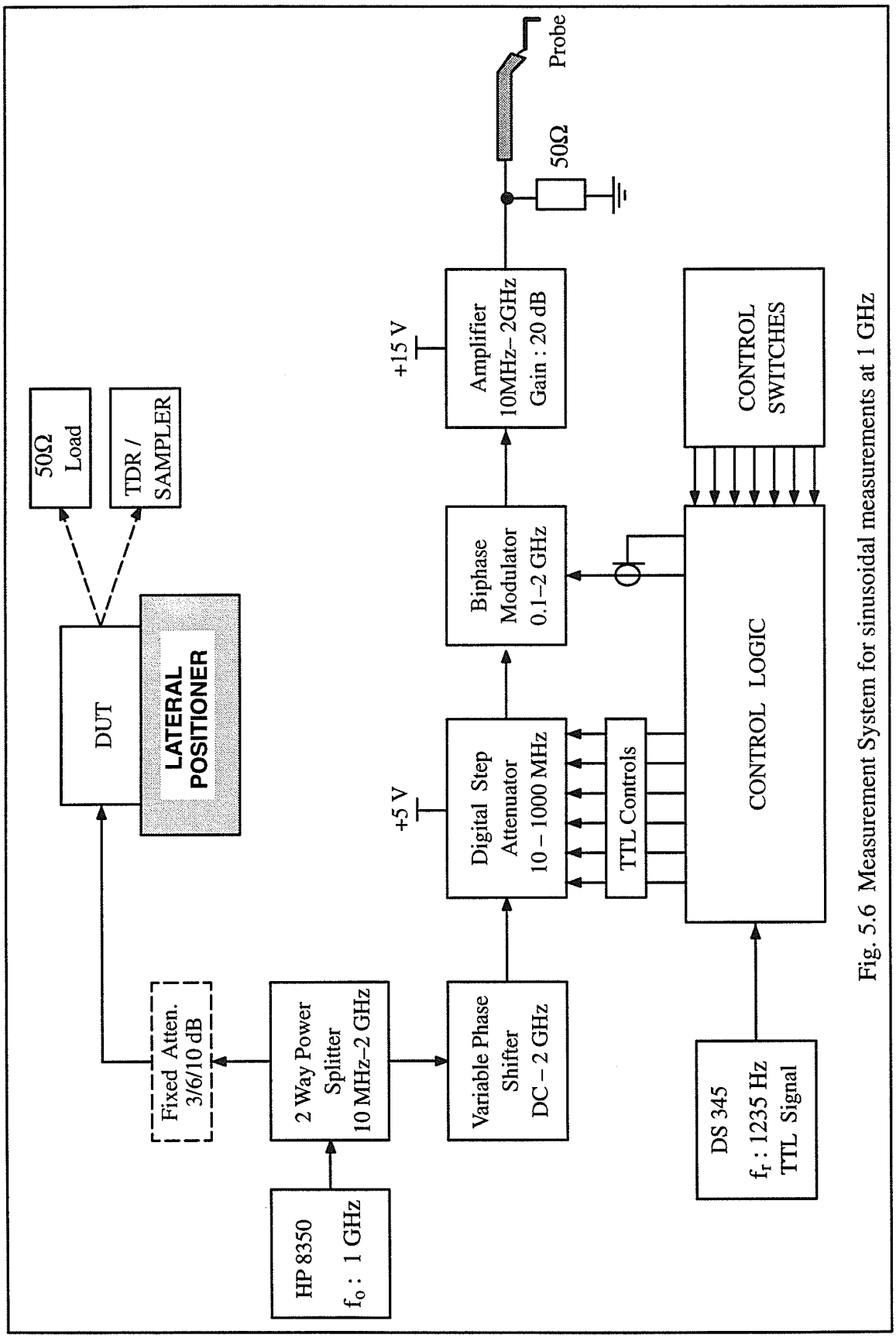

Fig. 5.6 Measurement System for sinusoidal measurements at 1 GHz

a series of components that have a fairly large insertion loss. The output from the amplifier is fed directly to the probe through a series of flexible cables, 50Ω feedthrough terminations and adaptors as described in the previous section.

With reference to Fig. 5.6, the other output of the power divider feeds the signal to the device on which the test point is located. Depending on the signal level requirements, varying attenuation levels can be introduced using fixed attenuators as shown within dashed box in the figure. For example, if the signal to be measured is an amplifier, with a high gain and a limited output level, the input signal has to be low and appropriate attenuation is introduced. On the other hand, if the signal to be measured is on a thru–line for example, the attenuation can be reduced or even completely removed to provide a signal with a large amplitude on the thru–line.

The control logic consists mainly of TTL logic components and an opamp used to provide appropriate control signals to the digital step attenuator and the biphase modulator. A function generator (DS 345) which provides the modulating frequency at the resonant frequency of the probe completes the measurement system. Brief specifications of some of the key components used in the measurement system are listed in Table 5.1 [66].

Table 5.1 : Component Specifications

2 Way Power Divider	MC ZESC–2–11	Freq. 10–2000 MHz
Phase Shifters	Sage 6702	Freq. DC–2 GHz Nom. phase Shift : 5.7/GHz/Shaft–turn
Digital Step Attenuator	MC ZSAT–31R5	Freq. 10–1000 MHz ; TTL Controls Principal Atten. Steps : 0.5,1,2,4,8,16 dB
Electronic Attenuator / Biphase Modualtor	MC ZFAS–2000	Freq. 100–2000 MHz Biphase : + 20 mA
Medium Power Amplifier	MC ZFL–2000	Freq. 10–2000 MHz ; Gain 20 dB min. Max. Power Output : +16 dBm

Recalling from chapter 3, the voltage applied to the probe in square–wave modulation is of the form

$$v_p\ (t)\ = \left[\ A + K\ G_T(t)\ \right] \cos\ \left(\omega_0 t + \phi_p\ \right) \quad . \tag{5.4}$$

The implementation of square–wave modulation is illustrated in Fig. 5.7. In normal implementation, K is kept constant and the offset A is varied. When there is no attenuation on the DSA i.e. all the TTL controls are at logic zero level and the biphase modulator introduces no phase change (due to positive current applied at its control port), there is no modulation and the waveform applied to the probe is as shown in Fig. 5.7(a). Next, when a small attenuation step is applied to the DSA, the waveform changes to as shown in Fig. 5.7(b). The step applied to the DSA is a 1/2 cycle of the square–wave and the period corresponds to the resonant frequency of the probe.

$$T\ = \frac{1}{f_r} \tag{5.5}$$

Using 6 discrete steps, attenuation levels ranging from 0.5 dB to 31.5 dB in steps of 0.5 dB can be applied to the probe signal. Progressively increasing attenuation are illustrated in Fig. 5.7(c) and 5.7(d) respectively. With reference to (5.4), Fig. 5.7(a) would correspond to K=0. Similarly Fig. 5.7(b,c,d) correspond to increasing values of K and decreasing values of A so that (A+K) is a constant level depending on the input to the step attenuator. With large attenuation, the output approaches the waveform of Fig. 5.7(e) which corresponds to the case where A=K. In the actual circuit, however, this situation is never realized since there is a small signal even with the maximum attenuation (31.5 dB) so that A≈K. In all of the cases described above, there was no phase shift through the biphase modulator and the output from the DSA is just attenuated by the insertion loss of the modulator. When the control corresponding to the biphase modulator is turned 'ON', the waveform at the output is as illustrated in Fig. 5.7(f). Here a negative current is supplied to the modulator control causing it to introduce a phase shift of 180^0. Since the negative current is applied only in the half cycle in which attenuation is applied to the DSA, the other half cycle remains unaffected. Also, since the attenuation level for the electronic attenuator is same for negative current, the attenuation level remains the same as in Fig. 5.7(d). This corresponds to the situation where K>A. With biphase modulator turned 'ON', different

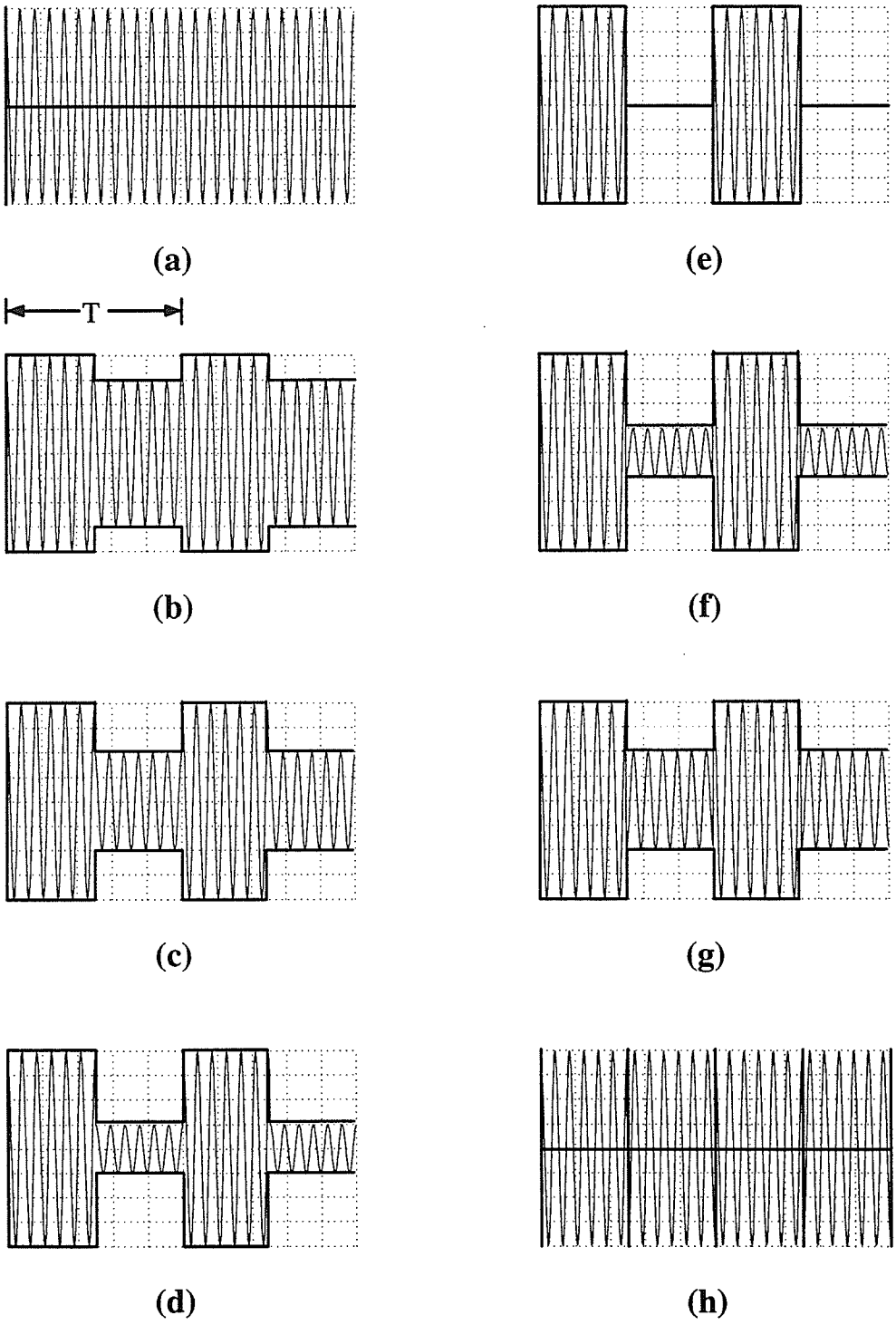

Fig. 5.7 Square Wave Modulation as realized in the system

attenuation levels will give another set of levels for A and K with K>A in each case. Finally, with no attenuation on the DSA, and with biphase modulator turned 'ON', the waveform as shown in Fig. 5.7(h) is obtained, which corresponds to A=0.

For any given attenuation level, the A and K values in (5.4) are determined as illustrated in Fig. 5.8. It is to be noted that since the attenuation and biphase modulator phase shift are applied in only one half cycle, V_{max} remains constant. Also, the maximum value of V_{min} is equal to V_{max}. Therefore, the probe parameter A would range from V_{max} when there is no attenuation and the biphase modulator is OFF to zero when there is no attenuation and the biphase modulator is ON. V_{max} is limited by the output of the amplifier. In the measurement system (Fig. 5.6), the input level of the HP source is adjusted so that the amplifier operates at the maximum allowable output power level (below 1 dB compression point). This signal is then applied to the probe.

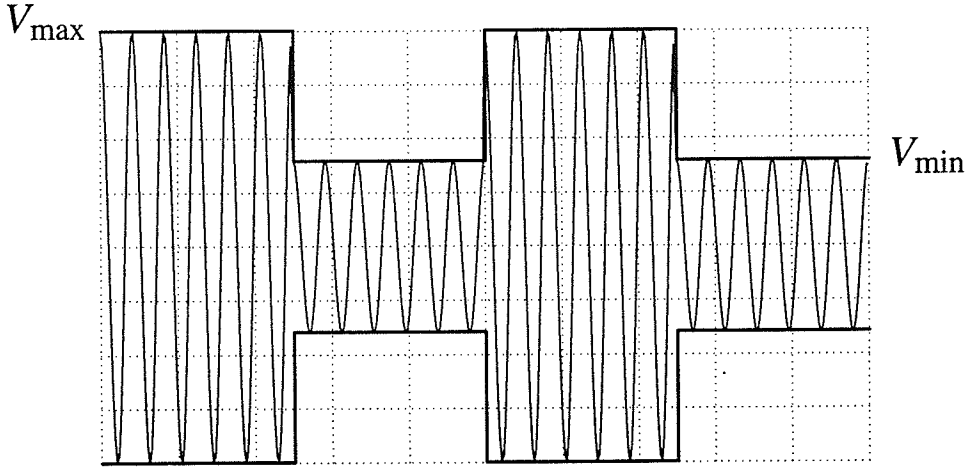

With Biphase Modulator 'OFF' : $A = \frac{V_{max} + V_{min}}{2}$ $K = \frac{V_{max} - V_{min}}{2}$

With Biphase Modulator 'ON' : $A = \frac{V_{max} - V_{min}}{2}$ $K = \frac{V_{max} + V_{min}}{2}$

Fig. 5.8 Determining A and K in the measurement system

To map the attenuator and biphase modulator control switch settings to the corresponding A and K levels in (5.4), the output of the amplifier was measured with a Tektronix TDR/Sampler. The measurement arrangement is shown in Fig. 5.9. The amplifier output is connected to an S–6 sampling head of a 7S12 TDR/Sampler through a 6 dB attenuator. The attenuator is added to avoid damage to the sampling head. A trigger is provided by a power splitter to the S–53 trigger recognizer. Signals up to 1 GHz can be measured using the S–53 trigger recognizer.

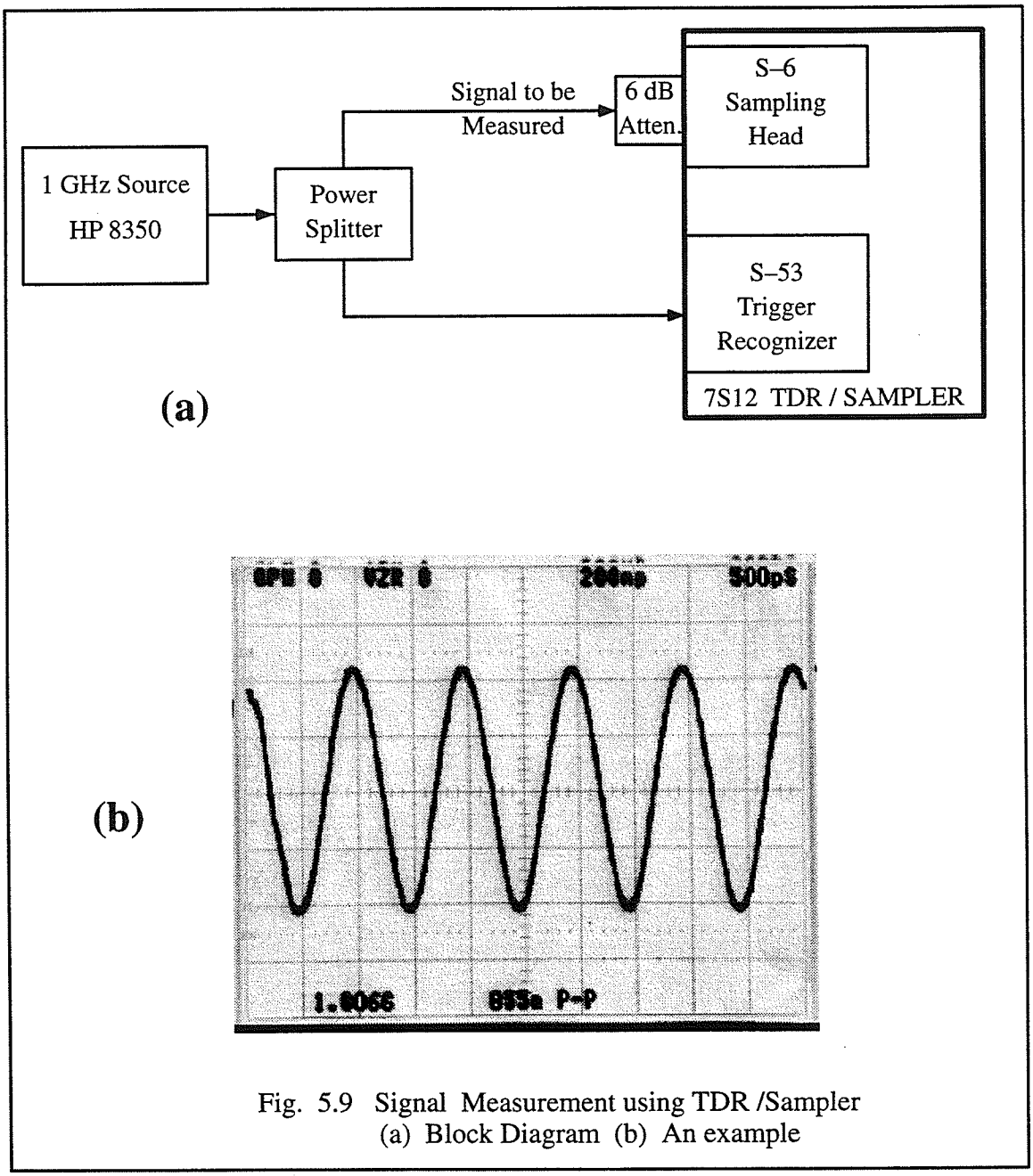

Fig. 5.9 Signal Measurement using TDR /Sampler
(a) Block Diagram (b) An example

Using the arrangement shown, V_{min} is measured for different attenuation levels. Since modulated signals cannot be measured using this arrangement, the modulation is turned off. V_{max} is measured with 0 dB attenuation. The signal on the sampler can be averaged and the peak–to–peak voltage is read off directly from the display as shown in Fig. 5.9(b). Since a 6 dB attenuator is used at the input, the voltage read on the sampler is approximately half of the input voltage level. Thus the peak–to–peak voltage is directly taken as the V_{min} level. Since all voltages are measured using the same attenuator, any inaccuracies that may be present in the measurement system are scaled out. From these measurements, a look–up table was prepared which gives A and K values for different control switch settings.

A photograph of the entire measurement system, including the signal electronics, is shown in Fig. 5.10. The box on the left is the fiber–optic displacement sensor. Its output is monitored on a FFT spectrum analyzer. Next to this is the probe–holder along with the 2–axis positioner on which the DUT is mounted. These are placed on a floating granite slab (mounted on inflated tubes).

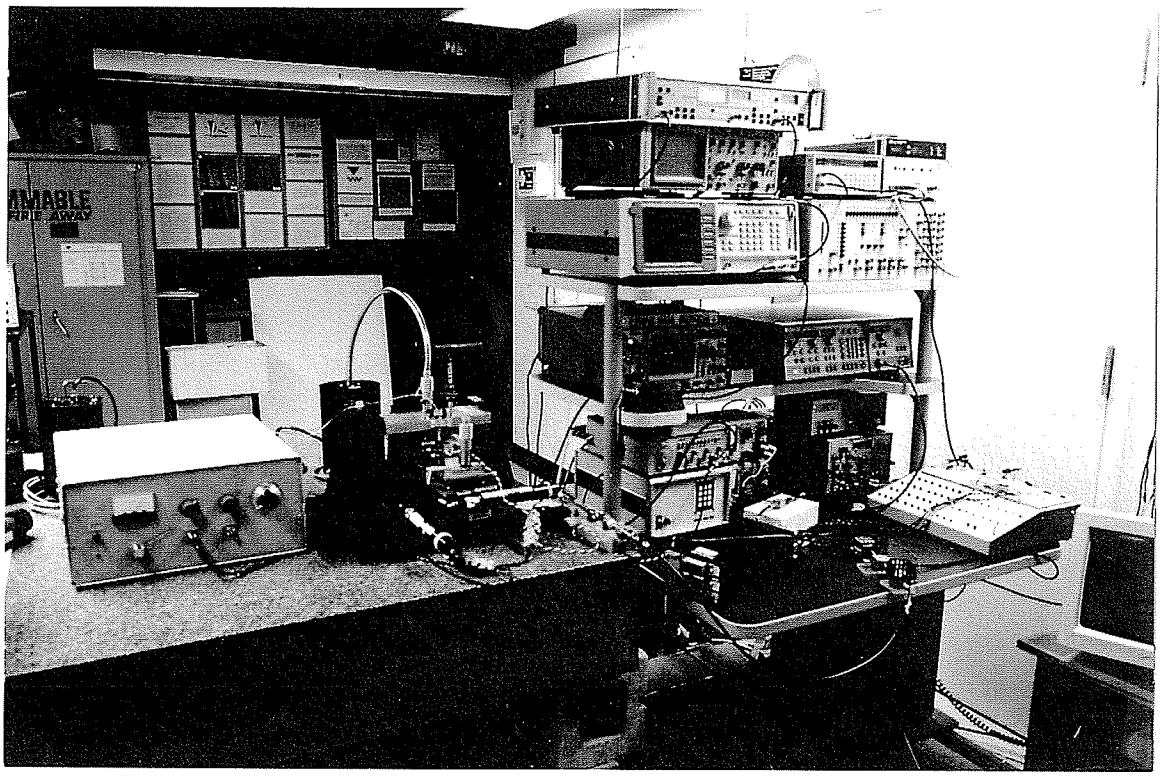

Fig. 5.10 Photograph of the Measurement System

5.4 Measurements on a Microstrip Thru–Line

Measurements were first performed on a microstrip thru–line. The microstrip was fabricated using copper tape on a microwave substrate (ε_r=2.5). The characteristic impedance of the microstrip line depends on the width, the dielectric constant of the substrate material, the thickness of the board and the thickness of the conductor. Standard synthesis equations were used to calculate the width of the tape for a 50 Ω transmission line [67]. With ε_r=2.5 and thickness of the board=1.5875 mm, the width of the transmission line for 50Ω impedance was calculated to be 4.46 mm. A copper tape of width w≈4.46 mm was cut and pasted on the substrate. SMA connectors were soldered at each of the two ends and the body of the connector was soldered to the back plane copper on the board. A photograph of the microstrip thru–line is shown in Fig. 5.11.

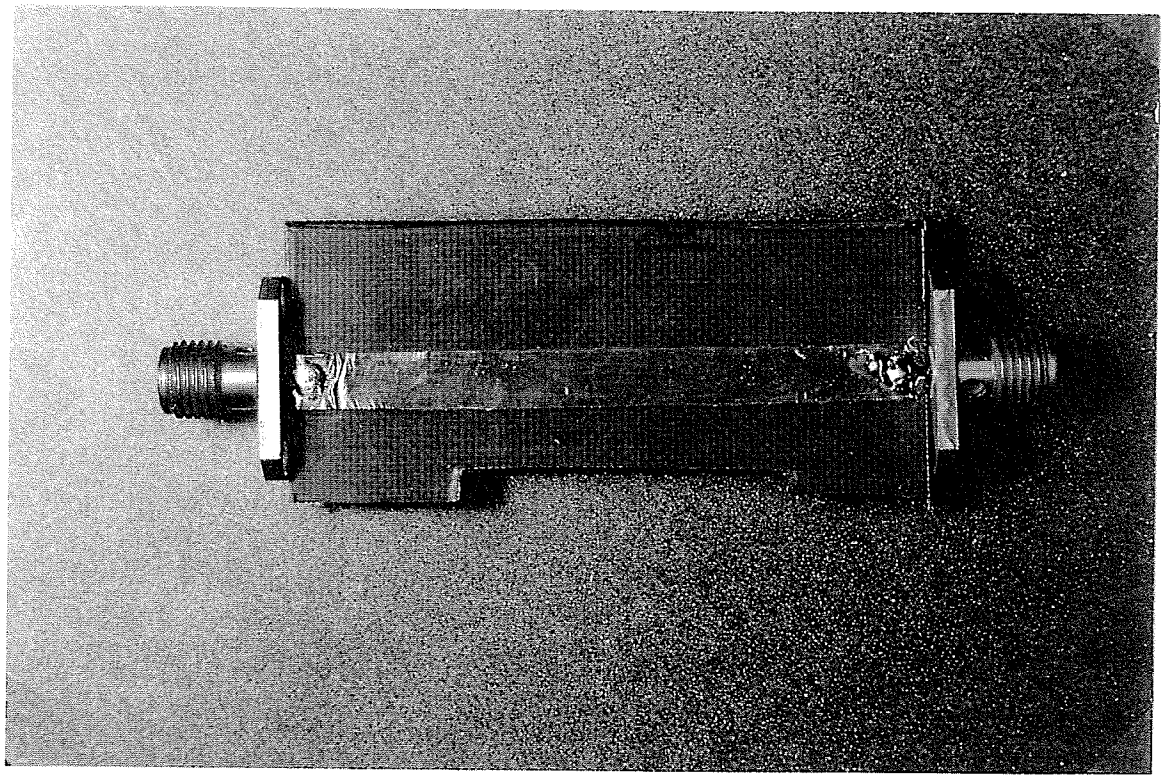

Fig. 5.11 Photograph of the Microstrip Thru–Line

Since the synthesis equations are empirical and the width of the tape is difficult to cut and maintain accurately, the S–parameters were measured on the network analyzer

after assembling the thru–line. The measured forward reflection parameter s11 is shown in Fig. 5.12. The return loss is better than 28 dB indicating a good match on the

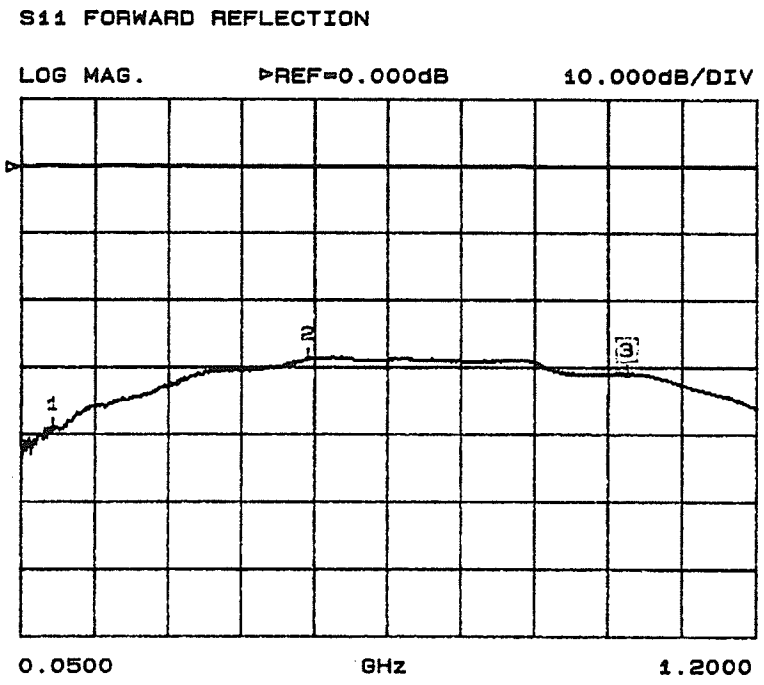

Fig. 5.12 s_{11} of the thru–line measured on the network analyzer

input port. For this measurement, the output port was terminated with a 50Ω load. Next the forward transmission parameter s21 was measured for the thru–line. The measured result is shown in Fig. 5.13. Transmission loss of less than 0.1 dB indicates that the losses on the microstrip are minimal. These measurements indicate that the characteristic impedance of the transmission line fabricated using the tape is close to 50Ω and that the voltages applied to the input of the structure should be maintained on the line.

Sinusoidal measurements at 1 GHz were performed next for different circuit signal amplitudes V_c. The circuit signal amplitudes were varied by changing the fixed attenuators shown in the measurement system (Fig. 5.6). The circuit signal amplitudes were measured on the TDR/sampler prior to performing the measurements with the instrument using the same 6 dB attenuator as mentioned earlier.

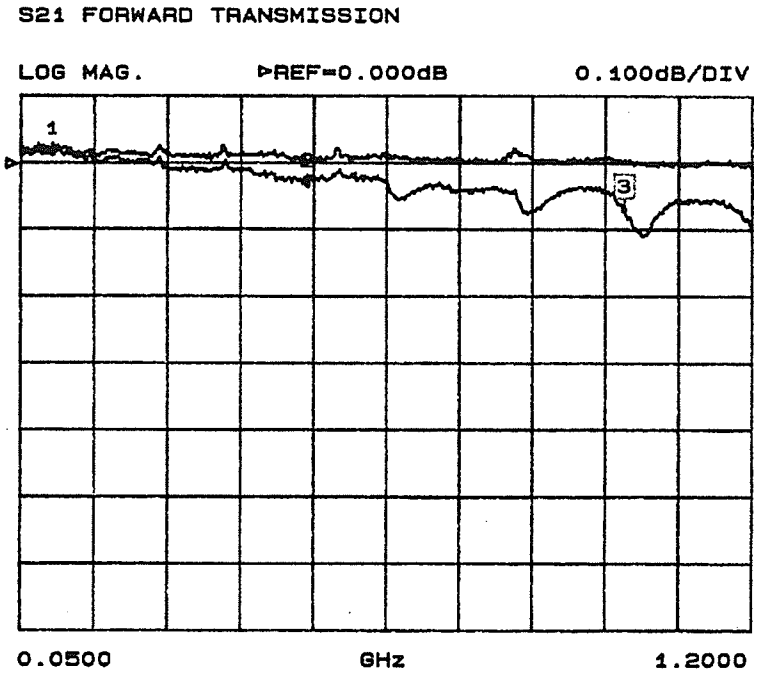

Fig. 5.13 s_{21} of the thru–line measured on the network analyzer

As developed in chapter 4, the probe deflection magnitude at the resonant frequency ω_r is given by

$$|\Delta z|_{\omega_r} = \frac{1}{2}\frac{Q}{k}\frac{\partial C}{\partial z}\, K\frac{4}{\pi}\left[A - V_c\cos\left(\phi_p - \phi_c\right)\right] \tag{5.6}$$

To establish the circuit signal amplitude V_c by nulling the deflection, the phase had to be set accurately first. This was done using the procedure described in chapter 4. With some low attenuation ($A < V_c$), the probe phase was changed using the mechanical phase shifters and two null points were obtained as before. Then the shaft position for the two nulls was averaged and the phase shifter shaft set at the mean position. If more than one phase shifter is involved, the shaft position on the second is added to that on the first and the mean taken with these two numbers. Experience has shown that the phase can be set accurately to within one shaft turn of the phase shifter, which corresponds to 5.7^0 at 1 GHz. Once the phase is set ($\phi_p=\phi_c$), the probe deflection magnitude $|\Delta z|$ is then measured for various control switch settings. Thus, the probe parameter A is varied over its full range form 0 to V_{max}.

For a circuit signal amplitude V_c=0.272V, Fig. 5.14 shows the measured probe deflection magnitude |Δz| as a function of probe parameter A. Here the data taken with different control switch settings has been mapped to the corresponding A values of the probe parameter using the look–up table described in the previous section. Unlike the square–wave modulation results in chapter 4, the plot has two null points. This is because of the specific square–wave modulation arrangement used in our measurement system. From (5.6), the deflection is nulled not only when $A=V_c$ with $\phi_p=\phi_c$, but also when K=0. When $A=V_{max}$ (i.e. when there is no square–wave modulation), K=0 and so the deflection is also nulled at that point. The other point corresponds to the case where $A=V_c$. This situation is not encountered in normal square wave modulation as only A is varied and K is held constant. In the system used here, both A and K change simultaneously.

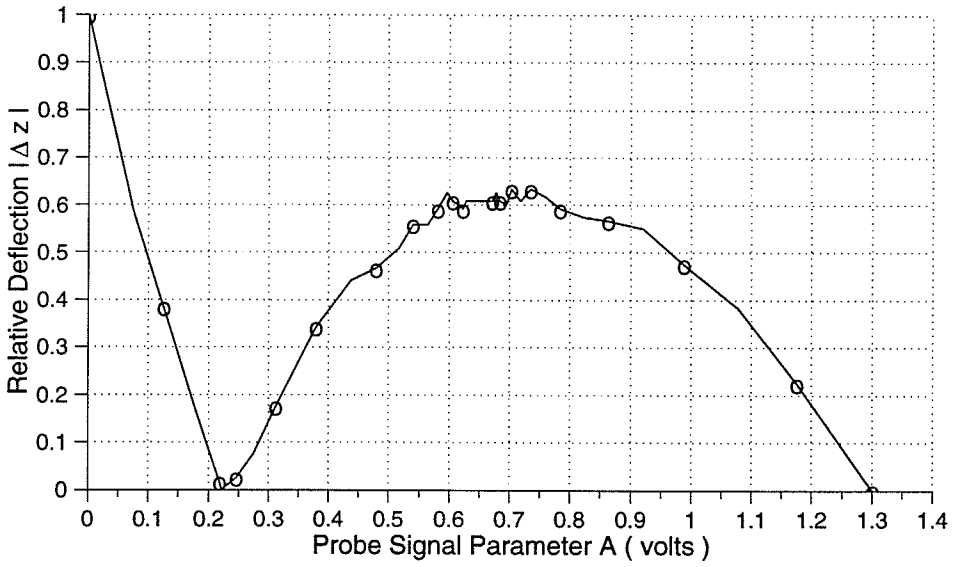

Fig. 5.14 Relative deflection signal as a function of the probe signal parameter A for test circuit amplitude V_c=0.272 V.

Fig. 5.15 (a,b,c) show similar plots for V_c=0.388, V_c=0.529 and V_c=0.765 volts, respectively. Since the range to which A can be varied is limited by the output of the amplifier, the curve progressively starts becoming flat near the null point as the circuit signal amplitude V_c is increased and approaches V_{max}.

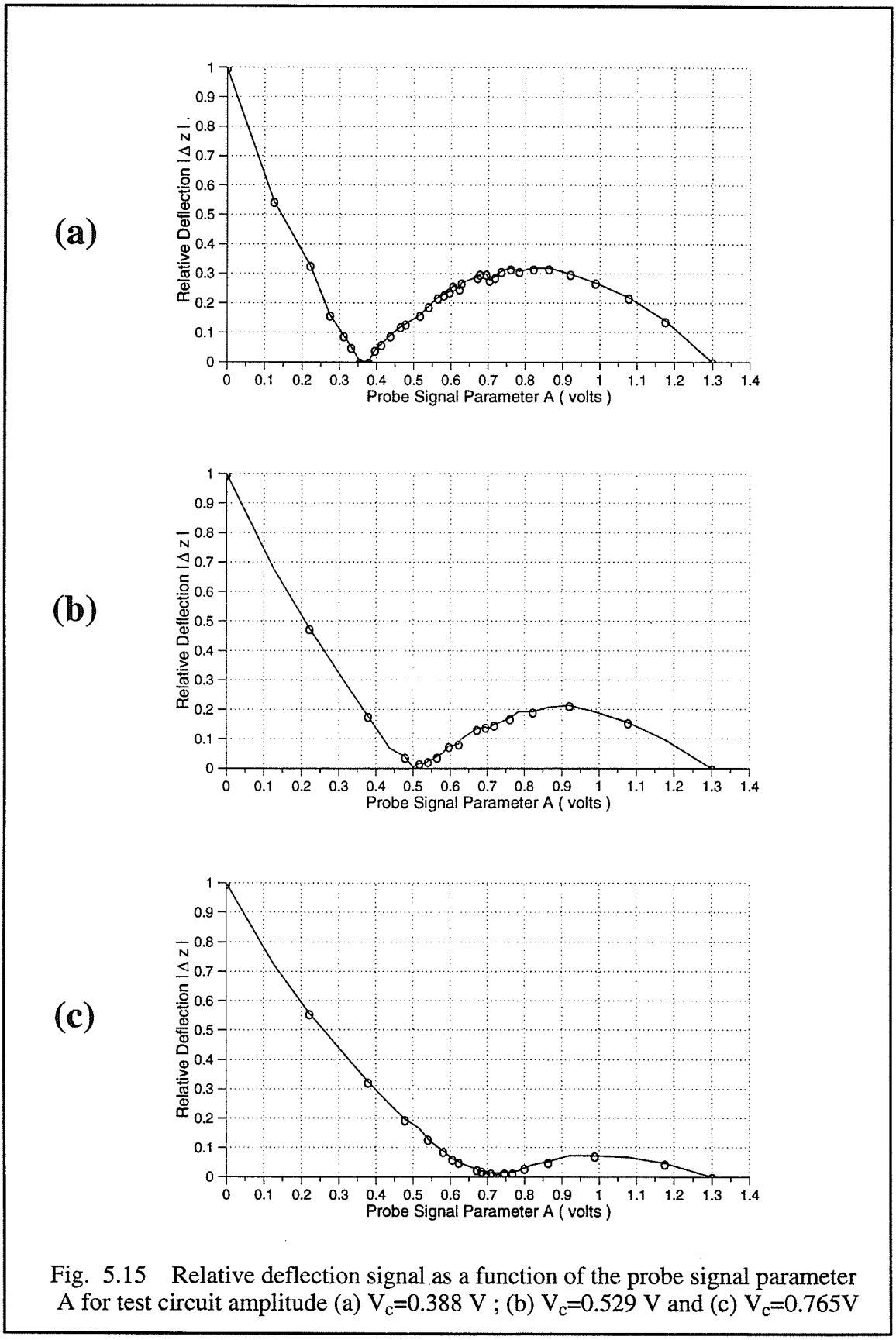

Fig. 5.15 Relative deflection signal as a function of the probe signal parameter A for test circuit amplitude (a) V_c=0.388 V ; (b) V_c=0.529 V and (c) V_c=0.765V

Fig. 5.14 and 5.15 indicate that $A \neq V_c$ at the null points. This is because of the standing wave on the open–circuit line feeding the signal to the probe. Thus, a calibration factor is required to calculate the circuit voltage signal from the probe parameter A. To establish this scaling factor, the probe parameter A which nulls the deflection is plotted against the circuit signal amplitude V_c as shown Fig. 5.16. A near linear variation of the probe parameter as a function of the circuit signal amplitude indicates that a constant scaling factor is involved. From this plot, the scaling factor can be established. This scaling factor is valid for the specific frequency at which the measurements have been performed, which in our case is 1 GHz.

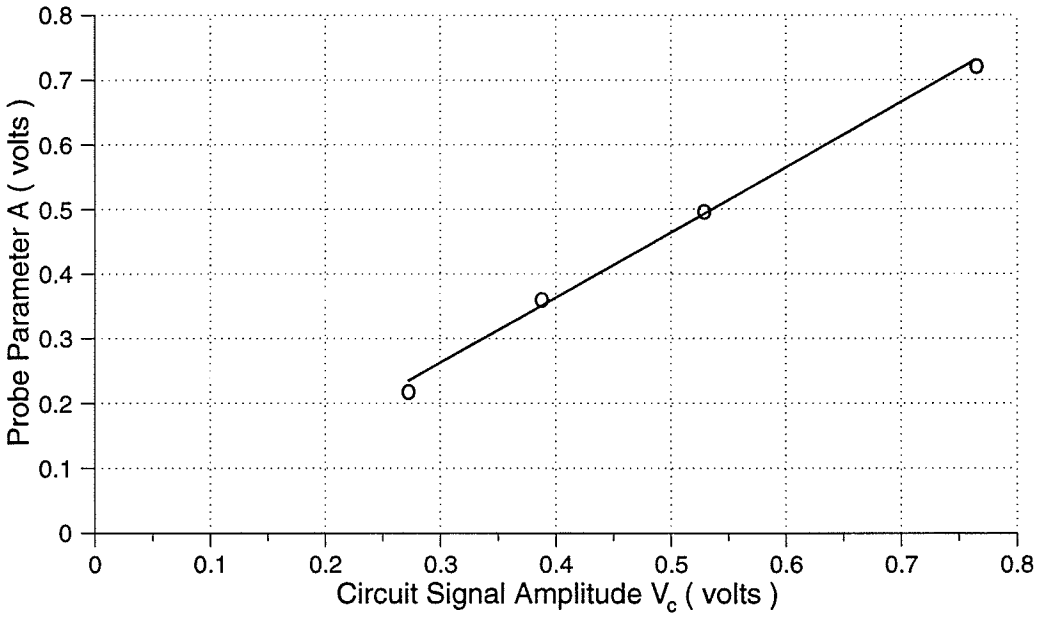

Fig. 5.16 Parameter A as a function of circuit signal amplitude V_c when Δz is nulled. $\phi_p = \phi_c$ and $f_0 = 1$ GHz.

While the measurements of the circuit signal amplitude on a microstrip thru–line are otherwise trivial in the sense that these can be much more easily performed by other means, the results here establish the capability of the instrument to perform sinusoidal measurements at RF frequencies. Also, the signal electronics for generating the square–wave modulated signal is validated.

5.5 Measurements on a Commercial MMIC Amplifier

After measuring the signals on the thru–line, similar measurements at 1 GHz were performed on a commercial MMIC low noise amplifier (LNA).

The LNA (TI–TGA 8061) is a GaAs monolithic low–noise amplifier employing three FET stages [68] with resistive feedback. A photograph of the packaged amplifier is shown in Fig. 5.17. The amplifier has an 18 dB nominal gain over a 0.1–3.5 GHz bandwidth and operates from a single +12 volts supply. The amplifier was packaged at Communications Research Centre, Ottawa [69].

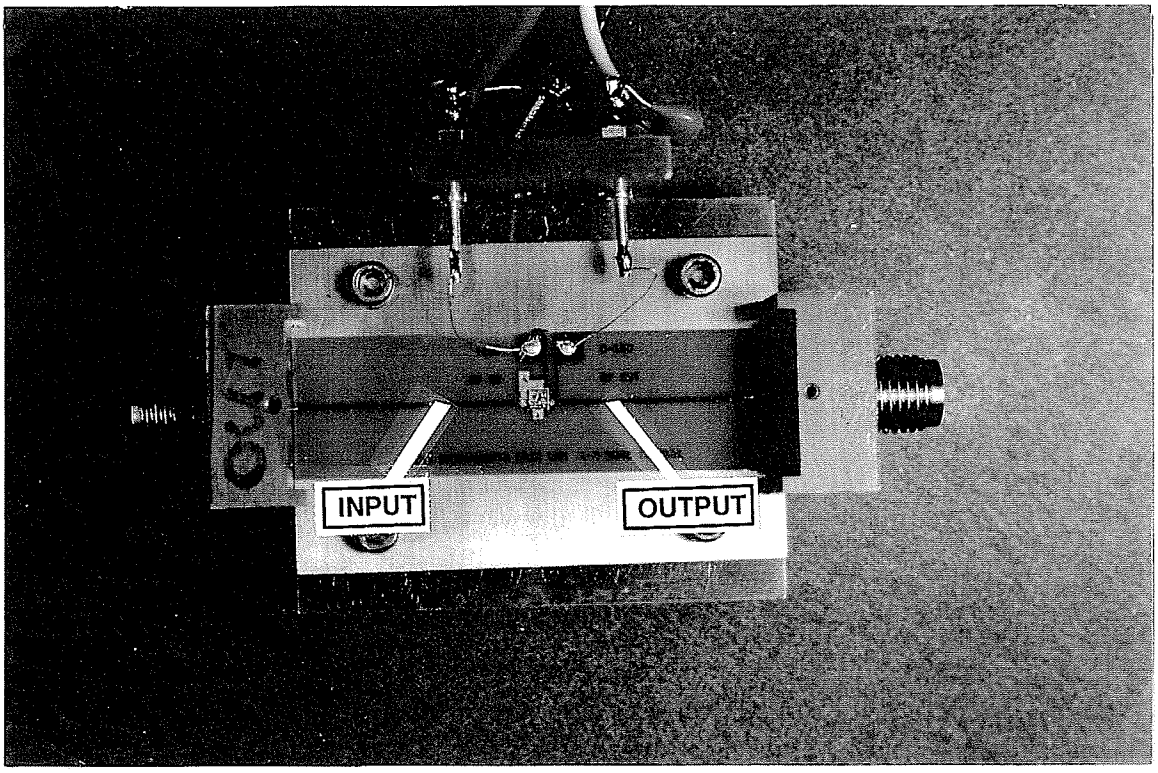

Fig. 5.17 Photograph of the TI Low Noise Amplifier

Fig. 5.18 is a photograph of the device layout on the amplifier. Bond pad and backside metalization is gold plated. The circuit topology of the amplifier is shown in Fig. 5.19.

The measurements were performed on input, output and two internal nodes of the LNA. The internal nodes at which measurements were performed are the output of the first FET and the input to the 3rd FET, respectively. These are identified in

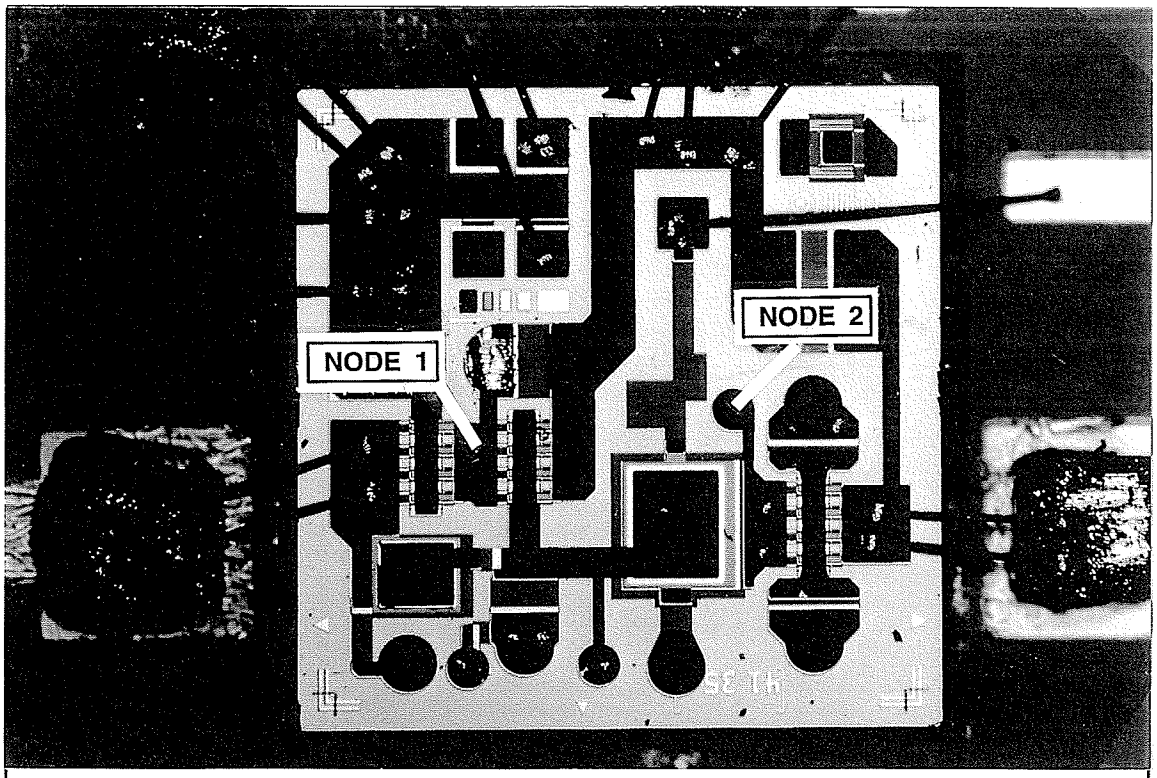

100 µm

Fig. 5.18 Photograph of the Layout on the TI LNA

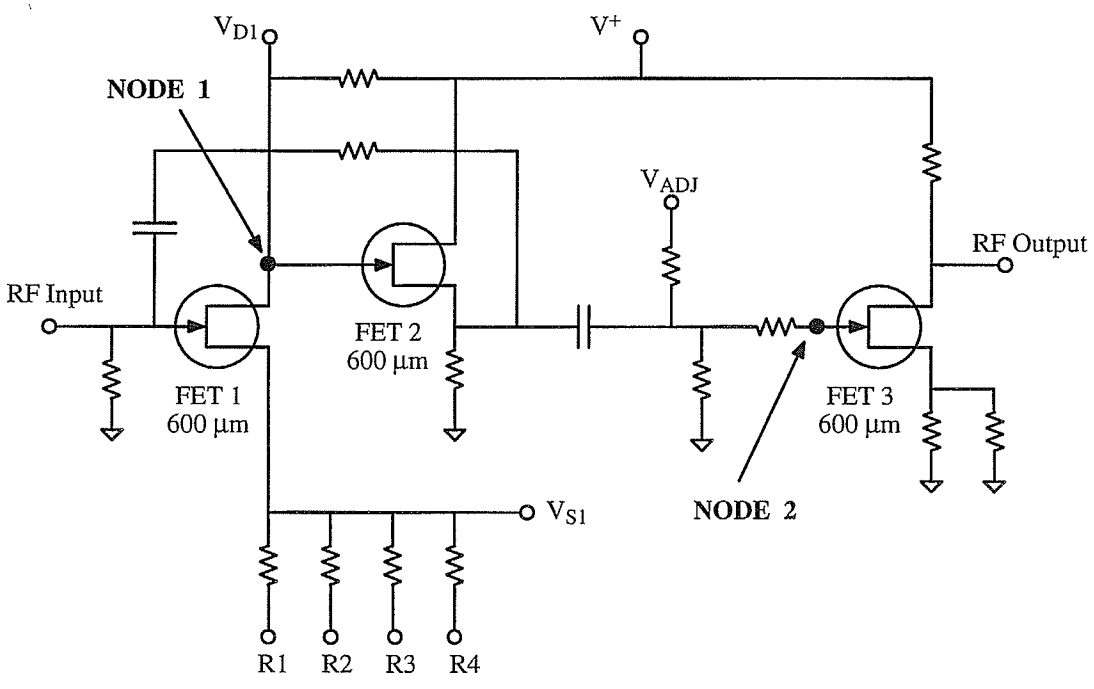

Fig. 5.19 Circuit Diagram of the LNA

the device layout (Fig. 5.18) and the circuit topology (Fig. 5.19). The input and output pads on the circuit had bond wires attached to them. Therefore, those measurements were performed on the 50Ω transmission line leading to the connectors on the amplifier housing as shown in Fig. 5.17. Since the substrate is alumina ($\varepsilon_r \approx 9.6$), the width of the line is fairly small (~1 mm). The chip dimensions are approximately 1.5mm×1.5mm.

Before performing measurements on the LNA, the forward transmission and reflection s–parameters were measured on the network analyzer. The measured s21 is shown in Fig. 5.20 and is in good agreement with the measurement data provided by the supplier. The gain at 1 GHz is ~17.8 dB.

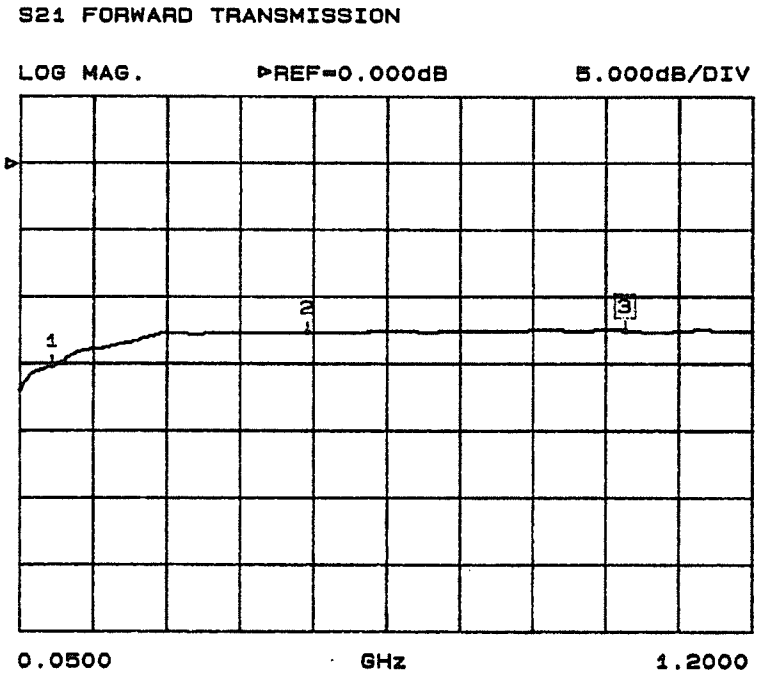

Fig. 5.20 s_{21} of the TI LNA measured on the network analyzer

Fig. 5.21 shows the measured forward reflection s–parameter s11. With better than 20 dB return loss (s11 < –20 dB), the LNA shows a good input match.

First, the measurements were performed on the input line. The circuit signal amplitude was measured on the TDR/Sampler to be 79.5 mV. As in the case of measurements on the thru–line, the probe phase was first adjusted to be equal to the circuit phase. Since V_c is very small in this case, the phase was set with A=0. Fig. 5.22 is a plot of the relative deflection $|\Delta z|$ as a function of probe parameter A. The deflection is

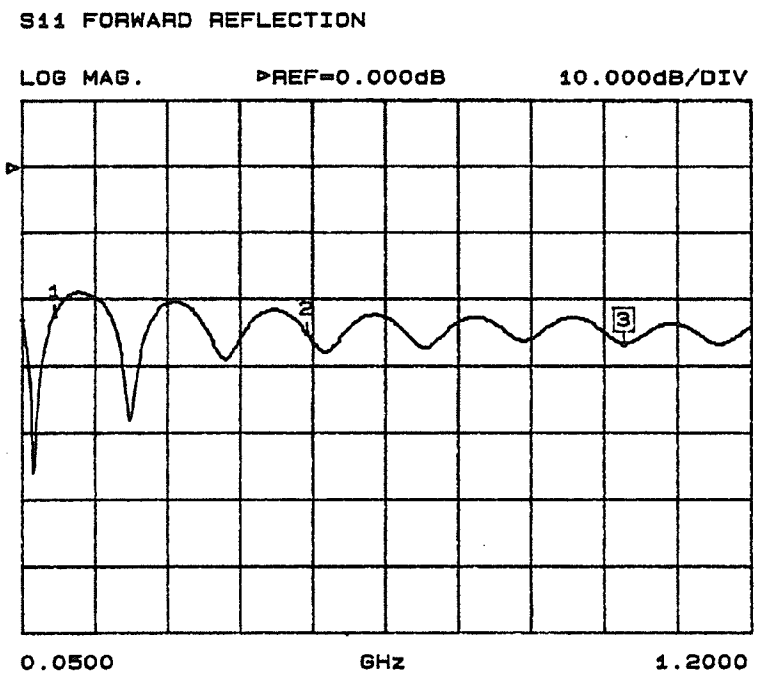

Fig. 5.21 s_{11} of the TI LNA measured on the network analyzer

nulled for A=73.5 mV. Note that the smallest attenuation step was ±0.5 dB, which corresponds to 36 mV and since the signal level is extremely small, the measurement accuracy is limited.

Next, the measurements were performed on the output line of the amplifier. The output signal was measured on the TDR/sampler and was determined to be 0.57 volts. The phase was set at $+73^0$ with respect to the input. Fig. 5.23 shows a plot of the relative deflection as a function of A. Here the deflection is nulled for A=0.625 volts. While measuring the signal on the output line, the output of the amplifier was connected to the TDR/Sampler. Thus the voltage waveform could be observed while performing the measurements. As the probe approached the circuit and was within 1 μm of the test point on the output line, no change was observed in the amplitude and/or shape of the waveform on the sampler. This observation clearly demonstrates the non–invasive nature of the measurement technique.

In all the previous measurement cases including the ones on the thru–line, the circuit signal to be measured could be measured externally using the TDR/sampler as well. However, the signals on the two internal nodes cannot be measured by any straightforward technique. Therefore, the circuit signal amplitudes are not known apriori

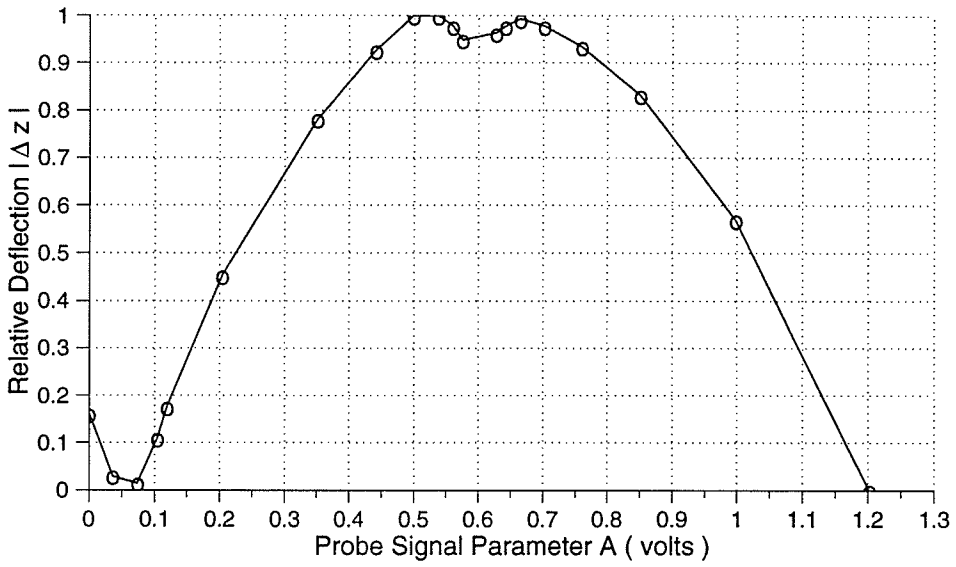

Fig. 5.22 Relative deflection signal as a function of the probe signal parameter A on the LNA Input line : V_c=79.5 mV.

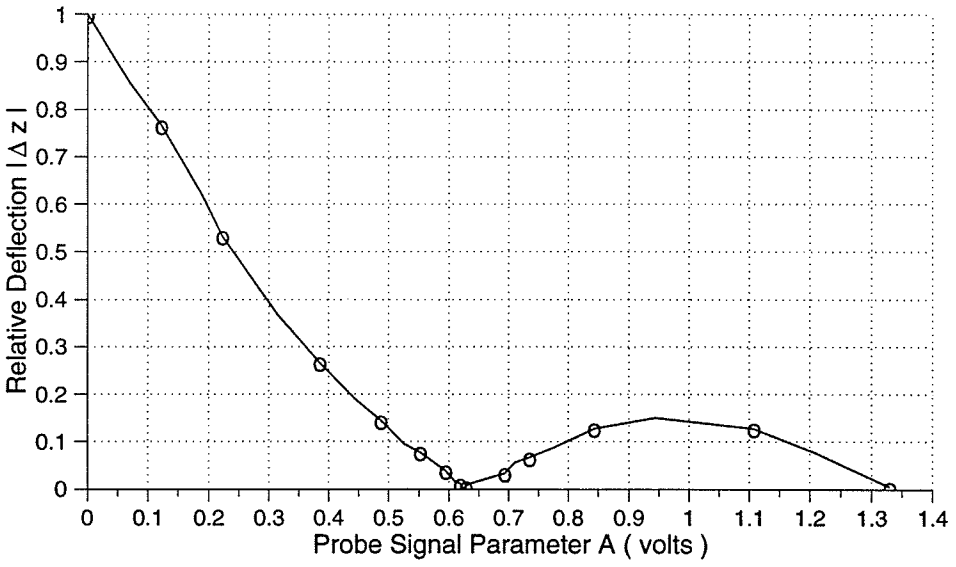

Fig. 5.23 Relative deflection signal as a function of the probe signal parameter A on the LNA Output line : V_c=0.57 V.

in these cases. The measurements on the internal nodes specified earlier were performed next.

Node 1 is the output of the first FET. The probe was positioned on the area indicated in Fig. 5.18 and lowered to within 1 μm of the circuit surface. Measurements were performed as before, setting the probe phase first and then taking the deflection measurements for different control switch settings. Fig. 5.24 is the plot of relative deflection vs. A for this node. From the plot, it is determined that the deflection is nulled for A=0.585 volts. The phase setting relative to the input node was -149^0.

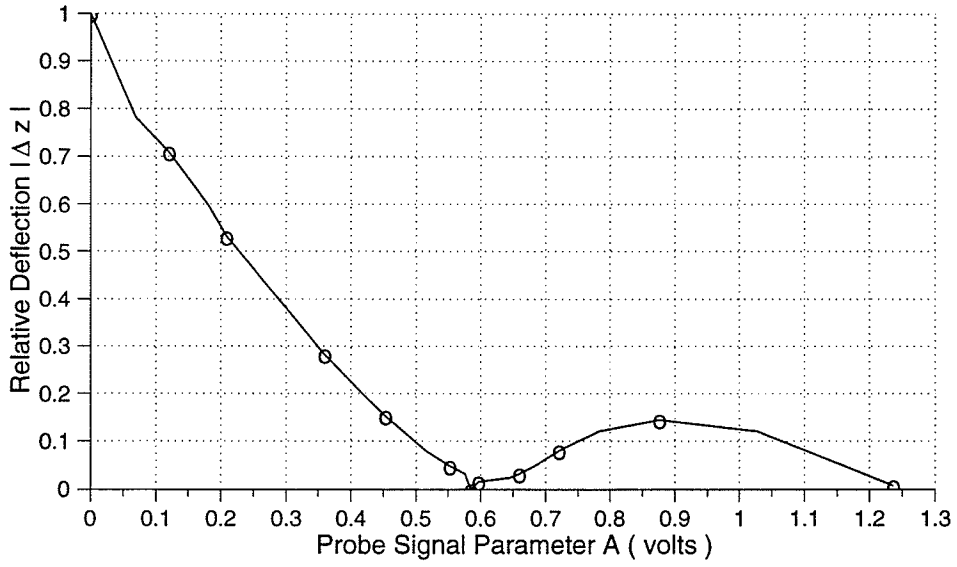

Fig. 5.24 Relative deflection signal as a function of the probe signal parameter A on the LNA Node 1 : V_c not known

Node 2 is the input to the 3rd FET stage as indicated in the circuit diagram of Fig. 5.19. The area where the probe was positioned is indicated on the device layout of Fig. 5.18. Fig. 5.25 is the corresponding plot of relative deflection vs. probe parameter A for this node. The deflection was nulled for A=0.50 volts with phase set at -142^0 relative to the input.

The measurement results on the input, output and the two internal nodes of the LNA are summarized in Table 5.2. The phase has been calculated by noting the shaft position that was set for each of the measurements and by using the nominal phase

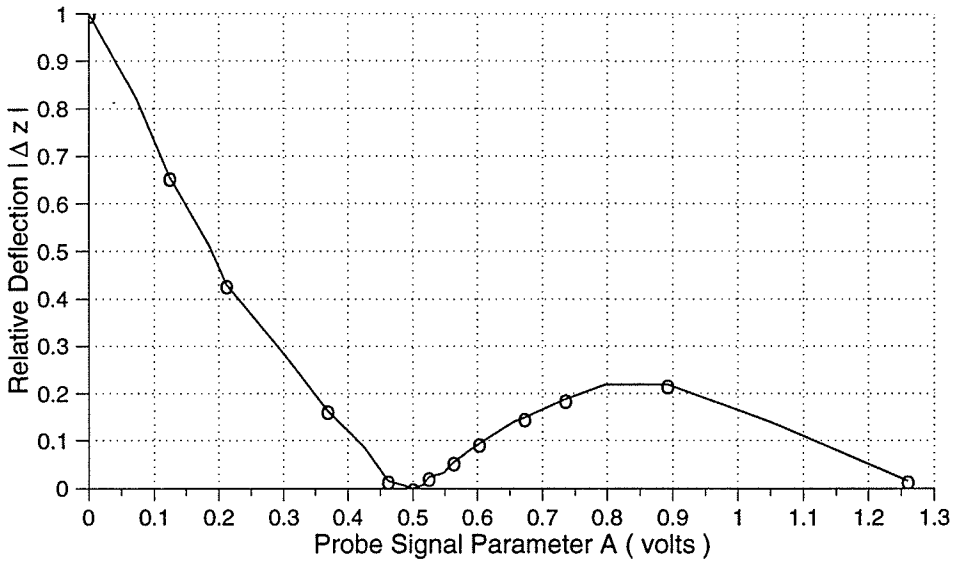

Fig. 5.25 Relative deflection signal as a function of the probe signal parameter A on the LNA Node 2 : V_c not known

shift/shaft turn of 5.7^0 at 1 GHz. The phase shifts are indicated relative to the phase on the point probed on the input line. The gains are calculated using the measured parameter A for which the deflection was nulled. Since only ratios are involved, any scaling factor involved is cancelled out. The overall gain of the amplifier is calculated using the measured values at the input and output as +18.6 dB. The respective gains of the individual FET stages have been calculated using the measurements made at the two internal nodes and are listed in the table.

Measurements at internal nodes of the MMIC is a significant result since these measurements could not be possibly performed with any other means. This demonstrates the usefulness of the instrument. Since the component values and FET models were not available, it was not possible to perform any simulation on the circuit to predict the voltages at the internal nodes. In such a situation, while it is difficult to comment on the accuracy of measurements at these nodes, circuit topology suggests that the first FET stage is an amplifier stage while the second stage is like a source follower. High gain in the first stage and a small loss in the second stage indicates some correspondence with the actual circuit signal amplitudes expected at these nodes.

Table 5.2 : Summary of Test Results

	Input	Node 1	Node 2	Output
Actual	79.5 mV	Unknown	Unknown	570 mV
Measured	73.5 mV ± 36 mV $\angle 0^0$	585 mV ± 5 mV $\angle -149^0 \pm 5.7^0$	500 mV ± 8 mV $\angle -142^0 \pm 5.7^0$	625 mV ± 5 mV $\angle +73^0 \pm 5.7^0$
Gain		+ 18.02 dB 1st Stage	–1.37 dB 2nd Stage	+ 1.94 dB 3rd Stage
Overall Gain | s21| = + 18.6 dB				

The deflection at resonant frequency in these measurements was monitored on a FFT spectrum analyzer where peak value at the modulating frequency was used in the measurement results. Alternately, a lock–in amplifier can be used. Using a large time–constant, nulling the deflection with the lock–in amplifier is capable of providing much more accurate results.

CHAPTER 6

Extensions and Conclusions

Before making the concluding remarks, some extensions of the heterodyne technique are briefly described. This includes the spectral analysis of waveforms and the measurement of arbitrary repetitive waveforms by pulsed sampling.

6.1 Spectral Analysis of Waveform

In chapter 3, an AC measurement scheme was described which can be used to extract the circuit amplitude and phase of a high frequency signal. The circuit signal was assumed to be of the form

$$v_c(x, y, t) = V_c \sin(\omega_0 t + \phi_c) \tag{6.1}$$

This is the case in linear circuit applications where the circuit is excited with a signal at reference frequency ω_0 and this remains unchanged at all points on the circuit. The magnitude and phase which would vary at different points on the circuit can be extracted using the technique described earlier.

In general, however, the circuit signal $v_c(x,y,t)$ may contain the fundamental frequency ω_0 as well as its harmonics. The circuit test point voltage will then be a periodic waveform with period $T=2\pi/\omega_0$ as shown in Fig. 6.1(a). To implement the heterodyne

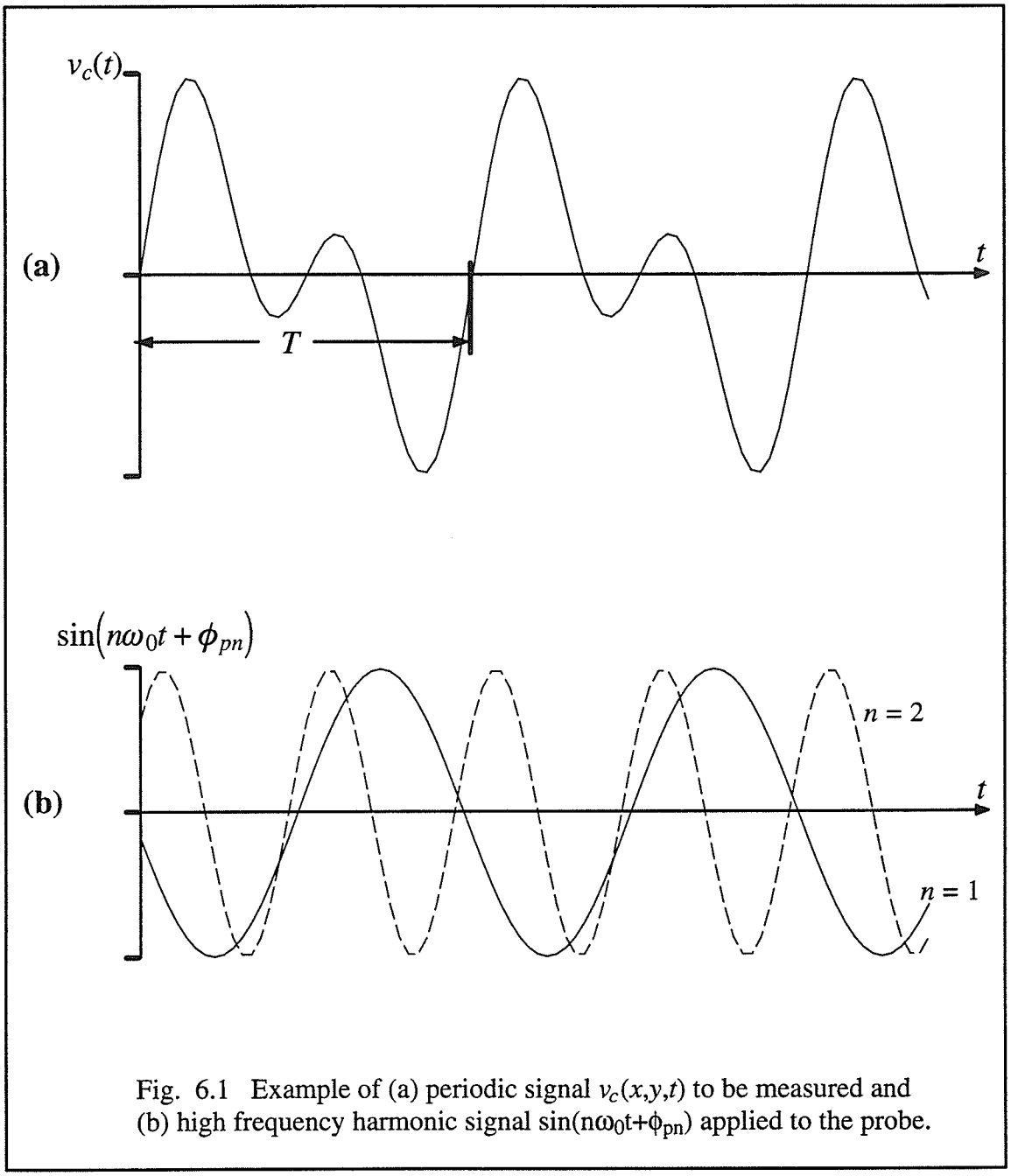

Fig. 6.1 Example of (a) periodic signal $v_c(x,y,t)$ to be measured and (b) high frequency harmonic signal $\sin(n\omega_0 t+\phi_{pn})$ applied to the probe.

technique, a signal at a specified harmonic of the fundamental frequency $\sin(n\omega_0 t+\phi_{pn})$, n=1,2,... is modulated and applied to the probe as [61]

$$v_p(t) = \left[A + K\cos(\omega_r t)\right]\sin(n\omega_0 t + \phi_{pn}) \tag{6.2}$$

The harmonic signal here is synthesized externally with n, A, K and ϕ_{pn} being controllable parameters in the instrument. The modulating signal contains a frequency component at the probe resonance ω_r and a DC bias component A. Using (3.1) and the specified potentials, the force on the probe will be

$$F_z = \frac{1}{2}\frac{\partial C}{\partial z}\left[\left(A + K\cos(\omega_r t)\right)\sin(n\omega_0 t + \phi_{pn}) - v_c(x,y,t)\right]^2 \qquad (6.3)$$

This results in a static force component, several high frequency components ($n\omega_0 \pm \omega_r$), ($n\omega_0 \pm 2\omega_r$), as well as components at frequencies ω_r and $2\omega_r$. The static force component is given by

$$F_z|_{DC} = \frac{1}{2}\frac{\partial C}{\partial z}\left[\frac{A^2}{2} + \frac{K^2}{4} - \frac{2A}{T}\int_0^T \sin(n\omega_0 t + \phi_{pn})v_c(x,y,t,)dt + \frac{1}{T}\int_0^T v_c^2(x,y,t)\ dt\right] \qquad (6.4)$$

which causes a fixed deflection of the probe. The force component at the resonant frequency ω_r is given by

$$F_z|_{\omega=\omega_r} = \frac{\partial C}{\partial z}\left[\frac{AK}{2} - K\frac{1}{T}\int_0^T \sin\left(n\omega_0 t + \phi_{pn}\right)v_c(x,y,t)dt\right]\cos(\omega_r t) \qquad (6.5)$$

The probe will not respond to high frequency components. On examination of (6.5), the integral term represents the magnitude of the Fourier components of the circuit signal $v_c(x,y,t)$. The nulling technique described earlier is then used to determine the value of these Fourier components. A lock–in amplifier is used so that the deflection signal $\Delta z(\omega_r) \sim QF_z(\omega_r)/k$ at the resonant frequency ω_r is detected. The desired harmonic frequency $n\omega_o$ and an arbitrary initial phase ϕ_{pn} are set. The modulating signal bias parameter A is then varied to null the deflection signal $\Delta z(\omega_r)$. When this is accomplished, the parameter A will be equal to the Fourier component for $(n\omega_o, \phi_{pn})$. To obtain both quadrature components at the harmonic $n\omega_0$, the phase ϕ_{pn} is changed by 90^0 and the nulling procedure is repeated. In this manner, the Fourier components of a repetitive sinusoidal waveform can be extracted.

6.2 Sampled Waveform Measurements

The techniques discussed so far could measure amplitude and phase of sinusoidal signals. To measure arbitrary repetitive signals, a different approach is required. Here, instead of using sinusoidal probe excitation, a pulsed excitation is used to make sampled waveform measurements. A block diagram of the sampled waveform measurement is shown in Fig. 6.2 [70].

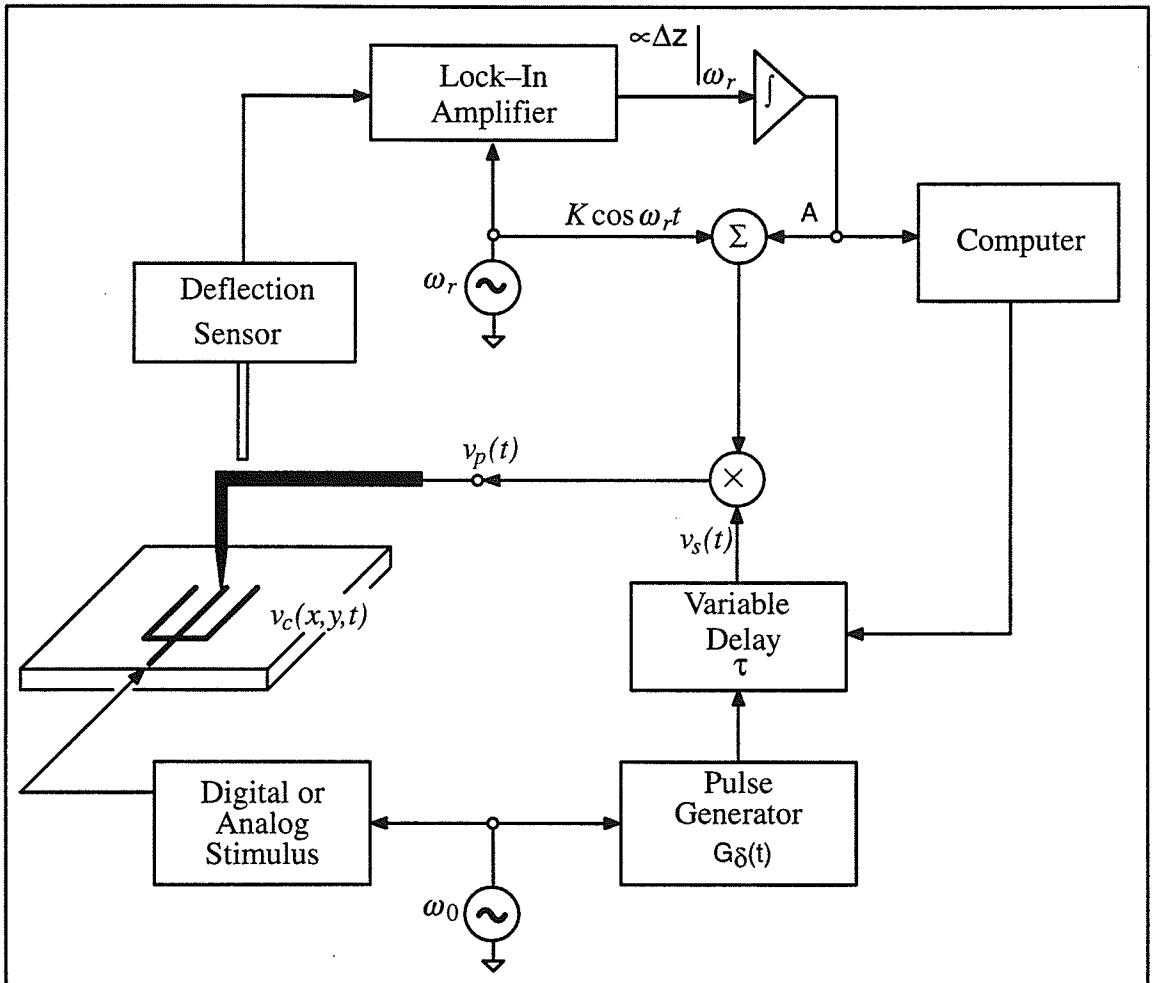

Fig. 6.2 Block Diagram of the Heterodyne technique for high frequency sampled waveform measurement

In this arrangement, the test circuit is triggered by a reference signal of period $T=2\pi/\omega_0$, with $\omega_0 >> \omega_r$. The reference signal is also used to generate a periodic high frequency sampling signal $v_s(t)$, as shown in Fig. 6.3(b).

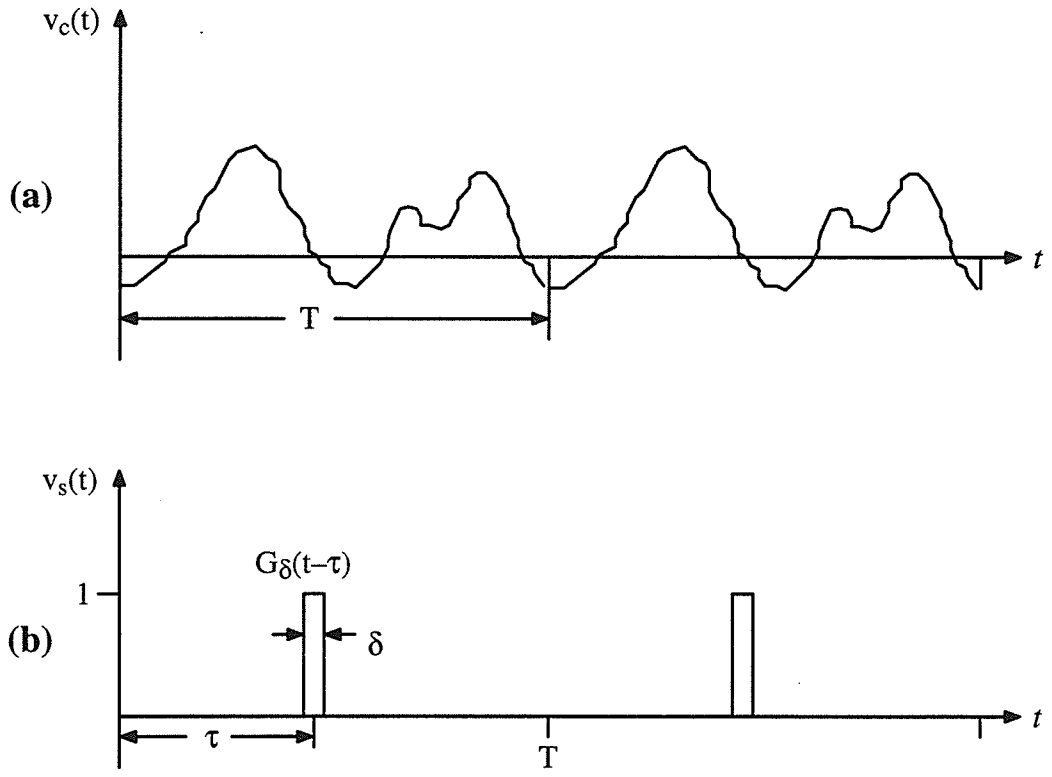

Fig. 6.3 Example of (a) periodic waveform $v_c(x,y,t)$ to be measured and (b) variable delay sampling pulse $v_s(t)=G_\delta(t-\tau)$ which is modulated and applied to the probe

The sampling signal is a narrow pulse $v_s(t)=G_\delta(t-\tau)$, where τ is the pulse delay and δ is the pulse width. The sampling signal is then modulated and applied to the probe as

$$v_p(t) = \left[A + K\cos(\omega_r t)\right]v_s(t) \tag{6.6}$$

Using this as the probe signal, the force can be calculated as before using (3.1). The force contains several high frequency terms to which probe cannot respond, several DC terms which causes a static deflection and terms at resonant frequency of the probe ω_r. The force term at ω_r is

$$F_z|_{\omega=\omega_r} = \frac{\partial C}{\partial z}\Big[\, A < v_s(t), v_s(t) > - < v_s(t), v_c(x,y,t) > \Big]\, K\cos(\omega_r t)$$

$$< a(t), b(t) > = \frac{1}{T}\int_0^T a(t)b(t)dt \quad , \quad < a(t) > = \frac{1}{T}\int_0^T a(t)dt \tag{6.7}$$

where < , > and < > indicate the inner product and average over the period T respectively. Using (6.7) for the pulse sampling signal G_δ, the probe deflection at ω_r will be

$$\Delta_z|_{\omega_r} = \frac{\partial C}{\partial z}\frac{Q}{K}\left[A\frac{\delta}{T} - < G_\delta(t-\tau), v_c(x,y,t) >\right] K\cos(\omega_r t) \tag{6.8}$$

Ideally, for narrow sampling pulse widths $\delta << T$, the remaining inner product in (6.8) can be approximated by

$$< G_\delta(t-\tau), v_c(x,y,t) > \;\approx\; v_c(x,y,t=\tau)\frac{\delta}{T} \tag{6.9}$$

Thus, by adjusting the probe parameter A so that the force component at ω_r is nulled, the magnitude of the signal $v_c(x,y,t{=}\tau)$ can be determined. To obtain the entire waveform of $v_c(x,y,t)$, the delay τ is scanned over the period $0 < \tau < T$.

6.3 Conclusions

RF electronics for measurements in the GHz frequency range using the electrostatic force microscope has been set up. A square–wave modulation scheme has been implemented using commonly available microwave components. This allows measurements on internal nodes of ICs and MMICs in a non–invasive manner.

Measurements at 1 GHz were performed on simple structures such as a microstrip thru–line as well as on a more complicated MMIC low noise amplifier. The measured gain matches well with the gain measured with the network analyzer. The ability of the instrument to measure voltages at the internal nodes of these circuits and devices equips the designer with a useful diagnostic tool to analyze the performance of individual components on the chip.

In the instrument, the nulling was done manually using the control switches. A lock–in amplifier with a feedback loop to automatically adjust the deflection to zero and extract the circuit signal amplitude is a desirable feature in the instrument. The phase would have to be set accurately too, using the procedure described, to completely automate the measurement procedure. Since the phase shifter used was manual, alternate components and devices which will allow this automatic manipulation need to be explored.

A molybdenum wire probe soldered to the centre conductor of a semi–rigid coaxial cable was used as the probe. Thermal considerations necessitated the location of the termination some distance from the end of the probe. This resulted in a long length of open–circuit line and consequently a narrow band match for the signal being fed to the probe. While this approach was acceptable for sinusoidal measurements, where the bandwidth of the signal is not very high, alternate approaches need to be investigated to match the probe over a wide range of frequencies. Specifically, if pulsed sampling measurements are to be performed in the Mbit or Gbit range, where the bandwidth of the probe signal is very high, the simplistic probe matching approach adopted here will not work. With a wideband match, the system can be used to perform swept frequency measurements, like a network analyzer. One approach could be using an adjustable stub to match the probe at various frequencies, or using an electronic phase shifter to automatically adjust the length of the open–circuit line.

The wire probe at the end of the coaxial cable represents a discontinuity since the wire cannot be considered a transmission line. This not only affects the probe matching, but would also ultimately limit the upper end of the frequency range to which such a probe could be used. Beyond a few GHz, the probe parasitics are considerable and the probe would behave like an antenna. Thus a probe where transmission lines reach the very end of the probe tip is desirable. With proper probe match, the upper limit on frequency is determined by the coupling capacitance. As mentioned earlier, the capacitance between the probe and the circuit, calculated numerically, is on the order of 0.2 fF. This means that the technique can be used up to at least 1 THz.

From the sensitivity point of view as well, alternate probes need to be explored. Micromachined cantilever probes, with a much higher resonant frequency, are expected to provide enhanced sensitivity in measurements. The resolution is also improved since these probes can be positioned closer to the circuit test point.

REFERENCES

[1] K. de Kort, "The Role of Internal waveform Measurements in IC Development", *Microelectronic Engineering*, vol. 24, No. 1–4, pp. 365–376, March 1994.

[2] D. Winkler, R. Schmitt, M. Brunner and B. Lischke, "Flexible Picosecond Probing of Integrated Circuits with Chopped Electron Beams", *IBM Journal of Research and Development*, vol. 34, No. 2/3, pp. 189–203, March/May 1990.

[3] E. Wolfgang, "Electron Beam Testing" in *Handbook of Advanced Semiconductor Technology and Computer Systems*, Ed. G. Rabbat (Van Nostrand Reinhold, New York, 1988) pp. 148–180.

[4] V.R.M. Rao and A. Saini, "Electron Beam Probing for Design Verification at Intel", *Microelectronic Engineering*, vol. 24, No. 1–4, pp. 25–34, March 1994.

[5] R. Clauberg, H. Beha, A. Blacha and H.K. Seitz, "Picosecond Photoemission Probing of Integrated Circuits : Capabilities, Limitations and Applications", *IBM Journal of Research and Development*, vol. 34, No. 2/3, pp. 173–187, March/May 1990.

[6] P.G. May, J.M. Halbout and G.L. Chiu, "Non–Contact High–Speed Waveform Measurements with the Picosecond Photoelectron Scanning Electron Microscope", *IEEE Journal of Quantum Electronics*, vol. 24, No. 2, pp. 234–239, Feb. 1988.

[7] T.T. Lee, T. Smith, H.C. Huang, E. Chauchard and C.H. Lee, "Optical Techniques for On–Wafer Measurements of MMICs", *Microwave Journal,* vol. 33, pp. 91–102, May 1990.

[8] M. Y. Frankel, "500–GHz Characterization of an Optoelectronic S–parameter Test Structure", *IEEE Microwave and Guided Wave Letters*, vol. 4, No.4, pp. 118–120, April 1994.

[9] J. Kim, S. Williamson, J. Nees, S. Wakana and J. Whitaker, "Photoconductive Sampling Probe with 2.3–ps Temporal Resolution and 4–μV Sensitivity", *Applied Physics Letters*, vol. 62 (18), pp. 2268–2270, 3 May 1993.

[10] D.L. Millard, K.R. Umstadter and R. C. Block, "Noncontact Testing of Circuits", IEEE Design and Test of Computers, pp. 55–63, March 1992.

[11] H.K. Heinrich, "Picosecond Noninvasive Optical Detection of Internal Electrical Signals in Flip–chip mounted Silicon Integrated Circuits", IBM Journal of Research and Development, vol. 34, No. 2/3, pp. 162–172, March / May 1990.

[12] J.M. Wiesenfield, "Electro–optic Sampling of High Speed Devices and Integrated Circuits", *IBM Journal of Research and Development,* vol. 34, No. 2/3, pp. 141–161, March/May1990.

[13] J. A. Valdmanis and G. Mourou, "Subpicosecond Electro–Optic Sampling : Principles and Applications", *IEEE Journal of Quantum Electronics*, vol. QE–22, No. 1, pp. 69–78, Jan. 1986.

[14] W. Mertin, C. Bohm, L. J. Balk, E. Kubalek, "Two–Dimensional Field Mapping in MMIC–Substrates by Electro–Optic Sampling Technique", *IEEE MTT–S Digest*, pp. 1443–1446, 1992.

[15] D. Le Quang, D. Erasme and B. Huyart, "Fabry–Perot Enhanced Real–Time Electro–Optic Probing of MMICs", *Electronics Letters*, vol. 29, No. 5, pp. 498–499, 4 March 1993.

[16] M. Y. Frankel, J. F. Whitaker, G. A. Mourou, J. A. Valdmanis, "Experimental Characterization of External Electro–Optic Probes", *IEEE Microwave and Guided Wave Letters*, vol. 1, No.3 , March 1991.

[17] J.S. Dahele and A.L. Cullen, "Electric Pulse Measurements on Microstrip", *IEEE Transactions on Microwave Theory and Techniques*, vol. 28, No. 7, pp. 752–755, July 1980.

[18] G.E. Bridges and D.J. Thomson, "High Frequency Circuit Characterization using the AFM as a reactive near field probe", *Ultramicroscopy*, vol. 42–44, pp. 321–328, 1992.

[19] G.E. Bridges, T.S. Forzley and D.J. Thomson, "Novel Near–field Probe for On–Wafer Integrated Circuit Measurements", *Microelectronics Journal*, vol. 23, No. 5, pp. 363–369, 1992.

[20] S.S. Osofsky and S.E. Schwarz, "Design and Performance of a Non–Contacting Probe for Measurements on High Frequency Planar Circuits", *IEEE Transactions on Microwave Theory and Techniques,* vol. 40, No. 8, pp. 1701–1708, August 1992.

[21] E. W. Strid, "26 GHz Wafer Probing For MMIC Development and Manufacture", *Microwave Journal*, vol. 29, pp. 71–82, August 1986.

[22] K.E. Jones, E. W. Strid and K. R. Gleason, "mm–Wave Wafer Probes Span 0 to 50 GHz", *Microwave Journal*, vol. 30, pp. 177–183, April 1987.

[23] E. W. Strid and T. Burcham, "Wideband Probing Techniques for Planar Devices", *Solid Sate Technology*, pp. 49–50, August 1989.

[24] G. Rabjohn, J. Wolczanski and R. Surridge, "High Frequency Wafer Probing Techniques", *Canadian Journal of Physics*, vol. 65, No. 8, pp. 850–855, Aug. 1987.

[25] V. A. Ranieri, A. Deutsch, G. V. Kopcsay and G. Arjavalingam, "A Novel 24–GHz Bandwidth Coaxial Probe", *IEEE Transactions on Instrumentation and Measurement*, vol. 39, No. 3, pp. 504–507, June 1990.

[26] R. Yu, M. Reddy, J. Pusl, S. Allen, M. Case and M. Rodwell, "Full Two–port On–wafer Vector Network Analysis to 120 GHz Using Active Probes", *IEEE MTT–S Digest*, pp. 1339–1342, 1993.

[27] M.S. Shakouri, A. Black, B.A. Auld and D.M. Bloom, "500 GHz GaAs MMIC Sampling Wafer Probe", *Electronics Letters*, vol. 29, No. 6, pp. 557–558, 18 March 1993.

[28] H.K.Wickramasinghe, "Scanned Probe Microscopes", *Scientific American*, pp. 98–105, Oct. 1989.

[29] H.K.Wickramasinghe, "Scanning Probe Microscopy : Current Status and future trends", *Journal of Vacuum Science and Technology*, A8 (1), pp. 363–368, Jan./ Feb 1990.

[30] S. Watanabe, K. Hane, M. Ito and T. Goto, "Dynamic Mode Force Microscopy for the Detection of Lateral and Vertical Electrostatic Forces", *Applied Physics Letters*, vol. 63 (18), pp. 2573–2575, 1 Nov. 1993.

[31] Y. Martin and H.K. Wickramasinghe, "Magnetic Imaging by Force Microscopy with 1000Å resolution ", *Applied Physics Letters*, vol. 50(20), pp. 1455–1457, 18 May 1987.

[32] H.K.Wickramasinghe, "Extensions of STM", *Methods of Experimental Physics*, vol. 27, pp. 77–94.

[33] P. Muralt and D.W. Pohl, "Scanning Tunneling Potentiometry", *Applied Physics Letters*, vol. 48 (8), pp. 514–516, 24 Feb. 1986.

[34] P. Muralt, H. Meier, D.W. Pohl and H.W.M. Salemink, "Scanning Tunneling Microscopy and Potentiometry on a Semiconductor Heterojunction", *Applied Physics Letters*, vol. 50 (19), pp. 1352–1354, 11 May 1987.

[35] J.E. Stern, B.D. Terris, H.J. Mamin and D. Rugar, "Deposition and Imaging of Localized Charge on Insulator Surfaces using Force Microscope", *Applied Physics Letters*, vol. 53 (26), pp. 2717–2719, 26 Dec. 1988.

[36] B.D. Terris, J.E. Stern, D. Rugar and H.J. Mamin, "Localized Charge Force Microscopy", *Journal of Vacuum Science and Technology*, A8 (1), pp. 374–377, Jan./ Feb 1990.

[37] B.D. Terris, J.E. Stern, D. Rugar and H.J. Mamin, "Contact Electrification using Force Microscopy", *Physics Review Letters*, vol. 63, No. 24, pp. 2669–2672, 11 Dec. 1989.

[38] F. Saurenbach and B.D. Terris, "Imaging of Ferroelectric Domain Walls by Force Microscopy ", *Applied Physics Letters*, vol. 56 (17), pp. 1703–1705, 23 April 1990.

[39] K. Domansky, Y. Leng, C.C. Williams, J. Janata and D. Petelenz , "Mapping of Mobile Charges on Insulator Surfaces with the Electrostatic Force Microscope", *Applied Physics Letters*, vol. 63 (11), pp. 1513–1515, 13 Sept. 1993.

[40] Y.J. Huang, J. Slinkman and C.C. Williams, "Modelling of Impurity Dopant Density Measurement in Semiconductors by Scanning Force Microscopy", *Ultramicroscopy*, vol. 42–44, pp. 298–303, 1992.

[41] W.A. Zisman, "A New Method of Measuring Contact Potential Differences in Metals", *Review of Scientific Instruments*, vol. 3, No. 7, pp. 367–370, July 1932.

[42] F. Rossi, "Contact Potential Measurement: Spacing–Dependence Errors", *Review of Scientific Instruments*, vol. 63, No. 9, pp. 4174–4181, Sept. 1992.

[43] M. Nonnenmacher, M.P. O'Boyle and H.K. Wickramasinghe, "Kelvin Probe Force Microscopy", *Applied Physics Letters*, vol. 58 (25), pp. 2921–2923, 24 June 1991.

[44] M. Nonnenmacher, M. O'Boyle and H.K.Wickramasinghe, "Surface Investigations with a Kelvin Probe Force Microscope", *Ultramicroscopy*, vol. 42–44, pp. 268–273, 1992.

[45] D. Sarid, "Scanning Force Microscopy with Applications to Electric, Magnetic and Atomic Forces", Oxford University Press, Inc., 200 Madison Avenue, New York, New York 10016, 1991.

[46] C.A.J. Putman, Bart G. De Grooth, N.F. Van Hulst and J. Greve, "A Detailed Analysis of the Optical Beam Deflection Technique for Use in Atomic Force Microscopy", *Journal of Applied Physics*, vol. 72 (1), pp. 6–12, 1 July 1992.

[47] P.J. Mulhern, T. Hubbard, C.S. Arnold, B.L. Blackford and M.H. Jericho, "A Scanning Force Microscope with a Fiber–Optic Interferometer Displacement Sensor", *Review of Scientific Instruments*, vol. 62, No. 5, pp. 1280–1284, May 1991.

[48] M. Nonnenmacher, M. Vaez–Iravani and H.K. Wickramasinghe, "Attractive Mode Force Microscopy using a Feedback Controlled Fiber Interferometer", *Review of Scientific Instruments*, vol. 63, No. 11, pp. 5373–5376, Nov. 1992.

[49] D. Rugar, H.J. Mamin and P. Guethner, "Improved Fiber–Optic Interferometer for Atomic Force Microscopy", *Applied Physics Letters*, vol. 55 (25), pp. 2588–2590, 18 Dec. 1989.

[50] J. Song, D.J. Thomson and G.E. Bridges, "Super Luminescent Diode Based Optical Fiber Interferometer for Force Microscopy", *Technical Report UMECE TR–94–102*, Department of Electrical and Computer Engineering, University of Manitoba, Winnipeg, Manitoba, Canada, 1994.

[51] U. Mueller, C. Bohm, J. Sprengepiel, C. Roths, E. Kubalek and A. Beyer, "Geometrical and Voltage Resolution of Electrical Sampling Scanning Force Microscopy", *IEEE MTT–S Digest*, pp. 1005–1008, 1994.

[52] R.A. Said, "Scanning Force Potentiometry for Semiconductor Circuit Characterization", *Ph.D. Candidacy Report*, Department of Electrical and Computer Engineering, University of Manitoba, Winnipeg, Manitoba, Canada, 1994.

[53] S. Watanabe, K. Hane, T. Ohye, M. Ito and T. Goto, "Electrostatic Force Microscope Imaging Analyzed by the Surface Charge Method", Journal of Vacuum Science and Technology B 11 (5), pp. 1774–1781, Sept./ Oct. 1993.

[54] Y. Martin, C.C. Williams and H.K. Wickramasinghe, "Atomic Force Microscope – Force Mapping and Profiling on a sub 100–Å scale", *Journal of Applied Physics*, vol. 61 (10), pp. 4723–4729, 15 May 1987.

[55] Y. Martin, D.W. Abraham and H.K. Wickramasinghe, "High Resolution Capacitance Measurement and Potentiometry by Force Microscopy", *Applied Physics Letters*, vol. 52(13), pp. 1103–1105, 28 March 1988.

[56] J.M.R. Weaver and D.W. Abraham, "High Resolution Atomic Force Microscopy Potentiometry", *Journal of Vacuum Science and Technology* B, vol. 9, No. 3, pp. 1559–1561, May/ June 1991.

[57] R.A. Said, G.E. Bridges and D.J. Thomson, "Noninvasive Scanned Probe Potentiometry for Integrated Circuit Diagnostics", *IEEE Transactions on Instrumentation and Measurement*, vol. 43, No. 3, pp. 469–474, June 1994.

[58] A.S. Hou, F. Ho and D.M. Bloom, "Picosecond Electrical Sampling using a Scanning Force Microscope" *Electronics Letters*, vol. 28, No. 25, pp. 2302–2303, 3 Dec. 1992.

[59] G.E. Bridges, R. A. Said and D.J. Thomson, "Heterodyne Electrostatic Force Microscopy for Non–Contact High Frequency Integrated Circuit Measurement", *Electronics Letters*, vol. 29, No. 16, pp. 1448–1449, 5 Aug. 1993.

[60] R. A. Said, G.E. Bridges and D.J. Thomson, "Scanned Electrostatic Force Microscope for Noninvasive High Frequency Potential Measurement", *Applied Physics Letters*, vol. 64 (11), pp. 1442–1444, 14 March 1994.

[61] R.A. Said, M. Mittal, G.E. Bridges and D.J. Thomson, "High Frequency Potential Probe Using Electrostatic Force Microscopy", *Journal of Vacuum Science and Technology* A 12 (4), pp. 2591–2594, July/ Aug. 1994.

[62] M. Mittal, R.A. Said and G.E. Bridges, "Noncontact Voltage Measurements in Microwave Integrated Circuits", *Proceedings of the 1994 ANTEM Conference*, pp. 387–390, Ottawa, Canada, August 1994.

[63] A.J. Melmed, "The Art and Science and other aspects of making sharp tips", Journal of Vacuum Science and Technology B 9(5), pp. 601–608, March/ April 1991.

[64] D.M. Pozar, "Microwave Engineering", Addison–Wesley Publisihing Copmany, Inc.

[65] R. Compton and D. Rutledge, "PUFF Manual".

[66] Mini–Circuits Components Catalog.

[67] I.J. Bahl and P. Bhartia, "Microstrip Antennas", Artech House, Inc., 610 Washington Street, Dedham, Massachussets, 02026, 1980.

[68] TGA 8061 Application Notes, Texas Instruments.

[69] D. Roscoe, Communications Research Centre, Ottawa, private communication.

[70] G.E. Bridges, R. A. Said, M. Mittal and D.J. Thomson, "Sampled Waveform Measurement in Integrated Circuits Using Heterodyne Electrostatic Force Microscopy", to appear in *Review of Scientific Instruments*, vol. 65, No. 11, November 1994.